TECHNISCHE UNIVERSITÄT WIEN
Vienna | Austria

DISSERTATION

Thermo-mechanically induced fatigue damage in thin metal films: simulation, comparison to experiments, and fatigue damage parameter calibration

carried out for the purpose of obtaining the degree of Doctor technicae (Dr. techn.),

submitted at TU Wien, Faculty of Mechanical and Industrial Engineering, by

Dipl.–Ing. Paul Hoffmann

[redacted]

under the supervision of

Assoc. Prof. Dipl.–Ing. Dr. techn. Melanie Todt

Institute of Lightweight Design and Structural Biomechanics, E317

reviewed by

Priv. Doz. Dr. Megan J. Cordill
Erich Schmid Institute of Materials Science,
Austrian Academy of Sciences, Austria

Univ.Prof. Dipl.-Ing. Dr.techn. Ernst Kozeschnik
Institute of Materials Science and Technology,
TU Wien, Austria

This work was supported by Austrian Research Promotion Agency (FGG) within the framework of the project No. 874907.

I confirm, that going to press of this thesis needs the confirmation of the examination committee.

Affidavit

I declare in lieu of oath, that I wrote this thesis and performed the associated research myself, using only literature cited in this volume. If text passages from sources are used literally, they are marked as such. I confirm that this work is original and has not been submitted elsewhere for any examination, nor is it currently under consideration for a thesis elsewhere. I acknowledge that the submitted work will be checked electronically-technically using suitable and state-of-the-art means (plagiarism detection software). On the one hand, this ensures that the submitted work was prepared according to the high-quality standards within the applicable rules to ensure good scientific practice "Code of Conduct" at the TU Wien. On the other hand, a comparison with other student theses avoids violations of my personal copyright.

Vienna, December 2017

Paul Hoffmann

Acknowledgment

First of all, I would like to express my sincere gratitude to Assoc. Prof. Dr. Melanie Todt for her excellent supervision and support during my doctoral studies. Without her invaluable time and effort in guiding me through complex problems and providing constructive feedback, this dissertation would not have been possible. I would also like to thank Assoc. Prof. Dr. Heinz Pettermann for his role as a secondary supervisor, supporting me with his experience and input during difficult times.

Furthermore, I would like to express my gratitude to all the members of the ILSB for creating a supportive environment that made my time here an enjoyable experience. I am particularly grateful to my roommates, Marius Schasching and Fabian Key, for the many inspiring discussions we had during coffee breaks.

I would also like to thank the team of the Kompetenzzentrum Automobil- und Industrieelektronik GmbH, Villach (KAI) for their help and support during my thesis. Here I would like to mention, amongst many others, Dr. Balamurugan Karunamurthy, Dr. Michael Nelhiebel, Dr. Manuel Petersmann, and the head of KAI, DI Josef Fugger.

Last but not least, I would like to thank my family, friends, and my partner Eva for their support and sometimes needed motivation.

Contents

Abstract

Power semiconductors are integral components in a wide range of applications. As reliability requirements increase due to size reduction and new application fields e.g., in renewable power generation, new methods for predicting fatigue damage in such devices become increasingly important. Among the numerous failure modes that may occur in power semiconductors, this thesis addresses the issues of thermo-mechanical induced degradation of the copper power metallization and through-film crack formation due to cyclic overload pulses. To address this issue, an existing continuum damage mechanics based physical lifetime modeling framework is applied, further enhanced and calibrated.

In the existing framework, the local fatigue life is split into two stages, namely damage onset and damage evolution, which are described by their respective fatigue laws and parameters. In order to calibrate these parameters, a meaningful comparison between experimental and simulated results must be established. For this purpose, in addition to an adequate representation of the experimental loading conditions, methodologies must be developed to quantify and compare the fatigue damage observed in experiments with those predicted in simulations.

In a first approach binarized images of fatigue cracks visible on the surface of thermo-mechanically loaded test devices are used to define a fatigue crack density. This fatigue crack density is used in conjunction with corresponding simulations to calibrate the parameters related to damage onset. The influence of locally different maximum temperatures and mechanical stress concentrators is studied. Furthermore, the experimental results reveal

that distinct fatigue cracks also form away from stress concentrators, which is not yet well represented by the original simulation framework.

To address this finding, a concept is presented that introduces information about the microstructure into the original framework while keeping the effort for modeling and meshing within reasonable bounds. To better represent experimental results, information about the microstructure in the form of the misorientation angles at triple junctions is introduced as a parameter describing the local susceptibility to void nucleation. The influence of this parameter on the development of fatigue cracks is studied and discussed. In order to calibrate the enhanced fatigue modeling framework, a second comparison method is presented that matches the density of distinct fatigue cracks as seen in cross-sectional scanning electron microscope images with their simulated representations. Using this comparison method, a parameter study provides a well-fitting set of parameters for the fatigue laws employed.

Finally, the calibrated framework is applied to larger structures featuring more realistic boundary conditions. The results are promising, regarding the positions of the predicted fatigue cracks and the associated load cycle numbers. While further research for a broader range of loading conditions is needed to verify the feasibility of the framework, the work presented here is an important step in the development of a physical lifetime model for power semiconductor devices.

Kurzfassung

Leistungshalbleiter sind integrale Bestandteile in einer Vielzahl von Geräten und Bauteilen. Da die Anforderungen an die Zuverlässigkeit von Leistungshalbleitern aufgrund sinkender Bauteilgrößen und neuer Anwendungsbereiche, z. B. in der erneuerbaren Energieerzeugung, steigen, werden neue Methoden zur Vorhersage von Ermüdungsschäden immer wichtiger. Unter den zahlreichen Versagensarten, die in Leistungshalbleitern auftreten können, befasst sich diese Arbeit mit der thermomechanisch induzierten Rissbildung in einer Kupfermetallisierungsschicht aufgrund zyklischer Überlastungsimpulse. Um dieses Problem numerisch beschreiben zu können, wird ein bestehendes, auf Kontinuums-Schädigungsmechanik basierendes physikalisches Lebensdauermodell angewandt, verbessert und kalibriert.

Im diesem Lebensdauermodell wird die lokale Ermüdungslebensdauer in zwei Phasen unterteilt, und zwar in jene der Initiierung und in jene der Ausbreitung der Schädigung. Beide Phasen werden durch ihre jeweiligen Ermüdungsgesetze und Parameter beschrieben. Um diese Parameter zu kalibrieren, muss ein aussagekräftiger Vergleich zwischen experimentellen und simulierten Ergebnissen hergestellt werden. Dafür müssen, neben einer adäquaten Darstellung der experimentellen Belastungsbedingungen, auch Methoden entwickelt werden, um die in Experimenten beobachteten Ermüdungsschäden zu quantifizieren, und um diese mit den in Simulationen vorhergesagten Ergebnissen vergleichen zu können.

In einem ersten Ansatz werden Binärbilder von Ermüdungsrissen, sichtbar auf der Oberfläche von thermomechanisch belasteten Prüfbauteilen, zur Bestimmung einer Ermüdungsrissdichte verwendet. Diese Ermüdungsrissdichte wird in Verbindung mit entsprechenden Simulationen herangezogen, um die Parameter des Modells zur Initierung zu kalibrieren.

Außerdem wird der Einfluss von lokal unterschiedlichen Maximaltemperaturen und mechanischen Spannungskonzentratoren wird untersucht. Die experimentellen Ergebnisse zeigen, dass sich ausgeprägte Ermüdungsrisse auch abseits von Spannungskonzentratoren bilden, was durch das ursprüngliche physikalische Lebensdauermodell nicht wiedergegeben werden kann.

Um dieses Problem zu beheben, wird ein Konzept vorgestellt, das Informationen über die Mikrostruktur in das ursprüngliche Modell einführt und gleichzeitig den Simulationsaufwand in einem vertretbaren Rahmen hält. Hierbei wird die Orientierung der Korngrenzen an den Triplepunkten verwendet, um einen Parameter zu definieren, der die lokale Anfälligkeit für Porenbildung beschreibt. Der Einfluss dieses Parameters auf die vorhergesagte Entstehung von Ermüdungsrissen wird untersucht und diskutiert.

Um diesen verbesserten Ansatz zu kalibrieren, wird eine zweite Vergleichsmethode vorgestellt, mit welcher die Anzahl der in Querschnittsbildern detektierten Ermüdungsrisse, mit Simulationsergebnissen verglichen wird. Unter Verwendung dieser Methode liefert eine Parameterstudie einen passenden Satz von Parametern für das verwendete Lebensdauermodell.

Schließlich wird das kalibrierte Modell auf größere Strukturen mit realistischeren Randbedingungen angewandt. Die Ergebnisse sind vielversprechend, was die Positionen der vorhergesagten Ermüdungsrisse und die damit verbundenen Lastwechselzahlen betrifft Obwohl weitere Untersuchungen für einen breiteren Bereich von Belastungsbedingungen erforderlich sind, um die Anwendbarkeit des hier präsentierten Ansatzes zu überprüfen, ist dieser ein wichtiger Schritt in der Entwicklung eines umfassenden physikalischen Lebensdauermodells für Leistungshalbleiterbauelemente.

Notations

Abbreviations

2D	...	Two–Dimensional
3D	...	Three–Dimensional
Al	...	Aluminum
APC	...	Active Power Cycling
APDL	...	ANSYS Parametric Design Language
CDM	...	Continuum Damage Mechanics
CTE	...	Coefficient of Thermal Expansion
Cu	...	Copper
DMOS	...	Double–diffused Metal–Oxide–Semiconductor
DMOSFET	...	Double–diffused Metal–Oxide–Semiconductor Field–Effect Transistor
DUT	...	Device Under Test
EBSD	...	Electron Backscatter Diffraction
ELM	...	Empirical Lifetime Model
FEM	...	Finite Element Method
FIB	...	Focused Ion Beam Technique
FIP	...	Fatigue Indicator Parameter
FS	...	Fatemi–Socie
HCF	...	High Cycle Fatigue
IGBT	...	Insulated–Gate Bipolar Transistors
KAI	...	Kompetenzzentrum Automobil- und Industrieelektronik GmbH
LCF	...	Low Cycle Fatigue
PLM	...	Physics-of-failure Lifetime Model
MCC	...	Minimum Circumscribed Circle
MDM	...	Maximum Damage Method
MOSFET	...	Metal–Oxide–Semiconductor Field–Effect Transistor

MSE	...	Mean Squared Error
SEM	...	Scanning Electron Microscope
Si	...	Silicon
SiO_2	...	Silicon Dioxide
SiN	...	Silicon Nitride
SWT	...	Smith–Watson–Topper
TMF	...	Thermo–Mechanical Fatigue

Symbols of recurring Latin Letters

a_φ	...	constant of the function describing the susceptibility of damage due to misorientation angles
b_γ	...	shear fatigue strength exponent
b_φ	...	constant of the function describing the susceptibility of damage due to misorientation angles
c	...	specific heat capacity
c_γ	...	shear fatigue ductility exponent
c_γ^*	...	calibrated shear fatigue ductility exponent
C_1	...	plasticity parameter for the Chaboche kinematic hardening model
$d_{\mathrm{surf}}^{\mathrm{exp}}$	...	experimental surface damage variable
$d_{\mathrm{surf}}^{\mathrm{sim}}$	...	simulated surface damage variable
D_{E}	...	damage evolution variable
$D_{\mathrm{mean}} = D_{\mathrm{mean}}^{\mathrm{sim}}$		mean damage evolution variable of a cross-section
D_{O}	...	damage onset variable
$D_{\mathrm{surf}}^{\mathrm{exp}}$	...	normalized experimental surface damage variable
$D_{\mathrm{surf}}^{\mathrm{sim}}$	...	normalized simulated surface damage variable
$\bar{D} = \bar{D}^{\mathrm{sim}}$	...	mean of multiple $D_{\mathrm{mean}}^{\mathrm{sim}}$ variables
$\bar{D}^{\mathrm{exp}}$	...	mean experimental cross-section damage variable
$\bar{D}_{\mathrm{cl}}^{\mathrm{exp}}$	...	mean experimental crack-length per area
$\bar{D}_{\mathrm{msh}}^{\mathrm{exp}}$	...	$\bar{D}^{\mathrm{exp}}$ variable after mesh size adjustment
$\bar{D}_{\mathrm{skl}}^{\mathrm{exp}}$	...	$\bar{D}^{\mathrm{exp}}$ variable after skeletonization
$\bar{D}_{\mathrm{cl}}^{\mathrm{sim}}$	...	mean simulated crack-length per area
$\bar{D}_{\mathrm{skl}}^{\mathrm{sim}}$	...	$\bar{D}^{\mathrm{sim}}$ variable after skeletonization
$e_{\mathrm{d,skel}}$	...	number of elements which are counted as damaged after the skeletonization
E, E_i	...	Young's moduli

$\widetilde{E}$, $\widetilde{E}_i$	...	Young's moduli of the damaged material
g	...	least square error estimate
G, G_{ij}	...	shear moduli
l	...	characteristic element length
n	...	number of data points for MSE
n_i	...	number of cycles in a load block i
N	...	load cycle number
N_{E}	...	number of cycles in the damage evolution stage
N_{F}	...	total fatigue life (number of cycles to fatigue failure)
N_{N}	...	total number of cycles for local material failure
N_{O}	...	number of cycles until damage onset
N^{exp}	...	load cycle number at which damage in an experimental cross-section image is evaluated
$P(t)_{\mathrm{Poly}}$	...	power introduced into the polysilicon
$\dot{q}_V(t)$	...	volumetric heat generation rate
r	...	shape value of the function describing the susceptibility of damage due to misorientatio
s	...	parameter describing the susceptibility of the material to the formation of voids
s_φ	...	s parameter based on misorientation angle
s_{tp}	...	s parameter of triple junction
s_{elem}	...	s parameter of element
px	...	pixels in an experimental cross-section image
px^d	...	pixels classified as damaged in an experimental cross-section image
t	...	time
T_{exp}	...	experimentally measured temperature at the temperature sensor
T_{B}	...	base temperature during poly-heater experiments
T_{bottom}	...	boundary temperature at bottom nodes
T_{P}	...	peak temperature during poly-heater experiments
T_{sim}	...	simulated temperature at the temperature sensor
V_{Poly}	...	volume of the polysilicon
$\Delta \mathrm{w}$	...	inelastic strain energy density
$\Delta \mathrm{w}_{\mathrm{mod}}$	...	modified inelastic strain energy density accounting for the hydrostatic pressure
$\Delta \mathrm{W}$	...	strain energy of all elements during one cycle
$\delta \mathrm{W}_{i,i-1}$	...	dissipated strain energy between two consecutive LCs
x_i	...	position of the experimental data points in the surface analysis

Symbols of recurring Greek Letters

α	...	coefficient used to adjust the inelastic strain energy
γ_{f}'	...	shear fatigue ductility coefficient
γ_{f}^{*}	...	calibrated shear fatigue ductility coefficient
γ_1	...	plasticity parameter for the Chaboche material model
$\Delta\gamma_{\max}$	...	maximum shear strain amplitude
$\boldsymbol{\varepsilon}$	...	total strain tensor
κ_1, κ_2	...	material parameters of the modified damage evolution law
$\varkappa$	...	material property in the FS criterion
λ	...	thermal conductivity
μ_{Gauss}	...	Gauss mean or expectation of the distribution
ν, ν_{ij}	...	Poisson's ratios
ρ	...	density
σ_{Gauss}	...	Gauss standard deviation
$\sigma_{\mathrm{H}}^{\max}$	...	maximum hydrostatic pressure
$\sigma_n^{\max}$	...	maximum normal stress acting on the plane of $\Delta\gamma_{\max}$
σ_{Y}	...	yield stress in the FS fatigue law
$\sigma_{\mathrm{Y,chab}}$	...	yield stress in the Chaboche model
$\boldsymbol{\sigma}$	...	Cauchy stress tensor
τ_{f}'	...	shear fatigue strength coefficient
φ	...	misorientation angle

Chapter 1

Introduction

1.1 Motivation

The topic of energy efficiency and sustainable energy consumption is gaining more and more importance in today's world, where the effects of climate change are omnipresent. While a switch to renewable energy sources and an overall reduction of CO_2 emissions is inevitable and also recognized in modern society and governmental policies, a decrease of carbon footprint through the use of more energy-efficient systems is often overlooked [78]. Power semiconductors, responsible for controlling, converting, and conditioning energy, play an important role in improving energy efficiency [11, 49, 92, 97]. Power semiconductors can be found in most electronic devices [41], with some studies estimating that more than 70% of electricity is processed through power semiconductor devices [102]. Given the trend towards smart grid solutions, this number is expected to increase and the power semiconductor market is expected to grow further [56, 65].

With such high demand across a wide range of applications, it is obvious that the reliability of power semiconductor devices is a topic of great relevance [23, 101], with standardized tests having been established for common silicon (Si) device technologies over the past decades [57]. Nevertheless, requirements for reliability increase due to multiple reasons. For example, the use of power semiconductor devices in the field of regenerative power

generation (wind turbines and photovoltaic systems) places new and higher demands on the devices employed [4, 13, 58]. Furthermore, newer generations of power semiconductors are designed to operate at higher power densities, which places additional stress onto the devices.

The causes which can lead to reliability issues are manifold and range from Thermo-Mechanical Fatigue (TMF) [107], humidity-induced failure [53], to cosmic ray failures [109]. From all reliability issues, TMF is reported to be the most critical one [23]. The main cause for TMF is power dissipation during overload pulses, which lead to high temperatures in the devices. Due to different coefficients of thermal expansion (CTE) of the employed materials, this leads to high thermal stresses and strains.

The most common method for experimentally quantifying TMF and determining the lifetime of power semiconductor devices are Active Power Cycling (APC) tests [30, 31, 40, 57, 88]. During these tests, a current is passed through the devices that mimics realistic stress states. In [57], three main failure mechanisms caused by TMF and observed in APC tests are distinguished: (i) Bond wire degradation, (ii) reconstruction or degradation of the metallization layer, and (iii) solder fatigue. Additionally, fatigue delamination between the various layers of the semiconductor devices is observed, e.g. [32, 42, 60, 62, 79, 87, 99, 100].

While for insulated–gate bipolar transistors (IGBT) the predominant failure modes are already well studied, the failure modes of metal–oxide–semiconductor field–effect transistors (MOSFET) devices and double-diffused MOSFET (DMOSFET) are analyzed in fewer publications [21]. In IGBT devices solder joint fatigue and bond wire degradation are most reported in the literature [9, 38, 54, 55, 107, 108] whereas for DMOSFET devices, degradation and fatigue crack propagation in the source metallization layer is one of the most important reliability issues to be addressed [63]. A schematic representation of a DMOSFET device is shown in Figure 1.1 together with a Scanning Electron Microscope (SEM) image depicting fatigue cracks in the metallization layer.

Most commonly the reliability of power semiconductors is quantified and described by the means of Coffin-Manson law type lifetime predictions based on APC experiment and

statistics. A wide range of similar modeling approaches of this type have been proposed, all relating temperature swings and average device temperatures to the number of cycles to failure [30, 54]. The individual modeling approaches differ in the number of additional influencing factors included. Such Empirical Lifetime Models (ELMs) have been a sufficient way to predict the lifetime of products for a long time, but due to the aforementioned increasing demands on power semiconductors, new ways to describe and predict the fatigue life are sought after. The main problem of the most commonly used ELMs is that they do not differentiate between the different failure modes. While there are some ELMs calibrated and designed to give cycle to failure numbers for specific failure modes [39, 85], the need to reliably predict the progression of these failure modes has led to the development of so-called Physics-of-failure Lifetime Models (PLM). In contrast to ELMs which are based on experiments and statistics, PLMs aim to simulate the failure number within a numerical

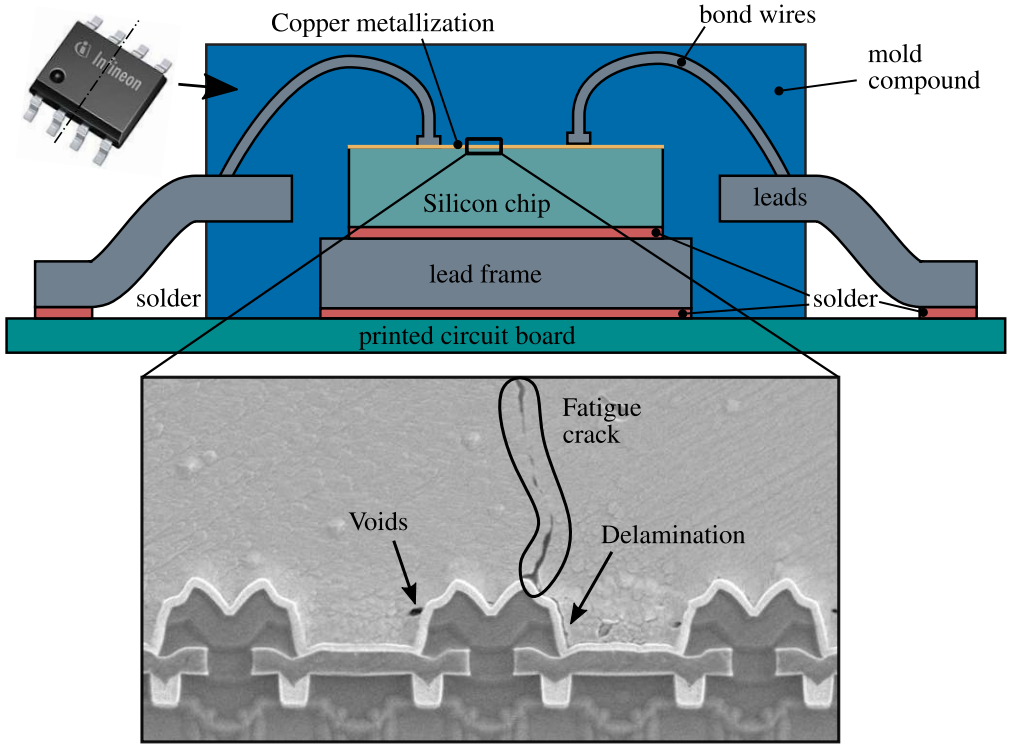

Figure 1.1: Schematic representation of the different parts of a power semiconductor device and SEM image highlighting fatigue damage in the Cu metallization layer. (Taken and modified from [47, 93])

framework based on constitutive laws and the stress and strain response due to the thermal loading. However, these models are also not entirely independent of experimental results as the parameters of such models need to be calibrated based on experimental results. There are significant challenges associated with these types of models, such as the complex nature of the fatigue failure modes, the accurate material characterization necessary for all layers of the devices, and the non-standardized calibration of material parameters. Nevertheless, well-formulated and calibrated PLMs give additional insights into the fatigue behavior and allow predictions for different loading scenarios and boundary conditions.

This work focuses on PLMs for simulating the formation and propagation of fatigue cracks in the copper-source metallization layer of DMOSFET devices. The Copper (Cu) metallization layer acts not only as an electrical connection but also as a heat sink [10, 69]. Its heat dissipation capabilities are important to prevent that repeated power pulses lead to thermal runaway and subsequent overheating of the Si chip [80]. Material degradation and crack formation in the Cu metallization can impede the heat conductivity of the material. Especially, through-film cracks can act as free-edges for the initiation of delamination [28] between the metallization and the underlying layers. This in turn can lead to the formation of hot-spot areas in the Si, causing device failure [17, 18, 76]. A PLM which reliably predicts weak spots and the number of cycles until through-film cracks appear can help in the design of more reliable products and save costs in the process.

1.2 State of the art

Since the general field of reliability analyses of power semiconductors is too extensive to be covered here, this section focuses on relevant studies regarding the analysis of fatigue damage in the Cu metallization layer of DMOSFET devices. A number of PhD theses have been published as more or less direct precursors to this thesis. In [46] nonlinear elector-thermal analyses of semiconductor devices have been conducted focusing on material characterization, where a good agreement between experimental and numerical results has been achieved. Further electro-thermal simulations of test devices have been conducted

in [22, 44], including comparison with experimental results obtained by infrared tomography. The simulation aspect of this work concentrates on homogenization concepts and the modeling of non-matching grid interfaces. It has been shown that these modeling approaches have the potential to overcome multiscale complexity restrictions. In [16] the focus has been on electro-thermal simulation concepts. Among other results, this work also highlights how cracks in the metallization layer cause the formation of hot spots. Further numerical studies (as well as experimental ones) have been conducted in [75], including the modeling of fatigue degradation of the solder layer. Extensive experimental analyses of thermo-mechanical Cu film fatigue are presented in [10], with emphasis on the influence of inorganic residues.

Important experimental analysis of Cu metallization layers have been published in [1, 2, 66, 67, 70, 90, 98]. Therein, so-called poly-heater device studies are presented, focusing mostly on the formation of fatigue damage in the bulk material of the copper metallization layer. The main features of poly-heater devices are the name giving poly-silicon resistor layers which are used to perform fast *in situ* heating. In [50] such studies are additionally accompanied by numerical simulations to verify experimentally measured temperatures. Additional studies of micron-sized Cu structures have been published in [82, 105, 106]. Here, mechanical studies of thin-film Cu structures are performed in the low cycle fatigue (LCF) and high cycle fatigue (HCF) regime and the resulting loss of material integrity is described and discussed. Due to the fact that Aluminum (AL) metallization layers exhibit similar aging and degradation behavior to Cu metallization layers, it is important to reference studies such as [20, 77, 81]. Only a few physical lifetime analyses of Cu metallization layers have been published, many of them being preceding studies to this work [33, 34, 47, 48, 91, 93–96].

Here, the two theses [47, 93] should be highlighted, which form the cornerstones of the present work. In [47] various Continuum Damage Mechanics (CDM) based Fatigue Indicator Parameters (FIP) have been reviewed and applied to a submodel of a DMOS device, showing that cracks initiate at the position of mechanical stress concentrators. Additionally, a fatigue delamination propagation modeling method utilizing a cohesive zone modeling

approach has been discussed. Both approaches show good agreement with experimentally observed crack nucleation sites. In [93] the fatigue indicator parameters have been utilized to model fatigue onset and fatigue damage evolution in the bulk metallization. Furthermore, the cohesive zone modeling approach has been reworked to be able to be calibrated and model inter film delamination.

For [47, 93] a comparison with TMF experiments and a calibration of the required material parameters has been out of scope. Moreover, the initiation of fatigue damage modeled by the approach presented in [93] is strongly dependent on mechanical stress concentrators while experiments also show fatigue cracks that form in the absence of such stress concentrators.

1.3 Scope of the present work

The overall goal of the present work is to model fatigue damage in the Cu metallization layer within the framework of the Finite Element Method (FEM). For this purpose, the existing frameworks presented in [47, 93] are being utilized and extended. Methodologies are developed for comparing the results of numerical analyses with those of experimental ones. Based on such comparisons, the parameters of the fatigue modeling framework are calibrated. To achieve these objectives, several aspects have to be considered, which make modeling fatigue damage in semiconductors a challenging task.

- **Inhomogeneous temperature fields:** Fatigue damage in power semiconductor devices is the result of complex electro-thermo-mechanical interactions. The general influence of the temperature on the fatigue damage has been researched quite well but the influence of locally different temperatures in one device is a relatively novel topic [91]. To model the occurring thermal gradients, it is necessary to adequately represent the thermal loading conditions.
- **Comparison with experiments:** For the calibration of physical fatigue damage models, standardized experimental procedures are used in most cases, which allow the fatigue crack propagation to be observed in situ. In the case of metallization

degradation, neither standardized experimental testing procedures are available, nor is the fatigue damage onset and evolution inside the metallization layer easily observable.

- **Influence of the microstructure and device size:** The fatigue damage in the metallization layer is similar in scale to the grain size of the Cu, which implies that the microstructure plays a role in the fatigue life. This must be reflected to some extent by the modeling approach. However, computational requirements should be reasonable, since a modeling approach is desired that can also be used in simulations of larger structures.

1.4 Outline of the thesis

Chapter 2 provides a brief overview of the fatigue damage modeling framework developed in [47, 93].

In Chapter 3 the modeling approach presented in Chapter 2 is extended to model fatigue damage under transient thermal loading conditions. A study of a cluster of multiple DMOS cell-like structures is presented, which highlights the influence of lateral thermal gradients.

Chapter 4 focuses on the formation of fatigue damage visible on the surface of poly-heater test devices and its numerical prediction. A strategy for calibrating material parameters of the numerical fatigue approach using experimental results from TMF experiments is presented here and predictions about fatigue damage in a second device are made.

Chapter 5 presents a novel concept of introducing information of the microstructural descriptors into the fatigue modeling framework. The misorientation angles at the position of triple junctions are used to define weak spots in the bulk material. In addition, a preliminary parameter study is being conducted.

In Chapter 6 results of the extended fatigue modeling framework introduced in Chapter 5 are compared to experimental results obtained by poly-heater power cycling. For this purpose, the amount of fatigue damage visible in cross-sections is quantified in terms of crack length per area. The results are used for calibrating parameters of the fatigue modeling framework.

Finally, in Chapter 7 the results are summarized and a brief outlook into possible future work is given.

Chapter 2

Theoretical Background

2.1 Introduction

This chapter provides a brief overview of the Continuum Damage Mechanics (CDM) based bulk fatigue damage modeling framework developed in [93] which is a succession to the Fatigue Indicator Parameter (FIP) studies presented in [47]. For a more detailed explanation of the framework, please refer to [93].

The goal of the present work is to predict fatigue damage in metallization layers of power semiconductor devices. In modern applications, these layers are usually made of fine-grained Cu and have a thickness of several micrometers. The main causes for the formation of fatigue cracks in these layers are stresses and strains due to thermal heat up during repeated overload pulses and the different coefficients of thermal expansion of the Cu metallization and the underlying layers. This type of loading leads to complex multiaxial stress and strain conditions, which pose a significant challenge for the physical prediction of fatigue damage in metallization layers. While uniaxial lifetime-models work in cases where the principle axes of stresses and strains are consistent in their orientation throughout the whole fatigue life, it is assumed that the multiaxiality of the stress and strain states introduced by TMF loading conditions is too pronounced to make usage of such models. Various multiaxial fatigue models have been proposed in the literature [12, 25, 89] to account for such loading

conditions, whereby it depends on the material response which model is suitable for a specific load case.

In general, repeated cyclic loading can result in a pure elastic response, linear elastic shakedown, stabilized plastic cycling, or plastic ratcheting. The loading scenario of overload pulses is characterized by very high temperatures during very short time periods. The temperatures are high enough to induce thermal stresses that cause plastic deformation in the metallization layer, but the time periods are too short for significant plastic creep. Therefore, the material response is characterized by stabilized plastic cycles which evolve as fatigue damage progresses. This material response is characteristic for LCF [8].

The well-accepted theory of Brown [12] states that in case of complex LCF loading situations, it is advantageous to split the local fatigue life into two stages. Stage I is the part of the fatigue life, characterized by void accumulation at grain boundaries and the nucleation of microcracks. The driving forces are shear strains acting at critical crystal planes. These microcracks or voids are too small to cause measurable degradation of the material on structural level. During Stage II the microcracks and voids begin to grow significantly and coalesce into larger macrocracks that eventually compromise the local integrity of the material. These two stages of local fatigue life can be summarized as the fatigue crack initiation.

The two stages of fatigue life are also reflected in the CDM based fatigue modeling framework presented in [93]. To address the two stages, phenomenological fatigue damage criteria are used. To capture Stage I, subsequently called damage onset, a Fatemi–Socie (FS) critical plane criterion is employed. The evolution of damage during Stage II is captured using a standard damage evolution law based on the inelastic strain energy density as a driving force.

Damage onset and damage evolution are evaluated locally for each material point of interest, where the lifetime of each material point can be described as

$$N_{\mathrm{N}} = N_{\mathrm{O}} + N_{\mathrm{E}} \tag{2.1}$$

with N_{N} being the total number of load cycles until local material failure occurs, N_{O} the number of cycles until damage onset i.e. a microcrack of a certain size has nucleated, and N_{E} is the number of load cycles for damage evolution until the material is fully damaged.

2.2 Damage onset

Fatemi-Socie critical plane criterion

The FS critical plane criterion is employed to describe damage onset. This criterion is used because its formulation is based on the shear strain amplitude, which is considered to be the driving force for Stage I fatigue cracking [12]. The FS FIP [26] for a given fatigue life is originally expressed as

$$\frac{\Delta\gamma_{\max}}{2}\left(1+\varkappa\frac{\sigma_n^{\max}}{\sigma_{\mathrm{Y}}}\right)=\text{constant} \tag{2.2}$$

where $\Delta\gamma_{\max}$ is the maximum shear strain amplitude and $\sigma_n^{\max}$ is the maximum normal stress on the $\Delta\gamma_{\max}$ plane. The material properties σ_{Y} and $\varkappa$ are the yield stress of the material and a material property describing the influence of the normal stress on the fatigue damage, respectively. The critical plane is defined here as the plane experiencing the maximum shear strain amplitude.

Commonly, the FS fatigue criterion is formulated in the traditional strain-life equation format [25]

$$\frac{\Delta\gamma_{\max}}{2}\left(1+\varkappa\frac{\sigma_n^{\max}}{\sigma_{\mathrm{Y}}}\right)=\underbrace{\frac{\tau_{\mathrm{f}}'}{G}(2N_{\mathrm{F}})^{b_\gamma}}_{\text{HCF}}+\underbrace{\gamma_{\mathrm{f}}'(2N_{\mathrm{F}})^{c_\gamma}}_{\text{LCF}} \tag{2.3}$$

with a Basquin's equation term for HCF and a Coffin-Manson term for LFC on the right side. The parameter G is the shear modulus, τ_{f}' and b_γ denotes the fatigue strength coefficient and exponent, respectively and γ_{f}' and c_γ are the fatigue ductility coefficient and exponent, respectively. Generally, N_{F} describes the number of cycles until a certain "failure" criterion is reached. Because in the given framework the FS criterion is used to describe

the number of cycles for damage onset, N_F is replaced by N_O which describes the number of cycles until microcracks grow to a certain size and damage evolution sets in.

Since variable amplitude loading and also possible load direction changes are to be expected in case of power semiconductor TMF, the critical plane is not defined to be the plane experiencing the maximum shear strain amplitude $\Delta\gamma_\mathrm{max}$. Instead, it is defined as the plane experiencing the highest FIP value as proposed in [7] as the Maximum Damage Method (MDM). It reads

$$\left\{ \underbrace{\frac{\Delta\gamma}{2}\left(1+\varkappa\frac{\sigma_n^\mathrm{max}}{\sigma_\mathrm{Y}}\right)}_{\mathrm{FIP}} \right\}_\mathrm{max} = \underbrace{\frac{\tau_\mathrm{f}'}{G}(2N_\mathrm{O})^{b_\gamma}}_{\mathrm{HCF}} + \underbrace{\gamma_\mathrm{f}'(2N_\mathrm{O})^{c_\gamma}}_{\mathrm{LCF}} \quad . \tag{2.4}$$

The scope of the framework is in the range of LCF with large plastic deformations, therefore the HCF-Basquin part of the equation (2.4) is neglected and only the LCF-Coffin-Manson part is used subsequently. Although the cycle number for damage onset, N_O, can be calculated directly with this simplification, it is not a straightforward task. The critical plane is not known *a priori* and has to be determined from all planes considered, which is a computationally intensive task. The mathematical procedure of identifying the critical plane is described in detail in [47, 93] and only a brief summary of the procedure is given here.

From the infinite number of possible critical planes, a finite number of planes j are considered as possible critical planes. These planes are oriented in an icosahedral discretization of a hemisphere. For each of them the individual maximal FIP is calculated. In this case, the FS criterion reads as

$$\max_j \left\{ \left[\frac{\Delta\gamma}{2}\left(1+\varkappa\frac{\sigma_n^\mathrm{max}}{\sigma_\mathrm{Y}}\right) \right]_j \right\} = \gamma_\mathrm{f}'(2\cdot {}^{(j)}(N_\mathrm{O}))^{c_\gamma} \quad , \tag{2.5}$$

whereas j indicates the considered plane. Since the loading is in general non-proportional, $\Delta\gamma$ can not be calculated directly, and has to be obtained solving a non-trivial optimization problem. In the implementation of the framework in [93] the Minimum Circumscribed Circle (MCC) method is utilized as proposed in [73].

If the loading conditions changes during APC, Equation (2.5) has to be used together with a damage accumulation rule to determine the critical plane. In the following, a linear Palmgrem-Miner damage accumulation [64, 72] rule is employed given as

$$ {}^{(j)}D_{\mathrm{O}} = \sum_{i=1}^{m} \frac{n_i}{{}^{(j)}(N_{\mathrm{O}})_i} \,, \tag{2.6} $$

where j indicates again the considered plane and i the sequence of m load blocks. ${}^{(j)}(N_{\mathrm{O}})_i$ is calculated from Equation (2.5) and corresponds to the number of cycles until fatigue damage onset for load block i and the considered plane j. The number of load cycles of each individual load block is denoted by n_i. The resulting damage variable ${}^{(j)}D_{\mathrm{O}}$ describes the damage onset status of each individual plane. When

$$ \max_{j} \left\{ {}^{(j)}D_{\mathrm{O}} \right\} = 1 \,, \tag{2.7} $$

is reached, the critical plane is identified being the one first reaching this criterion, and the damage onset criterion is fulfilled.

2.3 Damage evolution

After the damage onset criterion is fulfilled and the damage onset variable D_{O} has reached 1 in the critical plane, damage evolution starts. Damage evolution is defined to be the growth and coalescence of microcracks that lead to a loss of local material integrity. To model this part of the fatigue life, an energy-based fatigue criterion is used in the modeling framework proposed in [93]. Such criteria have been shown to provide a reasonable prediction damage evolution for TMF problems [24, 29, 36, 104].

The basis for such an approach is the specific inelastic strain energy dissipated in one stabilized cycle [27], which is calculated as

$$ \Delta w = \int_{1\,\mathrm{cycle}} \boldsymbol{\sigma} : \dot{\boldsymbol{\varepsilon}} \; \mathrm{d}t \quad , \tag{2.8} $$

where $\boldsymbol{\sigma}$ is the stress tensor, $\dot{\boldsymbol{\varepsilon}}$ the rate of the strain tensor and t is the total time of one cycle.

Modifications for Δw have been proposed in the literature [59, 74] to account for different factors which can have an impact on the fatigue life, e.g. corrections for mean stress effects. The framework proposed in [93] utilizes the modification introduced in [3] which accounts for the hydrostatic pressure, reading

$$\Delta w_{\mathrm{mod}} = \Delta w + \alpha \sigma_{\mathrm{H}}^{\mathrm{max}} \,, \tag{2.9}$$

with α being a material property which has to be obtained from experiments and $\sigma_{\mathrm{H}}^{\mathrm{max}}$ being the maximum hydrostatic pressure. The damage evolution is defined by a damage variable D_{E} calculated with a standard damage evolution law as used in commercial FEM software. Based on the work of [14, 52] the damage evolution law is formulated as

$$\frac{\mathrm{d}D_{\mathrm{E}}}{\mathrm{d}N} = \frac{\kappa_1}{l}(\Delta w_{\mathrm{mod}})^{\kappa_2} \,. \tag{2.10}$$

where l is the characteristic element length and κ_1 and κ_2 are material parameters. The damage evolution variable D_{E} can then be obtained by integration of Equation (2.10) as

$$D_{\mathrm{E}} = \int_{N_{\mathrm{O}}}^{N} \frac{\kappa_1}{l}(\Delta w_{\mathrm{mod}})^{\kappa_2} \mathrm{d}N \,. \tag{2.11}$$

The number of cycles from the beginning of damage evolution ($D_{\mathrm{O}} = 1, D_{\mathrm{E}} = 0$) until a predicted loss of material integrity ($D_{\mathrm{O}} = 1, D_{\mathrm{E}} = 1$) is N_{E}. In CDM the meaning of the damage variable D_{E} is a reduction of material integrity, while the physical meaning is the growth of microcracks. There are many approaches how the damage variable influences the effective material properties. Theoretically, anisotropic damage modeling would be favorable in combination with the critical plane obtained during the damage onset as the orientation of the anisotropy can be based on the orientation of the critical plane. Further details on anisotropic damage modeling and preliminary numerical studies are presented in

[93] following [68]. Due to the *a priori* unknown orientation of the critical planes, such an approach cannot be easily implemented.

In this work a in [93] stated simplified isotropic damage model is utilized in which the effective elastic engineering parameter reads

$$\widetilde{E} = (1 - D_{\mathrm{E}})^2 E, \tag{2.12}$$

with other material parameters such as thermal conductivity, density and the yield stress of the material being reduced equivalently. The Poisson's ratio, the CTE and the heat capacity are not impeded by the progressing damage.

2.3.1 Numerical implementation

The fatigue modeling approach has been implemented in the framework of Ansys APDL v20.2. The fatigue simulation is performed using element stress and strain values calculated as the average of the nodal values. This means the smallest damaged entities are whole elements for which the material degradation is realized as a change of material cards. The fatigue simulation is based on stabilized plastic cycles. The stabilized cycles are identified by monitoring two consecutive cycles and calculating the change in dissipated inelastic strain energy density as

$$\delta W_{i,i-1} = \frac{\Delta W_i - \Delta W_{i-1}}{\Delta W_{i-1}} \tag{2.13}$$

with ΔW_i and ΔW_{i-1} being the dissipated inelastic strain energy density of all elements considered in the fatigue framework during the two consecutive cycles $(i-1)$ and (i), respectively. If $\delta W_{i,i-1}$ is lower or equal to a threshold value of 1%, a stabilized cycle is assumed and the fatigue simulation is initialized for all respective elements.

Although only LCF is considered in the simulation framework, it must be expected that several thousand cycles have to be simulated to model TMF in power semiconductors. This makes a cycle-by-cycle simulation not feasible, therefore a cycle jump technique has been

implemented in [93]. The cycle jump approach is based on the one described in [15] and explained more in detail in [93].

Chapter 3

Transient Thermo-mechanical Bulk Fatigue

3.1 Introduction

While the in Chapter 2 presented approach has been applied to mechanical fatigue problems [94] and to simplified submodels of thermo-mechanical loaded DMOSFET cells [95], it has not yet been tested together with non-uniform thermal loads. Such non-uniform thermal loads can lead to lateral thermal gradients within the device, which influence the fatigue behavior [91].

In this chapter, the existing framework is extended towards transient thermal loading conditions. The transient thermal and mechanical fields are treated in a sequentially coupled analysis that allows to be capture the effects of developing fatigue damage on the thermal fields. This enables the investigation of clusters of multiple DMOS cell-like features with lateral thermal gradients. Shielding effects and the influence of non-trivial thermal boundary conditions on the formation and propagation of fatigue cracks are investigated in such arrangements. This chapter is based on Hoffmann et al. 2020 [33].

3.2 Transient thermal loading

The CDM framework as presented in Chapter 2 allows to model fatigue damage under cyclic thermo-mechanical loading, where the thermal loads have to be specified by a set of predefined temperature fields. In order to be able to model the complex thermal loading conditions occurring in semiconductors, the framework has to be extended. Since time-dependent material behavior such as viscoplasticity is not considered in the current state and only one-sided coupling from the thermal to the mechanical fields is assumed, weak thermo-mechanical coupling is employed, as presented in Figure 3.1. The transient thermal analysis is conducted based on the material properties, the geometry, the given power pulse, and the boundary conditions. The spatial temperature fields are obtained for any time point in the load history. These temperature fields are subsequently used as temperature boundary conditions in the mechanical analysis, which is performed quasi-statically for each given time step of the transient analysis. Based on the mechanical analysis, the fatigue damage calculation can be conducted as explained in Chapter 2.

With this extension, it is possible to apply thermal boundary conditions that more realistically represent the thermal loading of a power semiconductor device. Heat can be

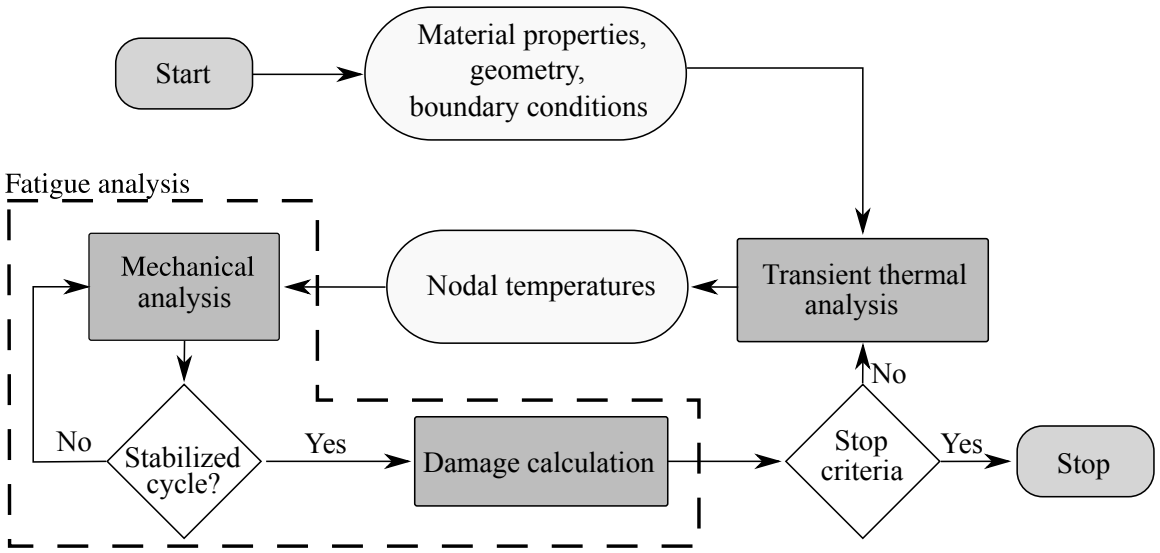

Figure 3.1: Simplified representation of the simulation procedure featuring the transient thermal loading conditions.

introduced into the system with a time-dependent power density equal to the thermal energy dissipation in the chip during APC. It is emphasized, that this also allows to capture the influence of propagating fatigue cracks on the temperature fields in a more realistic manner. With each increase in fatigue damage, the previously calculated temperature fields are outdated and the transient thermal analysis has to be redone under consideration of the evolving fatigue damage. With the updated temperature fields, a new mechanical analysis is conducted and the search for a stabilized cycle starts again.

3.3 Application

As representative examples, arrangements of DMOS cell-like features (see Figure 3.2) are used to show the capabilities of the framework. The complicated geometry of the DMOS cells is simplified since the goal of the studies presented in this chapter is not to predict the behavior of actual devices but to study the influence of theoretical lateral thermal gradients.

A two-dimensional (2D) generic geometry is chosen for the FEM simulation, see Figure 3.2. Eight DMOS cell-like features consisting of a Cu metallization layer and an Si substrate, subsequently called segments, are modeled. A part of the Si substrate acts as an active

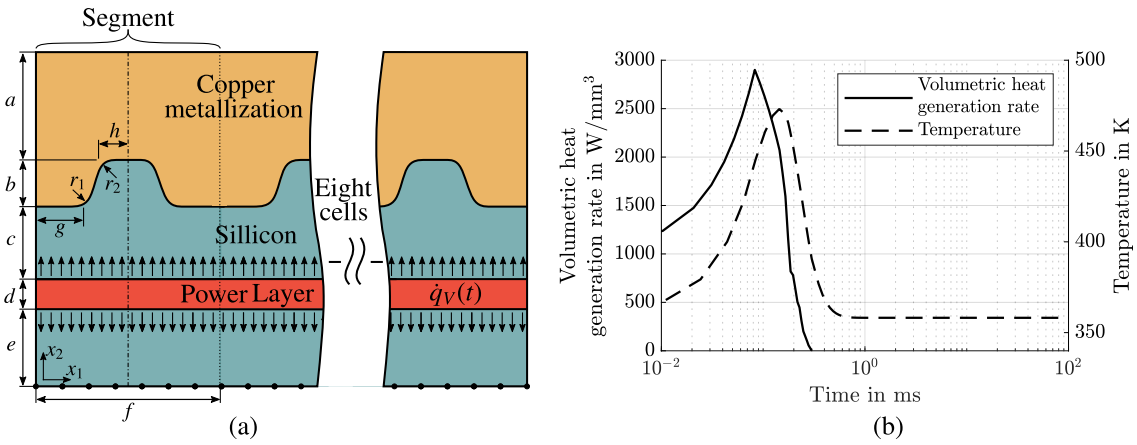

Figure 3.2: Schematic representation of the DMOS cell-like features (a). The volumetric heat generation rate $\dot{q}_V(t)$ in the power layer during one active cycle and the nodal temperature at the interface of the undamaged model (b).

Table 3.1: Dimensions of the model given in µm

a	b	c	d	e	f	g	h	r_1	r_2
21.7	3.2	5.1	5	30	12.8	3.8	1.9	1	1

Table 3.2: Estimated fatigue properties for Cu

$\varkappa$	γ_f'	c_γ	α	κ_1	κ_2
1	0.75	−0.45	0.0006	$1.9 \frac{10^{-6}\text{mm}}{\text{cycle}\,(\text{MPa})^{\kappa_2}}$	0.45

power layer that introduces thermal energy into the system. The dimensions are given in Table 3.1. A mesh consisting of isoparametric, linear interpolated, fully integrated, four noded, plane strain elements is used for discretization. The element size (edge length) is around 0.9 µm in the metallization layer and generally coarser in the Si substrate. It has to be mentioned that the mesh in the Cu layer is not regular, which means that there are small differences between the meshes of the individual segments. Material data for Si and Cu is taken from [94] and [47], and is summarized in Appendix A. The material properties of Si are given in Tables A.1 and A.2 and represent the material properties of a standard (100) silicon wafer which has the principle axes aligned with the crystal direction [100], [010], and [001]. For the given model, it is assumed that these axes are in turn aligned with the model axes $x_1 - x_2 - x_3$, see Figure 3.2. For the Cu metallization layer, the temperature independent elastic and thermal properties are defined in Table A.3. The plastic behavior is described using a temperature dependent Chaboche model. The corresponding parameters are listed in Table A.4. The whole model is assumed to be stress-free at room temperature, i.e. at T = 293 K, which is also the reference temperature for the CTEs. The required input parameters for the CDM fatigue framework have been determined in [95], based on micro cantilever experiments (see [105]). The properties are summarized in Table 3.2.

To highlight the capabilities of the modeling approach, different cluster configurations are presented, see Figure 3.3. These configurations do not represent the actual geometry and loading conditions of a semiconductor device, but are merely numerical test cases. All configurations have the same mechanical symmetry boundary conditions, which restrict

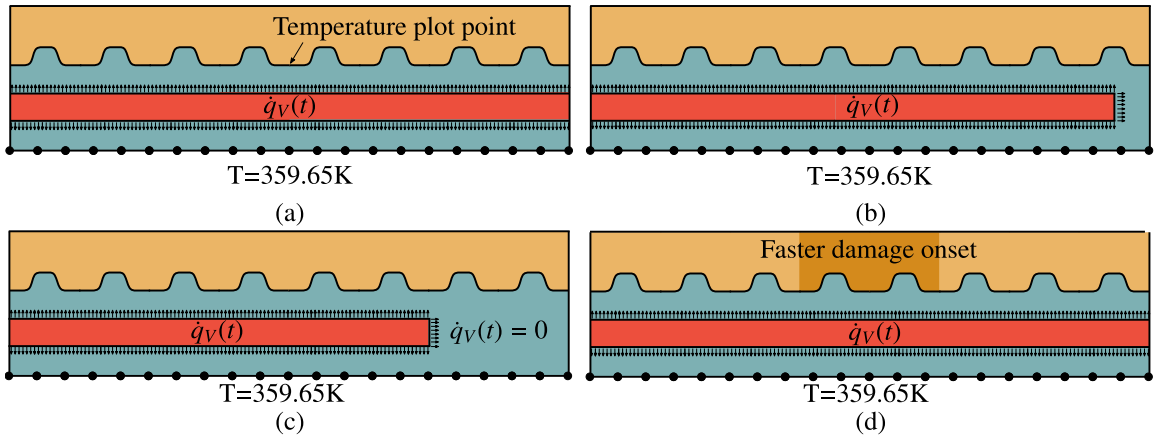

Figure 3.3: FEM models of DMOS cell-like features to study the influence lateral temperature differences (a-c) and locally accelerated fatigue damage onset (d) on the growth of fatigue cracks.

the displacement in the x_1-direction at the left and the right side, respectively. At the bottom nodes, the displacement in the x_2-direction is restricted. The thermal boundary conditions consist of a fixed temperature of T = 359.65 K at the bottom nodes, no heat transfer through the top, left, and right model boundary nodes and a volumetric heat generation rate, $\dot{q}_V(t)$, that introduces thermal energy into the power layer.

The model depicted in Figure 3.3 (a) represents the standard configuration, with heat generation in all eight segments. The volumetric heat generation rate, $\dot{q}_V(t)$, and the corresponding temperature result at the interface of Cu and Si in the middle of a representative segment (Figure 3.3(a)) are shown in Figure 3.2 (b). In the configuration depicted in Figure 3.3 (b)) a small lateral temperature difference between the segments is introduced by deactivating the heating beneath the rightmost half cell (i.e. beneath a full DMOS cell due to symmetry boundary conditions). A much stronger lateral temperature difference is introduced in the third load case, shown in Figure 3.3 (c), by deactivating the power layer beneath two cells. The last configuration, depicted in Figure 3.3 (d), focuses on a different aspect. While the thermal and mechanical boundary conditions are the same as the ones in the standard configuration shown in Figure 3.3 (a), the fatigue behavior of the two center

segments is modified. For these segments, fatigue damage onset is accelerated by 20%, i.e. a lower number of cycles N_{O} is necessary to initiate damage evolution.

3.4 Simulation results

The results of the different cluster configurations are presented and compared with respect to the fatigue cracks that emerge. In this chapter, fatigue cracks are defined as connected regions of elements where the damage evolution has led to a complete loss of material integrity and the local fatigue failure cycle number $N_{\mathrm{N}} = N_{\mathrm{O}} + N_{\mathrm{E}}$ has been reached. It is important to note that the used fatigue parameters have been obtained from experiments considering pure mechanical loading. Hence, the presented cycle numbers are rather qualitative in their character but allow for a direct comparison between the individual configurations.

3.4.1 Standard configuration

In the standard configuration, the thermo-mechanical load on each segment is the same. The only difference between the cells is the unstructured FEM mesh. At first, this leads to almost the same spatial FIP distribution for each of the eight segments, as can be seen in Figure 3.4. In this figure, and in all subsequent figures, dark blue indicates a high local FIP and light blue a low one. Since the FIP is directly related to damage onset, it can be

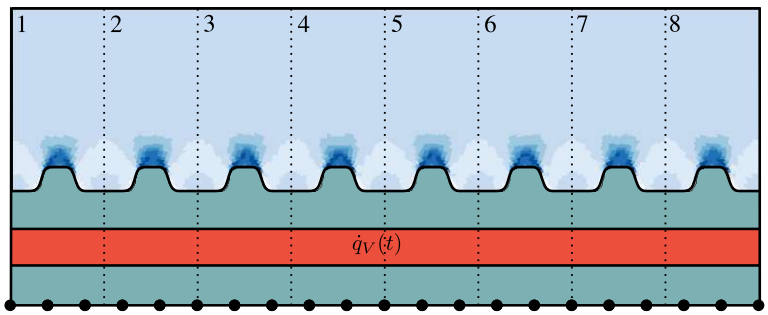

Figure 3.4: Distribution of FIP prior to the occurrence of fatigue cracks. Dark blue values indicate a high FIP, light blue values a low one.

expected that fatigue cracks emerge at locations with high FIP, in this case at the radii of the Si humps.

At which of the eight humps the first fatigue crack forms depends on the unstructured mesh. After 80 555 cycles, the first element in segment 4 has reached the local fatigue crack initiation cycle number N_{N}. The position is indicated in Figure 3.5 (a). After 84 651 cycles small fatigue cracks have emerged in all 8 segments. Up to about cycle number 106 160, all 8 individual fatigue cracks propagate at roughly the same speed, mostly growing upwards but also slightly downwards along the Cu-Si interface. Figure 3.5 (a) illustrates the fatigue crack pattern at this early stage. In this and in all following plots, the white areas are regions where the elements are completely damaged ($D_{\mathrm{E}} = 1$) and therefore a fatigue crack has formed. The coloring in the remaining part of the metallization layer again represents

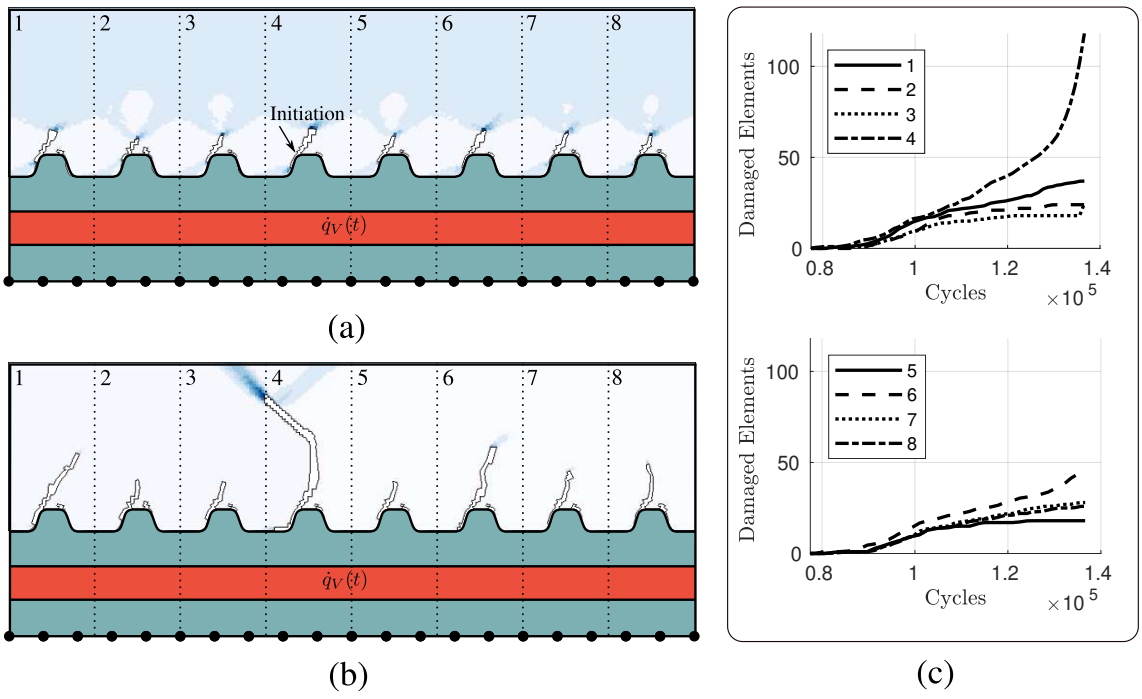

Figure 3.5: Fatigue damage characteristics of eight generic DMOS cell segments with lateral homogeneous thermal loading. Figure (a) shows the fatigue macro cracks and FIP values at cycle number 106 160. Dark blue values indicate a high FIP, light blue values a low one. Figure (b) shows fatigue macro cracks and FIP values at cycle number 136 620. In Figure (c) illustrates the evolution of the fatigue cracks in the different segments.

the FIP. At this stage, the FIP fields are already unevenly distributed between the eight segments. In segments 2, 3, 5, 7, and 8 regions of low FIP can be seen directly above the tip of the fatigue crack. In contrast, the highest FIP values are reached in segment 4. Figure 3.5 (b) shows the simulation results at cycle 136 620. At this stage, one dominant fatigue crack has formed in segment 4. As already predictable from Figure 3.5 (a), the fatigue cracks in segments 2, 3, and 5 have not grown much further since they are shielded by the dominant crack. This behavior can also be seen in Figure 3.5 (c) which shows plots of the number of failed elements per segment over the cycle number. With the emergence of the dominant macro fatigue crack in segment 4, the fatigue crack growth in all other segments slows down and stops almost completely in segments 3 and 5.

3.4.2 Configuration with a small lateral temperature gradient

Next, the results of configuration 3.3 (b) are presented. A relatively small lateral temperature gradient is introduced by deactivating the heating beneath only one-half segment. This reduces the total thermal energy introduced by 6.25%. The distribution of the FIP prior to the occurrence of fatigue cracks is depicted in Figure 3.6. The influence of the modified temperature field is visible, in particular when comparing it with Figure 3.4. How this lateral thermal gradient affects the emerging fatigue cracks is presented in Figure 3.7. The first fatigue crack emerges at 105 220 cycles at the hump in segment 4, similar to the standard configuration. Figure 3.7(a) shows how the fatigue cracks have developed after

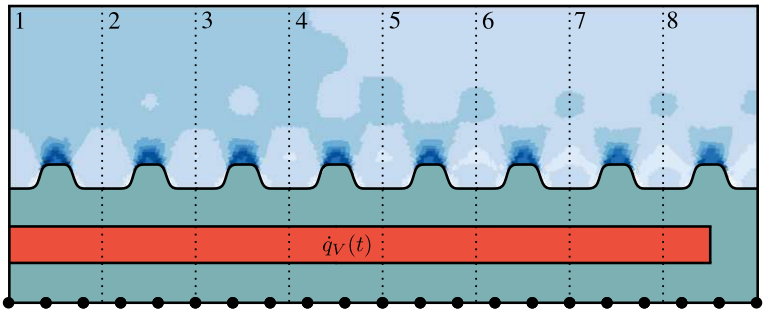

Figure 3.6: Distribution of FIP prior to the occurrence of fatigue cracks. Dark blue values indicate a high FIP, light blue values a low one.

132 350 cycles. The cracks in the segments 1-6 have all reached a relatively similar size, whereas the fatigue cracks in segments 7 and 8 are much smaller. This can also be seen in Figure 3.7 (c), which illustrates that the fatigue cracks in segments 7 and 8 initiate at higher cycle numbers than the fatigue cracks in the other segments.

Figure 3.7 (b) depicts the model at a later stage in the simulation, namely after 165 890 cycles. Again, a dominant fatigue crack has formed in segment 4, shielding the neighboring segments. Interestingly, the fatigue cracks of segments 7 and 8 have reached a length similar then those of the other non-dominant cracks.

It can be summarized, that deactivating the heating beneath one-half segment (i.e. one DMOS cell) influences the fatigue crack formation not enough to drastically change the

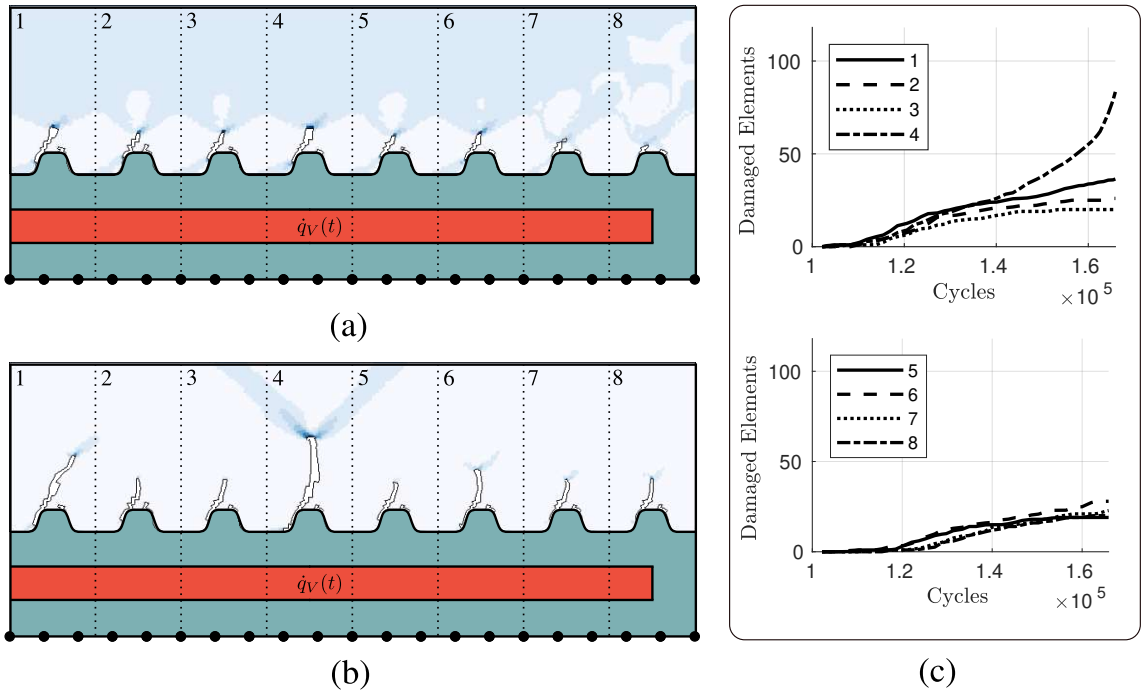

Figure 3.7: Fatigue damage characteristics of eight generic DMOS cell segments with a small lateral temperature gradient induced by deactivating the power layer beneath one-half cell. Figure (a) shows the fatigue macro cracks and FIP values at cycle number 132 350. Dark blue values indicate a high FIP, light blue values a low one. Figure (b) shows fatigue macro cracks and FIP values at cycle number 165 890. In Figure (c) the evolution of the fatigue cracks in the different segments can be seen.

forming crack patterns. Nevertheless, the reduction of the total thermal energy by 6.25% increases the number of cycles needed to reach a similar crack pattern by roughly 25%, when comparing Figures 3.5 (c) and 3.7 (c).

3.4.3 Configuration with a strong lateral temperature gradient

To get a better understanding of the effects of a stronger lateral temperature gradient, the number of segments without heating is increased from a half segment to two segments, see Figure 3.3 (c). This reduces the total amount of thermal energy introduced by 25% with respect to the standard configuration. While in the previously presented configurations the position of the first fully damaged element is largely dependent on the unstructured mesh, in this configuration the thermal differences between the segments become dominant. This leads to the first fatigue crack initiating in segment 1 at cycle number 199 280.

This number is significantly higher as the two previously observed cycle numbers for fatigue crack initiation, and it also takes much longer until the first larger fatigue cracks have formed. In Figure 3.8 (a) the damage state at cycle number 265 820 is presented. While this cycle number is more than double as high as the one of Figure 3.7 (a) very little progression of the fatigue cracks can be observed. The first two segments show small fatigue cracks and also the first elements are completely damaged in segments 3-6. No fatigue crack has formed yet in segment 7 and 8. Even at cycle number 353 120, as depicted in Figure 3.8 (b), no significant fatigue cracks can be seen in these two segments. A dominant crack has emerged in segment 2. This is interesting regarding two aspects. First, it shows that the lateral temperature gradient is now strong enough to force the dominant crack away from the mesh favored position in previously presented simulations. Secondly, it does not form in segment 1 which shows the first fatigue crack and also has the highest temperature. This can be explained by the boundary conditions. The mechanical symmetry boundary conditions at the left border of the first segment imply that also in the imaginative neighboring segment a symmetric crack occurs. Therefore, the crack growth in segment 1 is slowed down because it is shielded by itself through the symmetry assumption.

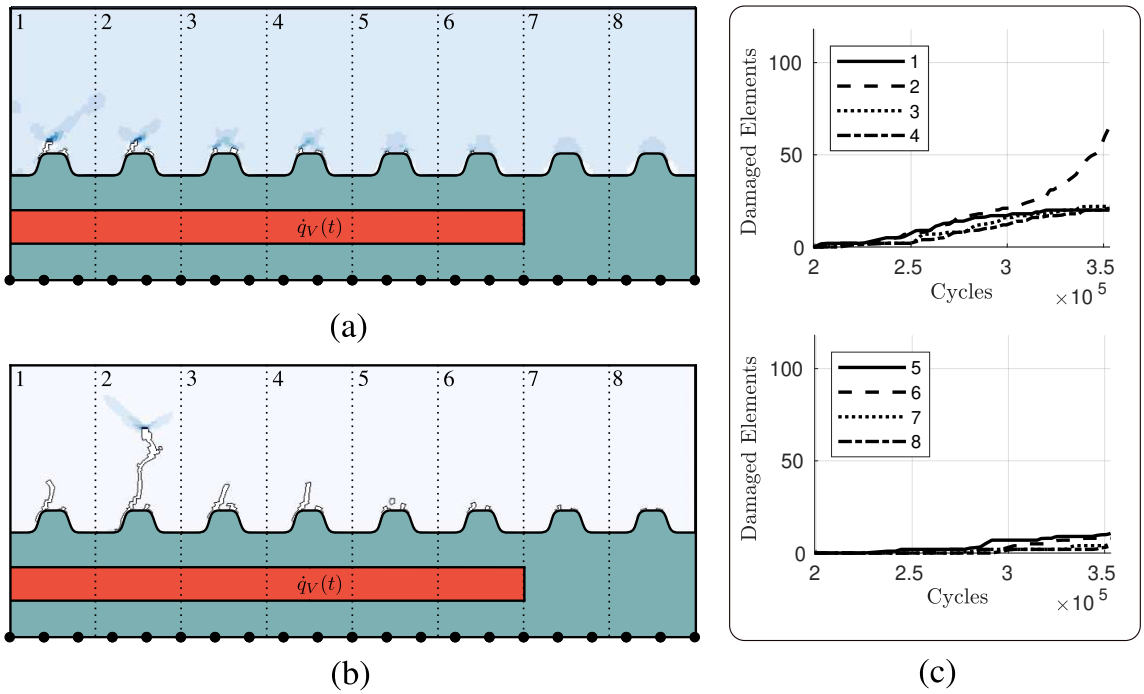

Figure 3.8: Fatigue damage characteristics of eight generic DMOS cell segments with a strong lateral temperature gradient induced by deactivating the power layer beneath two cells. Figure (a) shows the fatigue macro cracks and FIP values at cycle number 265 820. Dark blue values indicate a high FIP, light blue values a low one. Figure (b) shows fatigue macro cracks and FIP values at cycle number 353 120. In Figure (c) the evolution of the fatigue cracks in the different segments can be seen.

The plots in Figure 3.8 (c) illustrate all of the explained effects in more detail. The fatigue crack initiation in segment 1 can be seen as well as the formation of the dominant crack in segment 2 and the minimal crack growth in segments 5-8.

Figure 3.9 illustrates the influence of fatigue cracks on the developing temperature fields. It is clearly visible that the fatigue cracks have a strong influence on the temperature fields. Locally, the crack in segment 2 restricts the thermal flow from the left to the right side, see in Figure 3.9(b). Globally, the evolving fatigue damage seems to have two effects on the overall behavior. The highest temperature occurs later in the cycle and higher overall temperatures are reached.

3.4.4 Configuration with regions of faster damage onset

The last results presented in this work illustrate a different aspect of propagating fatigue cracks. The main question addressed here is how faster growing cracks affect their surroundings. Therefore, the fatigue damage onset in the two center segments is sped up by 20%. Otherwise the model is equivalent to the standard configuration in Figure 3.3 (a). As a result, the first fatigue cracks appear simultaneously at cycle number 70 654 in segments 4 and 5. In Figure 3.10 (a) it can be seen that at cycle 97 278 the fatigue cracks in the two center segments have grown substantially, whereas in the remaining segments little to no fatigue cracks have formed. The faster crack growth in the two center segments continues, with both growing at a similar pace without interfering too much with each other. The crack pattern after 108 540 cycles is depicted in Figure 3.10 (b). At this cycle number, the fatigue crack in segment 4 has grown into segment 5. The lower FIP values for the crack originating in segment 5 indicate that it is about to stop.

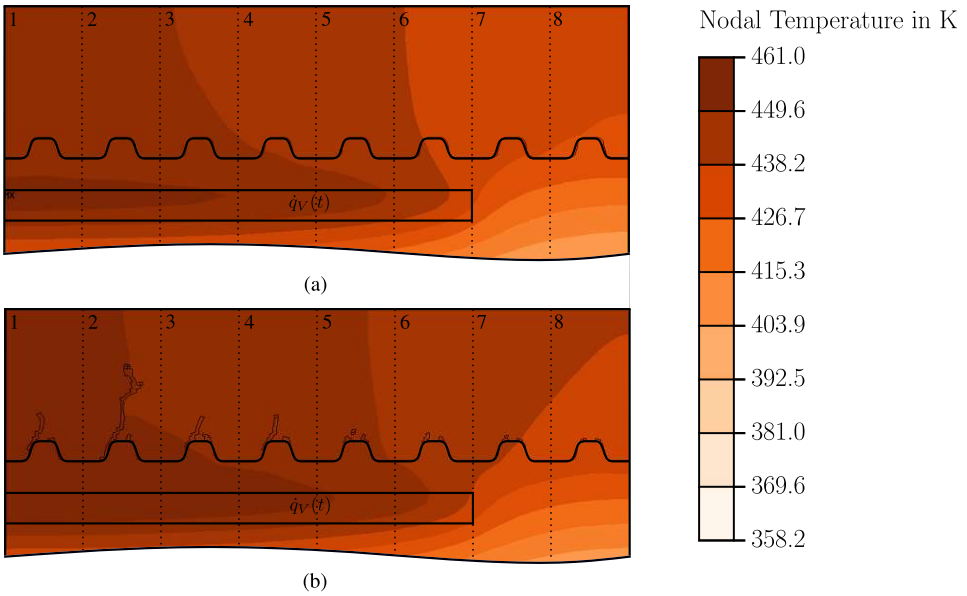

Figure 3.9: Temperature plots of the arrangement with a strong lateral temperature gradient. The temperature field of the undamaged model at the time of the maximum temperature ($t = 0.136\,\mathrm{ms}$), is depicted in (a). Figure (b) shows the temperature field of the model after 353 120 cycles at the time of the maximum temperature ($t = 0.144\,\mathrm{ms}$).

The influence of dominant cracks on their surrounding is illustrated in Figure 3.11 The black and the grey solid lines give the total number of failed elements over cycle number of segment 1 and 8 of the standard configuration (Section 3.4.1) and the current simulation, respectively. Both segments are far away from the dominant cracks. It can be seen that the fatigue cracks evolve similarly for both configurations. Contrary to this result, the dashed lines, which depict the overall number of failed elements in segments 3 and 6, the segments in the vicinity of the dominant cracks, differ strongly for both simulations. Looking back at Figure 3.5 (a), it is evident that at the given maximum cycle number of Plot 3.11, no dominant fatigue crack has formed and therefore no distinct shielding has taken place. As a result, the two black lines are almost identical. However, the forced fatigue cracks

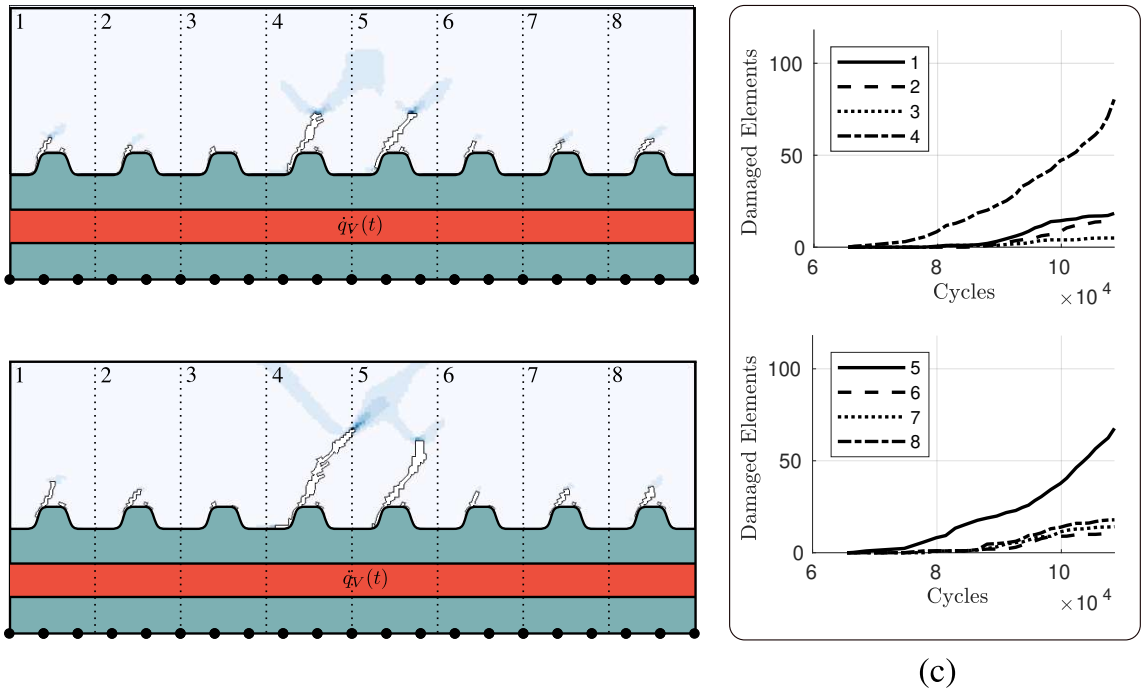

Figure 3.10: Fatigue damage characteristics of eight generic DMOS cell segments with accelerated fatigue damage onset in segments 4 and 5. Figure (a) shows the fatigue macro cracks and FIP values at cycle number 97 278. Dark blue values indicate a high FIP, light blue values a low one. Figure (b) shows fatigue macro cracks and FIP values at cycle number 108 540. In Figure (c) it can be seen that the evolution of the fatigue cracks in the different segments.

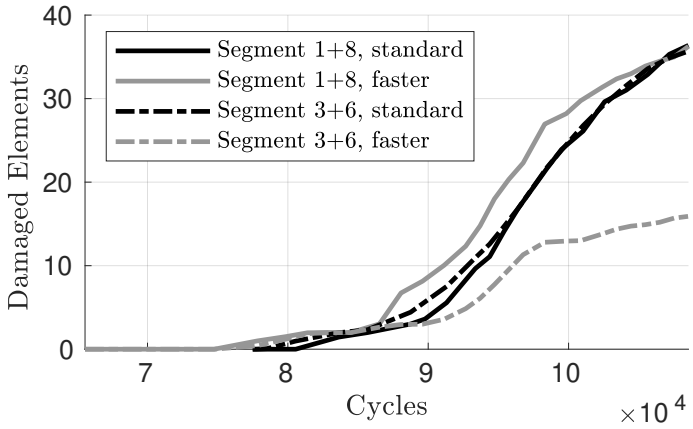

Figure 3.11: FEM models of DMOS cell-like features to study the influence of lateral temperature differences (a-c) and locally accelerated fatigue damage onset (d) on the growth of fatigue cracks.

in segment 4 and 5 (Figure 3.10 (b)), have a strong shielding effect on the neighboring segments and reduces the fatigue crack growth significantly in these segments.

3.5 Summary

The bulk fatigue framework proposed in [93, 94] is extended towards the application of sequentially coupled transient thermo-mechanical loading conditions.

Different configurations of eight DMOS cell-like structures are simulated utilizing a bulk fatigue framework under transient thermo-mechanical loading conditions. In such arrangements, the influence of non-uniform temperature fields on the fatigue damage initiation and on the fatigue crack propagation is studied.

A configuration that has no thermal difference between the individual cells is used as the reference solution. In this case, numerical perturbations introduced by the unstructured mesh determine the position where a dominant crack forms. Small lateral thermal gradients do not influence the fatigue behavior enough to change the position of the dominant crack, however, they significantly decrease the crack growth rate. For a substantially stronger lateral temperature gradient the dominant crack emerges in regions of higher temperature.

Furthermore, it is demonstrated that dominant fatigue cracks lead to shielding effects, i.e. significantly slow down the fatigue crack growth in their vicinity.

Chapter 4

Prediction of Surface Damage

4.1 Introduction

This chapter focuses on the formation of fatigue cracks visible on the surface of Cu metallization layers deposited on top of the active device area and the Si substrate. The goal is to assess the material parameters related to TMF damage in Cu metallization layers by using thermo-mechanically cycled test chips [66, 67] in conjunction with the fatigue damage framework presented in Chapter 2. First, the capability of a FS FIP to qualitatively predict the characteristic damage "distribution" on the surface of the test chips is illustrated. In a second step, a strategy is developed that enables a quantitative comparison of experimentally and numerically obtained results. This quantitative comparison is used to calibrate the parameters of a Coffin-Manson fatigue law to achieve an optimal fit of the predicted damage to the experimental results. Finally, the predictive capabilities of the calibrated framework are presented employing test chips subjected to other thermo-mechanical loading conditions than the test chips used for calibration. This chapter is based on Hoffmann et al. 2022 [34].

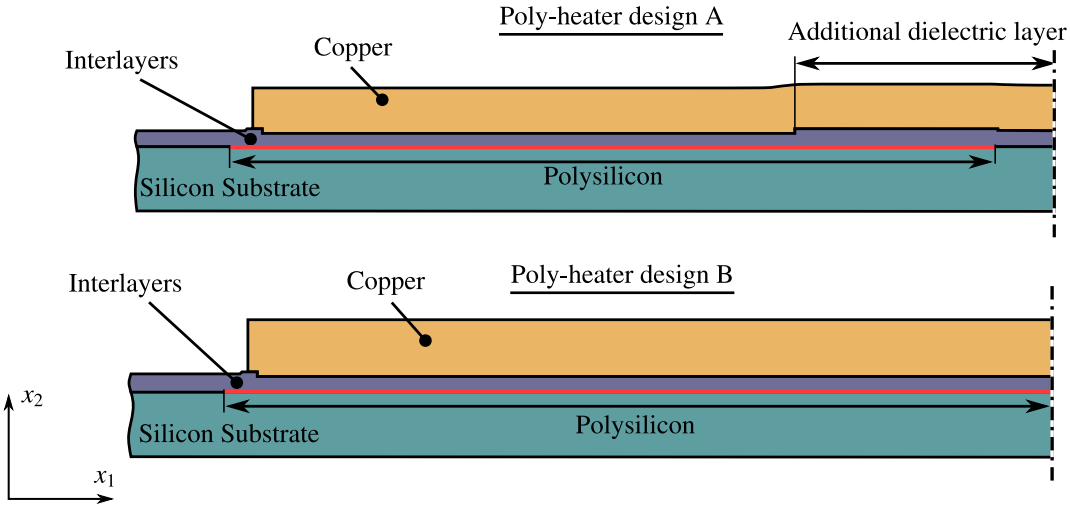

Figure 4.1: Schematic half cross-section of the two DUT layouts A and B, respectively.

4.2 Experimental analysis

In this section, the devices under test (DUT) and the experimental setup are presented. The experiments have been carried out by Sebastian Moser [66, 67] at the Kompetenzzentrum Automobil- und Industrieelektronik GmbH (KAI) and the damage detection algorithm discussed in Section 4.4 has been implemented by Corinna Kofler also at KAI.

4.2.1 Devices under test

The DUTs used for this work are microelectronic test chips with active heating specifically designed for TMF experiments. Their heating system is based on Joule heating of the integrated high-ohmic polycrystalline silicon (polysilicon) layer by applying electrical power. Due to the polysilicon heating layer, the whole devices are referred to as poly-heaters. Two different poly-heater layouts (A and B) are used for this work. Figure 4.1 shows schematic half cross-sections of both designs. The poly-heaters consist of a Si substrate with thickness $h_{\mathrm{Si}} = 120\,\mu\mathrm{m}$, a $20\,\mu\mathrm{m}$ thick Cu metallization layer with lateral dimensions of $700\,\mu\mathrm{m} \times 490\,\mu\mathrm{m}$, and a grain size significantly smaller than these dimensions, and various comparatively thin interlayers responsible for the functionality. One of those layers is the electrically isolated polysilicon layer ($h_{\mathrm{p}} = 300\,\mathrm{nm}$), which is responsible for active heating.

In the lateral direction, the size of the polysilicon varies between the two poly-heater layouts. In layout B the polysilicon is spread beneath the whole Cu layer with a lateral length of 720 µm. In contrast, in layout A, the polysilicon has a gap of 50 µm in the middle of the device (see Figure 4.1), which causes inhomogeneous heating across the poly-heater. Also part of the interlayers is a likewise electrically isolated structured Aluminum (Al) layer which is utilized as resistance temperature sensor in both poly-heater layouts.

Apart from the gap of the polysilicon layer, there is a second major design feature, differentiating layout A from layout B. In layout A, additional dielectric layers impede the heat flow between the polysilicon layer and the Cu metallization layer at the central 225 µm (see Figure 4.1).

As the Cu is deposited with a constant thickness, the approximate 1.5 µm high step of the additional dielectric layers translates to the Cu surface, which can be seen in Figure 4.1 true to scale. A second smaller step occurs at the end of the polysilicon layer near the center of the poly-heater. The shape of these surface irregularities is determined from a surface analysis of the DUT using confocal microscopy.

4.2.2 Experimental procedure

In order to thermo-mechanically load the DUTs by application of repetitive heat pulses the experimental setup described in [66] is used. For both poly-heater layouts, two DUTs are experimentally analyzed. The experimental analyses of the DUTs is done in a vacuum environment ($\sim 10^{-5}$ mbar). First, the DUTs are heated to a stable base temperature $T_B = 100\,°C$ by applying a DC voltage to their polysilicon heating layer. Subsequently, a total number of 5000 pulses, characterized by a temperature rise from T_B to $T_P = 450\,°C$ in 200 µs, are applied. The number of 5000 pulses is chosen because preliminary experiments have shown that at this stage the crack growth on the surface is saturated. Between each pulse, a pause of 1 s is introduced to give the DUT time to cool down to T_B. Key data of the power pulses used in the experiments are presented in Figure 4.2. Figure 4.2a depicts the voltage applied to the polysilicon layer and Figure 4.2b the corresponding dissipated power.

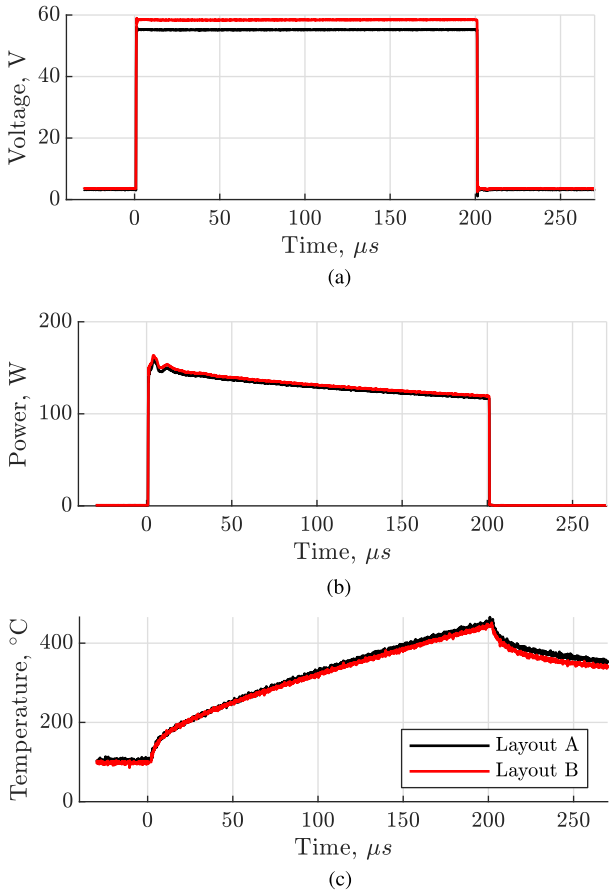

Figure 4.2: Characterization of the pulses applied to the DUT: (a) voltage applied to the polysilicon, (b) dissipated power, and (c) resulting temperature profile.

The DC voltage for base temperature heating and the pulse voltage are both set in a way that the above-mentioned target temperatures are achieved regardless of the layout of the respective DUT, as shown in Figure 4.2c. The base temperature heating is characterized by DC voltages of 3.2 V and 3.4 V (corresponding to powers of 0.57 W and 0.59 W), whereas the pulses are characterized by rectangular shaped voltages of 55.2 V and 58.3 V for the DUT layouts A and B, respectively. Although a constant voltage is applied to the polysilicon during the pulses, the resulting dissipated power is characterized by a declining profile (see Figure 4.2b). This is explained by the fact that during the pulses the temperature and correspondingly also the temperature-dependent resistance of the polysilicon increases by a significant amount, which in turn results in a power dissipation that is decreasing over time.

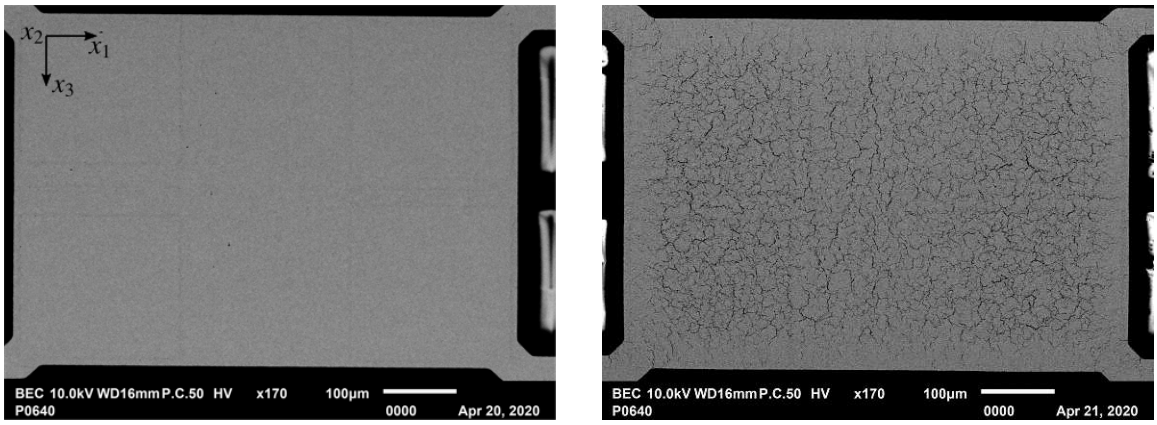

(a) 0 heat pulses **(b)** 5000 heat pulses

Figure 4.3: SEM image of the Cu metallization of a DUT of layout A before (a) and after (b) the experiment consisting of an application of 5000 heat pulses ($T_\mathrm{B} = 100\,^\circ\mathrm{C} \rightarrow T_\mathrm{P} = 450\,^\circ\mathrm{C} \rightarrow T_\mathrm{B} = 100\,^\circ\mathrm{C}$) .

4.2.3 Damage detection by means of surface imagery

SEM images are acquired before and after the individual experiments with a resolution of 0.2941 µm/pixel. Representatively, Figure 4.3 depicts one of the two DUTs of layout A at the pristine, undamaged state and after 5000 cycles, respectively. It clearly shows that the repetitive pulsing is driving degradation processes in the Cu metallization, leading to the formation of visible surface microcrack patterns. In the outmost $\sim 30\,\mu\mathrm{m}$ of the Cu plate significantly less surface microcracks are observed (cf. Figure 4.3b). This observation is attributed to edge effects, which can be explained by shear lag theory. Confining to the central part of the Cu plate, a lateral gradient in the amount of visible microcracks is expected as a result of the layout of the type A DUT see Section 4.2.1. However, examining Figure 4.3b by eye does not allow making a conclusive statement about the lateral distribution of the degradation. For this purpose, a quantitative approach for characterizing the degree of damage across the metallization layer based on SEM images has been developed at KAI by Corrina Kofler.

This approach consists of a series of steps that are conducted in a consistent manner for all of the experimental results. First, the images are cropped as is shown in the left image

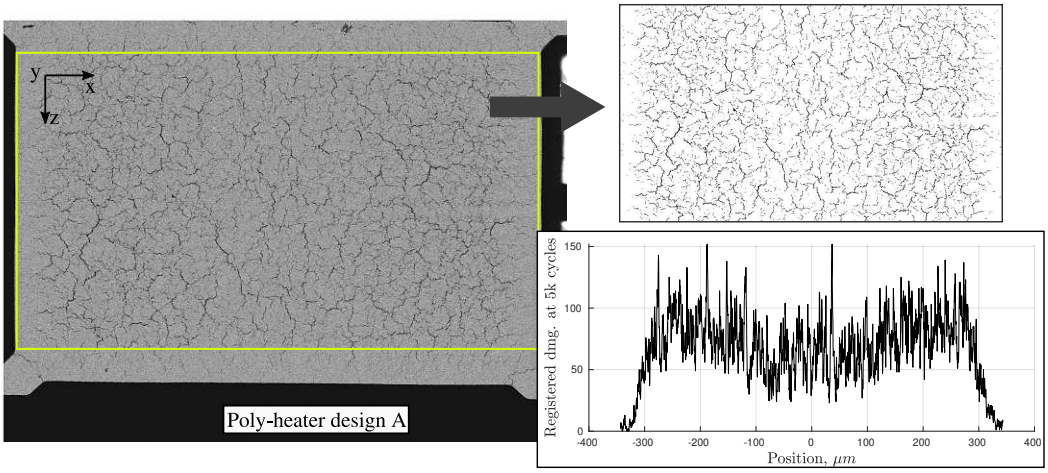

Figure 4.4: The left side of this figure shows a SEM image of the poly-heater after 5000 cycles, with the frame marking the cut-off area for further evaluation. At the upper right a binarized image is shown and at the bottom right the corresponding pattern of the experimental fatigue damage across the x_1-direction is presented.

of Figure 4.4. This step is done using the open source image software ImageJ (Public Domain [84]). All subsequent steps are conducted using MATLAB R2020b (MathWorks Inc., Natick, MA, USA). The cropped images are binarized using a global threshold obtained by Otsu's method. Within the binarized images, all pixels that are above the threshold are attributed to microcracks. This allows to quantify the amount of damage over the x-axis (see lower right corner of Figure 4.4). Here, for each column of the binarized image, all pixels attributed to microcracks are summed up and plotted against the x-position of the column. Presenting the data in this way makes it less dependent on individual surface cracks and, consequently, on local features of the microstructure such as grain boundaries. Instead, the data represents a quantitative description of the damage distribution introduced by lateral temperature gradients. These pixel sums are subsequently denoted as experimental fatigue damage.

4.3 Numerical prediction of fatigue damage

Both poly-heater layouts are simulated numerically with the FEM software ANSYS Mechanical APDL 19.2 (ANSYS Inc., Canonsburg, PA,USA).

To keep the simulation effort within reasonable limits, the three-dimensional (3D) poly-heater structures are simplified to 2D models of one half of the poly-heaters. This simplification is justified because even in 3D simulations, plane strain conditions would be present in large areas of the poly-heaters, due to their geometry and the applied loading conditions. This is in accordance with the experimental data, where the registered damage is also summed up over the depth and analyzed independently of the z-direction. The geometry of the models is shown in the cross-sections in Figure 4.1. The depicted Cu surface topology irregularities are included in the simulations. Small device features, such as temperature sensors that do not extend over the whole lateral depth (x_3-direction) of the DUTs are disregarded since their influence is expected to be negligible. The whole geometry is meshed using isoparametric, four node, linear interpolated, and fully integrated elements. An element edge length of around 0.33 µm is used for the Cu metallization layer and the interlayers, while the Si substrate is meshed much coarser. The employed constitutive laws and material properties are given in Appendix A. It should be noted that the constitutive law for the copper metallization describes the homogenized (effective) response of polycrystalline copper. The influence of microstructural descriptors such as the grain size is reflected to some extent in the material parameters.

Based on the approach presented in Chapter 3 the numerical analysis is divided into multiple parts as depicted in Figure 4.5. For analyzing the thermo-mechanical response due to a power pulse, a transient thermo-mechanical loading procedure is used. A weak coupling between the thermal fields and the mechanical fields is applied. The transient thermal analysis is conducted based on the material properties, the geometry, the given power pulse (see Section 4.2), and the boundary conditions. This analysis results in the nodal temperatures at all time increments used to resolve the power pulse and the cooling phase. Subsequently, these temperature fields are used as a temperature boundary condition for the mechanical

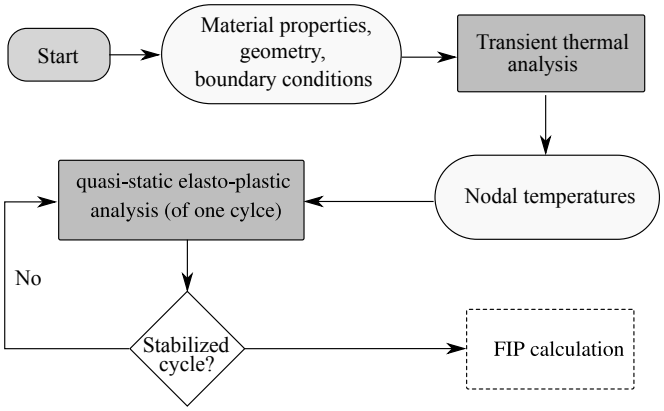

Figure 4.5: Simplified representation of the steps necessary to obtain the FIP.

simulation. The elasto-plastic mechanical analysis is conducted quasi-statically and under plane strain assumptions for each time increment given by the transient thermal analysis for one pulse cycle. For the fatigue simulation, it is necessary to repeat the mechanical analysis until a stabilized plastic cycle is found. From the latter the FIP is calculated and compared to the experimental results. In contrast to Chapter 3 the simulation is ended after the first FIP calculation as the damage evolution is not considered in this chapter.

4.3.1 Transient thermal analysis

The thermal boundary conditions are chosen such that the simulation and modeling effort are kept within reasonable limits, while still capturing the important aspects of the experiments. Heat is introduced into the system by the volumetric heat generation rate, $\dot{q}_V(t)$, in the active polysilicon layer. The heating rate $\dot{q}_V(t)$ is based on the available electrical loading data of the experiments. It is defined by

$$\dot{q}(t) = \frac{P(t)_{\mathrm{Poly}}}{V_{\mathrm{Poly}}} \tag{4.1}$$

with $P(t)_{\mathrm{Poly}}$ being the time-dependent power introduced into the polysilicon and V_{Poly} the volume of the polysilicon, as explained in Section 4.2.2. One thermal load cycle starts at $\mathrm{t} = 0\,\mu\mathrm{s}$, captures the full loading pulse until $\mathrm{t} = 200\,\mu\mathrm{s}$, and also includes the subsequent

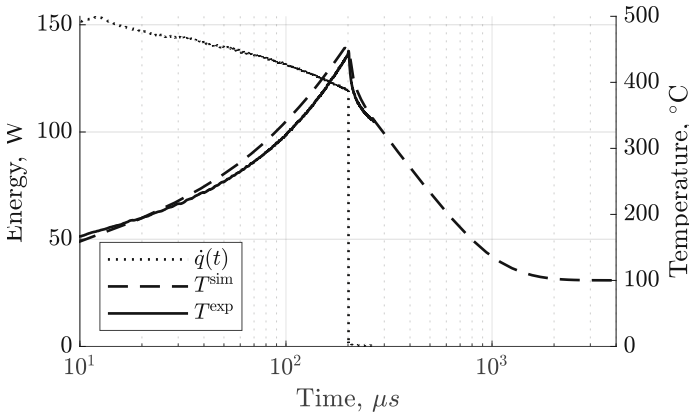

Figure 4.6: The pulse energy introduced in the polysilicon layer together with the experimental temperature response T^{exp} measured at the temperature sensor and the simulated temperature T^{sim} at the approximate position of the temperature sensor.

cooling-off phase until t = 1 s, when a steady state temperature field is reached. Since the test chamber is in a vacuum environment, there is no heat convection into the surrounding of the DUT. Heat radiation is neglected, since its role is expected to be insignificant. Consequently, the thermal energy introduced by the polysilicon layer is only dissipated by the mounting of the DUT in the sense of a heat sink. In order to model this heat sink, temperature boundary conditions are applied at the bottom nodes of the silicon substrate using a fixed temperature $T_{\text{bottom}} = 97.5\,°\text{C}$. The temperature T_{bottom} is determined in a preliminary analysis so that the simulated base temperature at the position of the temperature sensor is in good agreement with the experimentally measured base temperature of 100 °C. With $T_{\text{bottom}} = 97.5\,°\text{C}$ the whole temperature response measured at the temperature sensor can be well predicted by the simulations, as exemplified for the type A DUT in Figure 4.6. The simulated maximum temperature is with 452 °C only insignificantly larger than the 450 °C measured in the experiments. For all simulations as well as for all experiments the maximum temperature occurs at the end of the power pulse at $t = 200\,\mu\text{s}$.

Figure 4.7 shows the simulated nodal temperature field of the layout A poly-heater model at the end of the power pulse. The lateral thermal gradient, which is caused by the non-continuous polysilicon layer and the additional dielectric layers, is clearly visible.

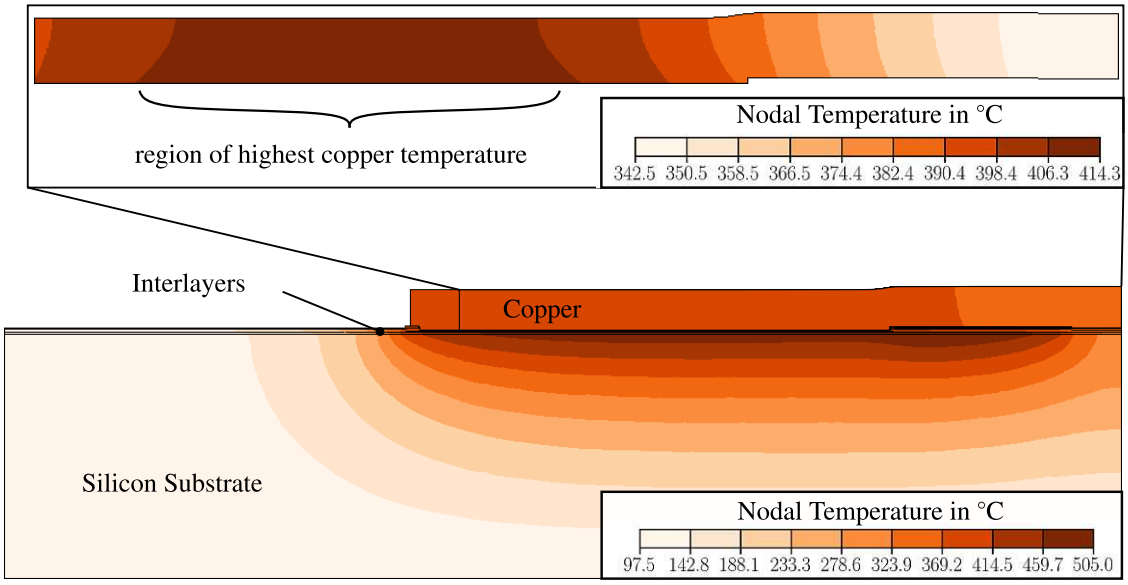

Figure 4.7: Nodal temperature field in a part of the Cu metallization layer and in the whole model of the poly-heater at the timestep with the maximum temperature ($t = 200\,\mu s$).

4.3.2 Mechanical analysis and calculation of the FIP

The mechanical boundary conditions consist of symmetry boundary conditions at the right side and constrained displacements in the y-direction at the bottom nodes. This is a simplification, but since the substrate is relatively thick compared to the rest of the poly-heater, the influence on the fatigue calculations is expected to be negligible.

The model is loaded incrementally with the previously determined nodal temperatures. The nodal temperatures introduce mechanical stresses and strains due to the different coefficients of thermal expansion of the individual materials. Due to these stresses plastic deformation occurs in the Cu metallization layer.

The mechanical analysis is repeated until a stabilized plastic cycle is found, i.e. the change in dissipated inelastic energy in the Cu metallization from one cycle to the next is less than 1% of the dissipated inelastic energy, see Equation 2.13. Subsequently, fatigue damage can be predicted based on Chapter 2. In contrast to [93] and Chapter 3, the goal is not to model the propagation of individual fatigue cracks. Instead, the predictive capabilities of

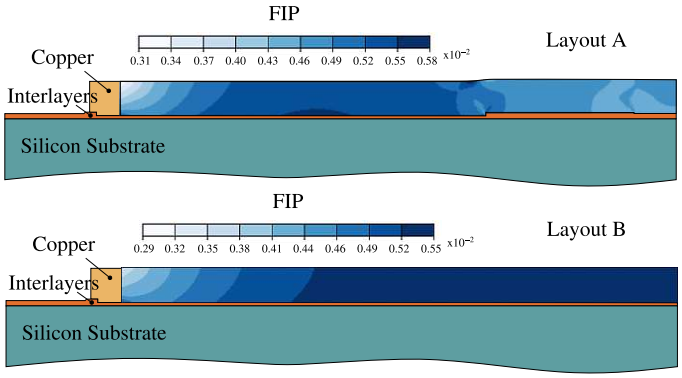

Figure 4.8: Picture showing the FIP normalized to the maximum in the Cu metallization layer.

the FS fatigue initiation criterion in the context of spatially varying thermo-mechanical loading conditions are studied and the results are compared with those of corresponding experiments.

With Equation (2.5) the FIP is calculated for every element in the Cu metallization layer for layout A (top) and layout B (Bottom). Figure 4.8 shows the FIP normalized to its maximum value within the largest part of the metallization layer. In this figure two major aspects of the FIP distribution are visible. On the one hand, the overall distribution of the FIP is driven by the temperature distribution (compare Figure 4.7). High maximum temperatures lead to high FIP values. And on the other hand, even relatively small and inconspicuous geometric features, such as the ramp at the beginning of the additional dielectric layers seem to have a large impact on the local FIP distribution. As a result of both aspects, the FIP distribution in layout A varies drastically in lateral direction, while layout B it is defined by relatively constant values in the middle with a decrease of the FIP towards the edge. In the subsequent comparison with the experimental data, only the FIP values of the surface elements are used.

4.4 Parameter calibration and predictive capabilities

4.4.1 Qualitative comparison between experimental and numerical results

As mentioned in Section 4.2 two experiments for each poly-heater layout are conducted. The damage detected after 5000 Cycles is summarized in Figure 4.9. Due to the symmetric layout of the poly-heaters, both halves (Figure 4.1) of each individual layout show a similar fatigue behavior. The fluctuations in the registered damage values of the individual halves are a consequence of local features of the particular microstructures under observation. In order to highlight the main characteristics of the experimentally observed fatigue damage of the individual layouts, a mean value is calculated over the available four halves, as is shown in Figure 4.9(a) and (b) for both layouts, respectively. This reduces the influence of individual cracks and allows a better comparison of simulations and experiments. These mean values show distinct patterns for both layouts. For layout A (Figure 4.9(a)) this pattern is characterized by a sharp rise of fatigue damage from the edge of the poly-heater ($-350\,\mu m$) to a maximum at around $-250\,\mu m$. Approximately at the beginning of the additional dielectric layers ($\approx -120\,\mu m$) there is a sharp increase and subsequent decrease in fatigue damage, followed by a region with less damage. In the middle of the poly-heater there is another region of higher damage. In case of layout B (Figure 4.9(b)), the pattern is characterized by a steep incline from the edge of the poly-heater to a plateau-like experimental fatigue damage towards the center of the DUT. This is the consequence of a large region with equally high maximum temperatures within layout B. For both device types, moving mean values (boxcar filter) over neighboring 250 pixel columns in x-direction are computed. The results are shown in Figure 4.9(c) and Figure 4.9(d), respectively.

The FIP values of the surface elements obtained by the FEM simulations are presented in Figure 4.10.

While the FIP value is just an indication where fatigue damage is more likely to form and the plots are not directly comparable to the experimental ones in this form, a qualitative

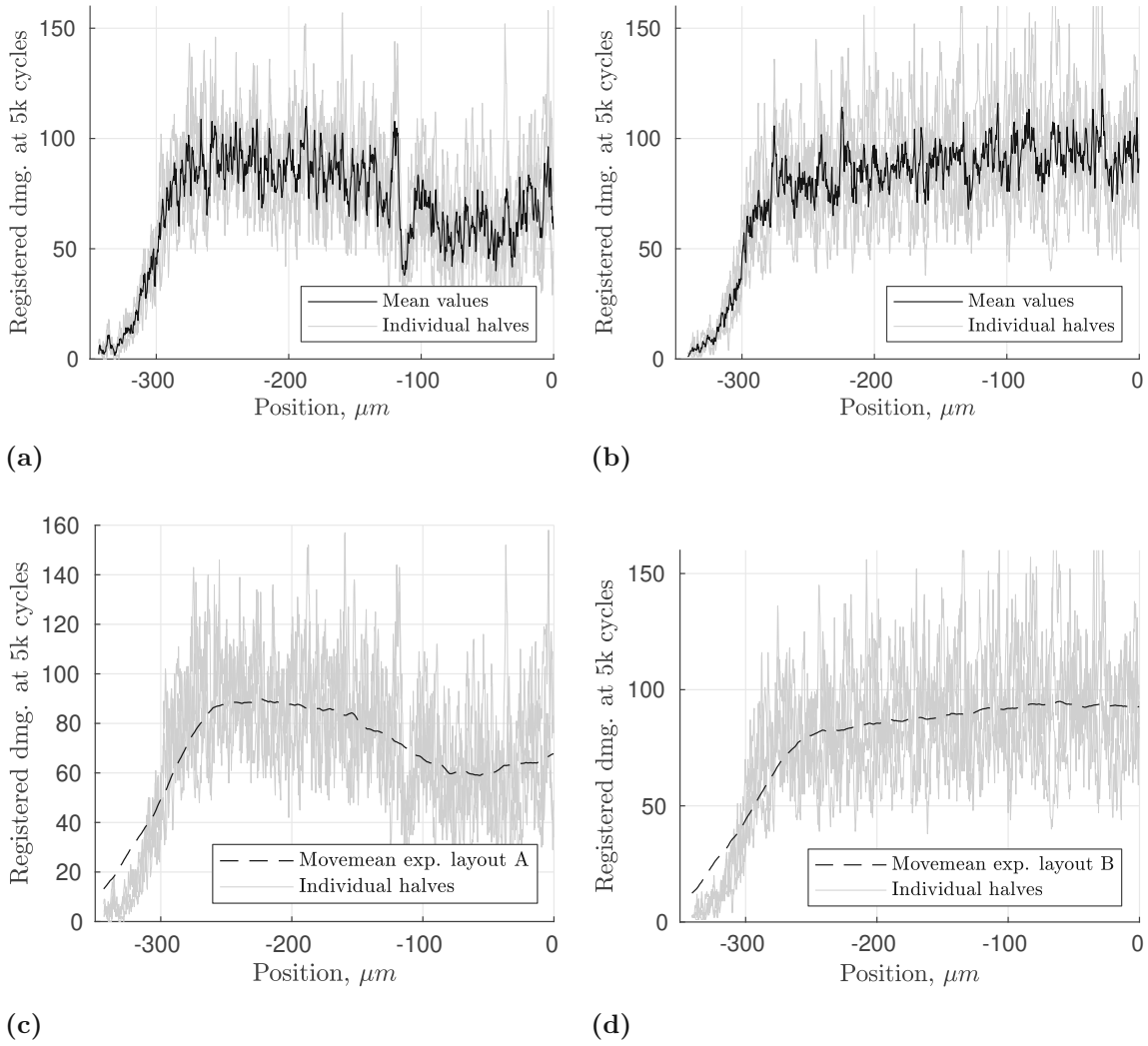

Figure 4.9: Combination of the damage patters of the four individual halves available for the layout A(a) and the layout B(b), respectively. Figure (c) and Figure (d) show the moving mean values for the poly-heater layouts A and B, respectively.

agreement between Figures 4.9 and 4.10 can already be seen. This is particularly true for layout A.

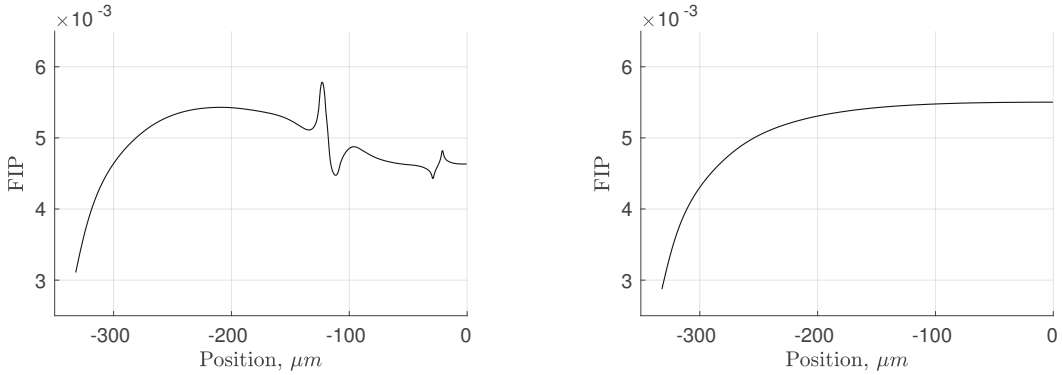

(a) **(b)**

Figure 4.10: Simulated FIP result for layout A(a) and layout B(b), respectively for the elements at the surface.

4.4.2 Parameter calibration of the Coffin-Manson law

With the FIP presented in Equation 2.4 and the FS fatigue criterion written in the LCF formulation as

$$\underbrace{\left\{\frac{\Delta\gamma}{2}\left(1+\varkappa\frac{\sigma_n^{\max}}{\sigma_{\mathrm{Y}}}\right)\right\}_{\max}}_{\mathrm{FIP}} = \gamma_{\mathrm{f}}'(2N_{\mathrm{N}})^{c_\gamma} \tag{4.2}$$

it is now possible to calibrate γ_{f}' and c_γ based on the available experimental results. Usually, these parameters are calibrated using standardized experiments that have distinct failure criteria and therefore also distinct failure cycle numbers N_{N} for given load cases. For TMF there exists no established failure criterion, which makes the application of a common calibration process impossible.

However, the experimental result of layout A can be considered as a correlation between different local loading conditions and a probability of visible microcracks. This means that instead of different separate experiments with distinct failure cycle numbers, the spatially varying experimental fatigue damage of layout A can be used for calibration.

To allow quantitative comparison, the result of the experiments are normalized as

$$D_{\text{surf}}^{\text{exp}}(x) = \frac{d_{\text{surf}}^{\text{exp}}(x)}{\max(\text{movemean}(d_{\text{surf}}^{\text{exp}}(x)))} \tag{4.3}$$

with $d_{\text{surf}}^{\text{exp}}(x)$ being the mean of the experimental damage over the four available halves as presented in Figure 4.9 (a,b), movemean() is the moving mean value over the neighboring 250 pixels, and $D_{\text{surf}}^{\text{exp}}(x)$ is the normalized experimental damage. A moving mean value is necessary since a normalization based on one of the peak values is not meaningful, whereas the value of 250 pixels has the desired effect without smoothing the overall result too much. The position where the maximum of the moving mean values occurs is subsequently called $\hat{x}$. The result of the simulation can be presented in a similar way as the normalized simulation damage value

$$D_{\text{surf}}^{\text{sim}}(x) = \frac{\min(\text{movemean}(N_{\text{N}}))}{N_{\text{N}}} = \frac{\min(\text{movemean}(\text{FIP}(x)^{(1/c_\gamma)}))}{\text{FIP}(x)^{(1/c_\gamma)}} \tag{4.4}$$

derived from Equation (4.2). The minimum value is used for the normalization, since the lowest cycle number is equivalent to the highest damage probability. Again, a moving mean value is used to circumvent a normalization against local peak values. The two normalized damage values $D_{\text{surf}}^{\text{sim}}$ and $D_{\text{surf}}^{\text{exp}}$ can be used in the next step to calibrate the fatigue strength exponent, c_γ, of the Coffin-Manson relation based on the distinct damage pattern of layout A.

While the fatigue strength coefficient γ_{f}' has no influence on $D_{\text{surf}}^{\text{sim}}$, c_γ influences the shape of $D_{\text{surf}}^{\text{sim}}$. This influence is presented in Figure 4.11(a). The normalized simulation damage value is computed for various values of c_γ which are in the range of values reported in the literature. The Mean Squared Error (MSE)

$$g = \frac{1}{n}\sum_{i=1}^{n}(D_{\text{surf}}^{\text{exp}}(x_i) - D_{\text{surf}}^{\text{sim}}(x_i, c_\gamma))^2 \tag{4.5}$$

is used to find the value of c_γ for which $D_{\text{surf}}^{\text{sim}}$ gives the best fit to the experimental results, where x_i denotes the positions of the experimental data points. The relation between the

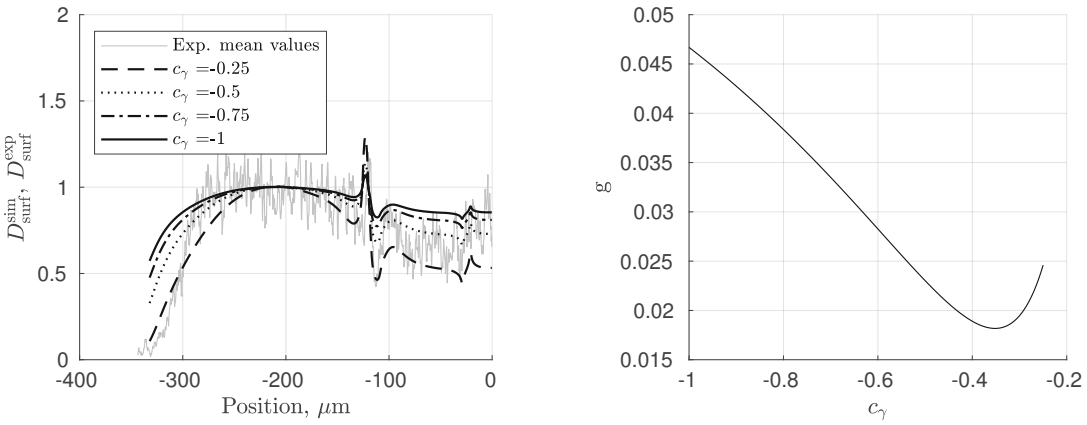

(a) **(b)**

Figure 4.11: Influence of the c_γ parameter on the shape of the normalized simulation damage value D^{sim} (a) and the relation between the error estimate g and the fatigue strength exponent c_γ (b).

error estimate g and the fatigue strength exponent c_γ is presented in Figure 4.11 (b). It can be seen that the smallest mean squared error is achieved with $c^*_\gamma = -0.352$, which is therefore accepted as calibrated value of c_γ.

A comparison between the simulated damage value $D^{\text{sim}}_{\text{surf}}$ using c^*_γ and the experimental damage value $D^{\text{exp}}_{\text{surf}}$ is presented in Figure 4.12 for layout A. This figure also includes the normalized temperature of the surface elements at the end of the power pulse. The shape of the experimental and the simulated curve shows a steep increase from the edge of the poly-heater until a plateau-like damage level is reached at around $-280\,\mu$m. The reason for the steep increase are the edge effects explained by the aforementioned shear lag theory. The plateau is the region where these edge effects have abated and the highest Cu temperatures occur.

With a decrease in temperature, the damage value also starts decreasing at around $-200\,\mu$m until a striking peak of damage followed by a minimum occurs. The peak as well as the minimum can be seen in the simulation as well as in the experimental results. These peaks and minima occur in this form in the four half poly-heater parts at almost the same position

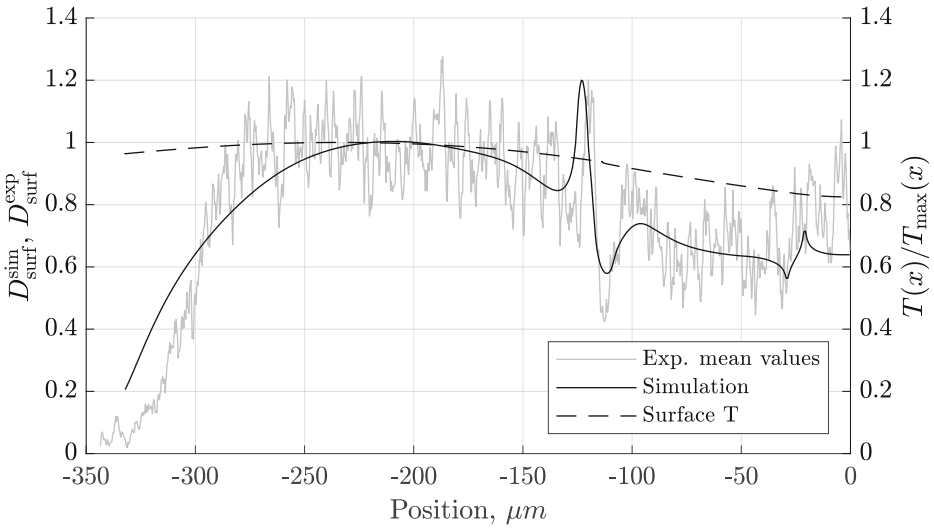

Figure 4.12: Comparison between the experimental results of layout A, the corresponding calibrated fatigue simulation, and the surface temperature at the end of the heating pulse.

(refer Figure to 4.9 (a)), therefore an accumulation by chance is ruled out. In accompanying simulations, the Cu surface is assumed as flat without distinct surface features. The general form with the two plateaus is predicted, but the distinct peaks and minima can not be captured. Therefore, they can be considered as a consequence of the topology of the Cu surface.

The concave part of the small step shown in Figure 4.1 increases the experimentally detected and numerically predicted surface damage, whereas the convex part reduces the formation of cracks in its direct vicinity. Also, the local maximum close to the middle of the poly-heater can be explained by the surface topology. As mentioned in Section 4.2.1 there is a second, even smaller change in Cu height, caused by the underlying end of the polysilicon layer at this position. Even though this step is around 300 nm it still causes a perturbation effect strong enough to be seen in the experiments as well as in the simulation.

The parameter γ_{f}^{*} can now be calibrated by evaluating Equation (4.2) at position $\hat{x}$ of layout A with the experimental cycle number $N = 5000$

$$\gamma_{\mathrm{f}}^{*} = \frac{\mathrm{FIP}(\hat{x})}{(2 \cdot 5000)^{c_{\gamma}^{*}}} \tag{4.6}$$

leading to a calibrated fatigue strength coefficient $\gamma_{\mathrm{f}}^{*} = 0.139$. This means that both Coffin-Manson law parameters are calibrated such that $D_{\mathrm{surf}}^{\mathrm{sim}}(\hat{x}) = D_{\mathrm{surf}}^{\mathrm{exp}}(\hat{x})$ for $N_{\mathrm{N}} = 5000$ for the type A DUT. It has to be kept in mind, that $\hat{x}$ is not the position of the maximum damage caused by the topological feature, but the one corresponding to the maximum of the moving mean. Furthermore, it should be noted that the calibration is done for copper with specific microstructural descriptors. For copper with different microstructural descriptors, different values for γ_{f}^{*} and c_{γ}^{*} may apply.

4.4.3 Predictive capabilities

Using the two calibrated fatigue parameters, γ_{f}^{*} and c_{γ}^{*}, together with the FIP values for layout B as shown in Figure 4.10 (b) the number of cycles $N_{\mathrm{N,B}}(x)$ required until the same experimental fatigue damage is reached as measured at position $\hat{x}$ after 5000 cycles in layout can be predicted.

Subsequently, the normalized simulation damage value is calculated according to Equation (4.4) as

$$D_{\mathrm{surf,B}}^{\mathrm{sim}}(x) = 5000/N_{\mathrm{N,B}}(x) \quad . \tag{4.7}$$

The experimental fatigue damage values of layout B are normalized similarly to Equation (4.3) using the known damage state at $\hat{x}$ of layout A as

$$D_{\mathrm{surf,B}}^{\mathrm{exp}} = d_{\mathrm{surf,B}}^{\mathrm{exp}}/\mathrm{movemean}(d_{\mathrm{surf,A}}^{\mathrm{exp}}(x))|_{x=\hat{x}} \quad . \tag{4.8}$$

A comparison between experimental and simulated results is given in Figure 4.13, also

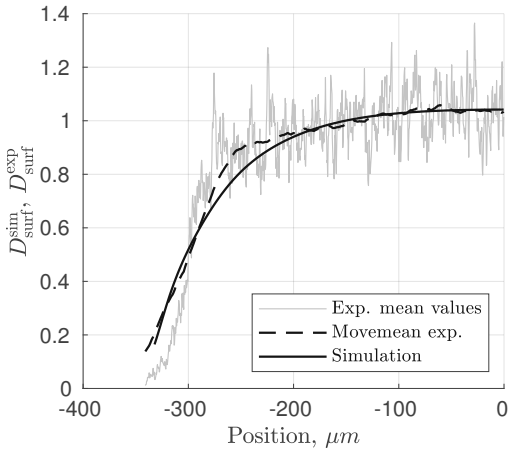

Figure 4.13: Comparison between the experimental results of experiments with layout B and the corresponding fatigue simulation calibrated with the result of layout A.

showing the moving mean of the experiments. The simulation predicts damage very similar to the moving mean of the experimental results, with the maximum damage being slightly higher than at position $\hat{x}$ in layout A. Although, the predicted increase in damage near the edge is not as steep as seen in the experiments, the overall prediction provides a satisfactory result, showing the capabilities of the framework.

4.5 Summary

Thermo-mechanically induced fatigue damage in a Cu metallization layer is analyzed numerically and experimentally using specific test devices. Experimentally, the devices are exposed to clearly defined loading conditions, which highlight the influence of the temperature distribution. SEM images of the degraded Cu surface are post-processed and analyzed to quantify the induced fatigue damage in terms of a damage density. Numerically, the devices are modeled by means of the FEM. Loading conditions resembling the experimental ones are applied to the models and the response is calculated in the form of transient thermo-mechanical analyses.

A FS FIP is calculated and the results at the surface of the Cu metallization layer are compared to experimentally obtained surface damage values. The results of a device featuring a lateral thermal gradient are used to calibrate the fatigue strength parameters of a Coffin-Manson law. With this calibration, an exceptional fit between experimental and simulated damage values can be achieved. The strong effects of seemingly small topological features of the Cu surface can be seen in the experiments and are reproduced by the simulation. Apart from these local effects, the damage is significantly higher in regions that experience higher temperatures. In a second step, the framework with the calibrated fatigue parameters is used to predict damage in a similar device without the distinct lateral thermal gradient. The predicted results show good agreement with the experimental ones.

Chapter 5

Enriched Bulk Fatigue Modeling Approach

5.1 Introduction and motivation

An important aspect of the lifetime analyses of Cu metallization layers is the number of overload pulses they can withstand until a crack has formed, which extends from the Cu surface of the metallization layer to the Cu-Si interface. Such so-called through-film cracks can be precursor to delamination and subsequent thermal runaway. In the initial proposal of the bulk fatigue framework [93], it has been assumed that the majority of the noteworthy cracks initiate due to stress concentrations caused by the device geometry, as is also shown by the example of the DMOS-cell like structures in Chapter 3. However, experimental studies such as the one presented in Chapter 4 indicate that cracks also occur in absence of macroscopic stress concentrators. While the initiation of fatigue damage in absence of macroscopic stress concentrators is a topic of ongoing research, it is known that the microstructure plays a significant role [61, 83, 86, 103]. Figure 5.1 shows part of a cross-section of the type A poly-heater presented in Figure 4.1 after accelerated fatigue loading. One can see through-film cracks that are far away from any stress concentrator and also smaller cracks that did not start at the Cu surface or at the Cu surface.

Applying the CDM fatigue framework as presented in Chapter 2 to model fatigue damage in test specimens such as type A and B poly-heaters, results in large regions of an uniformly high fatigue damage variable, D_{E}. Distinct fatigue cracks would only be predicted at the location of geometric stress concentrators, e.g. the step in polyheater design A (refer FIP values in Figure 4.8). While detecting regions that are highly prone to fatigue damage is sufficient for the surface damage studies presented in Chapter 4, it is necessary that the framework is able to predict through-film cracks if lifetime predictions are to be made for real components.

In this chapter, an extension of the original framework is proposed to allow the inclusion of information regarding the microstructure. This shall enable to simulate the initiation of fatigue cracks in the bulk metallization without stress concentrators and subsequently shall allow prediction of through-film cracks after the inevitable calibration. The fundamental concepts of the original framework in terms of usability and computation time are not affected by this extension.

5.2 Nomenclature fatigue damage and fatigue cracks

First, the terminology used in this and the following chapters is defined. It is important to clearly distinguish different stages of fatigue damage and the length scale of occurrence. As there is no universally accepted terminology, it should be noted that the nomenclature

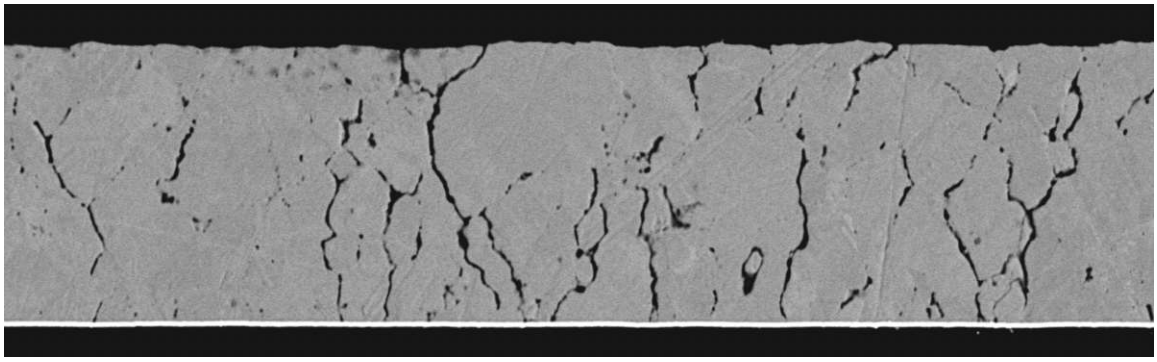

Figure 5.1: Cross-section of the Cu metallization of a layout B poly-heater after 5000 loading cycles. Courtesy of KAI.

used here may deviate from other publications. The smallest forms of fatigue phenomena considered in this work are microvoids and microcracks. In the analyzed images, this term is used to describe all forms of fatigue phenomena that are too small to be seen in the conventional cross-section SEM images, but that are known to occur based on the theory of fatigue crack initiation[8]. Within the simulation framework, this refers to the damage onset part of the fatigue life which does not lead to any material degradation. With an increasing number of load cycles, these microvoids can grow and coalesce to form macrovoids which can be seen in the cross-section SEM images as small pores in the material, see Figure 5.2. In the simulations, the term macrovoid is used to describe one or two connected finite elements in which damage evolution is initiated ($D_O = 1$). If such macrovoids continue to grow in size and coalesce, they from fatigue cracks. Examples of small fatigue cracks are shown for both, experiment and simulation, in Figure 5.2. In the SEM image cross-sections, the fatigue cracks are often not entirely continuous as they are only 2D images of 3D structures within a cross-sectional view. It has to be expected that such disconnections appear only in the visible plane and that the fatigue crack is connected out of plane. Fatigue cracks that reach from the surface of the Cu metallization to the Cu-Si interface are denoted

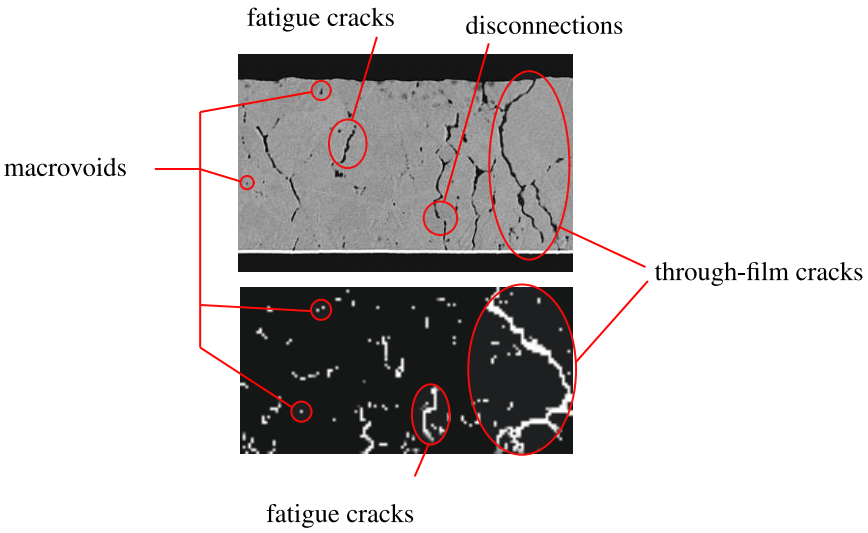

Figure 5.2: Figure of experimental and simulated cross-sections. Designations for fatigue phenomena of different sizes are given.

as through-film cracks. Examples of through-film cracks are highlighted in the simulated and experimental cross-section. All forms of macrovoids and fatigue cracks combined are denoted as fatigue damage.

5.3 Initial studies

Initially, studies have been conducted in which randomly distributed, fully damaged finite elements of the bulk material act as local stress concentrators. While resulting in distinct fatigue cracks this approach is disregarded since it would correspond to initially visible macrovoids in the pristine metallization layer. This is not backed by experiments. Instead, the microstructure promotes a faster formation of initial voids at certain positions during the loading cycles. To model this behavior, a spatially varying variable $s(\vec{x})$ is proposed which influences the damage initiation. This variable is introduced to Equation (2.5) as

$$FIP = s(\vec{x}) \cdot \gamma_{\mathrm{f}}'(2N_{\mathrm{O}})^{c_\gamma} \tag{5.1}$$

and describes the susceptibility of the material to the formation of voids dependent on the spatial location $\vec{x}$. In the following, $s(\vec{x})$ is defined individually for every element at the beginning of the simulation with $s = 1$ being the default value. Values in the range of $[0; 1[$ correspond to a lower number of cycles until damage onset occurs and values larger as 1 correspond to a higher number of cycles until damage onset occurs.

Using this approach, initial studies are conducted to test the effect of different probability distributions of $s(\vec{x})$ and to see if such an approach generally results in fatigue cracks that are comparable to experimental evidence. Furthermore, it is investigated whether a microstructural property such as the number of grains or triple junctions per area can be used to define a probability distribution of s that adequately represents the microvoid formation. Three probability distributions are presented in the following, (i) a random distribution based on the triple junction density, (ii) a Gauss distribution, and (iii) a continuous uniform distribution of the values of s.

All fatigue simulations are conducted using a plane strain Cu (20 µm layer thickness) on Si (15 µm layer thickness) bi-layer model as shown schematically in Figure 5.3. In lateral direction the model extends over 90 µm. The model is meshed regularly using isoparametric, four-node, linear interpolated, and fully integrated elements with a characteristic element length of 0.33 µm. Only the central 60 µm of the Cu layer are considered to be enriched using $s(\vec{x})$, which means that on both sides, the elements within the outermost 15 µm have a fixed value of s equal 1. This is done to avoid any edge effects. The material properties are given in Tables A.1 to A.4, Appendix A. The bi-layer is loaded homogeneously with heating pulses of 100 °C → 400 °C → 100 °C similar to those used in Chapter 4. As mechanical boundary conditions, the lateral displacements are restricted at the left and the right boundary and all displacement is restricted at the bottom nodes. For this demonstrative studies, the same fatigue parameters are applied as being used in [95], see Table 3.2.

For the given boundary conditions and prior to the occurrence of material degradation, the FIP (compare Equation (2.2)) has the same value for all elements of the Cu layer. However, since the parameter s is introduced, the initiation of the damage evolution is no longer solely dependent on the FIP, as elements with a lower value of s show an initiation of damage at lower cycle numbers.

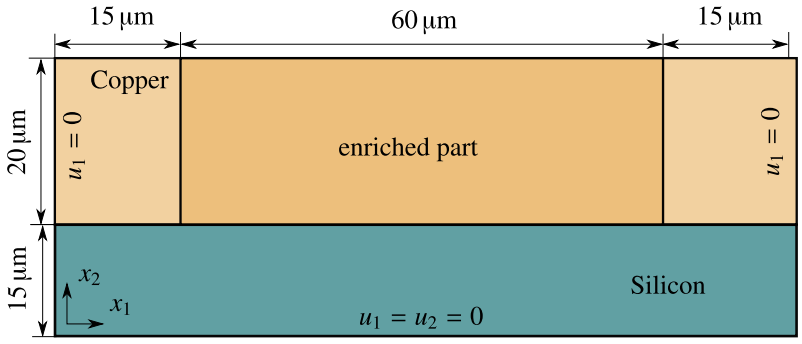

Figure 5.3: Model dimensions and boundary conditions of the initial studies.

Triple junction density

In this case, for $0,91\%$ of the elements, the value of s is set to 0.1, while all other elements have a value of $s = 1.0$. The prevalence is based on an estimation of the number of triple junctions per μm^2 in a representative cross-section. The obtained random distribution of s is schematically presented in the left of Figure 5.4. The distribution of the damage onset variable D_O after the initial cycle jump is shown for the Cu layer in the top right of Figure 5.4. It can be seen that the damage onset variable D_O reflects the positions where the values of s are set to 0.1.

Consequently, at these locations macrovoids begin to form, and damage evolution leads to local material degradation. This, in turn, acts a local stress concentrator and leads to an accumulation of damage at these locations and finally to the formation of fatigue cracks. In the bottom of Figure 5.4 the damage evolution variable D_E is depicted for the Cu layer after a significantly higher number of load cycles. At this state, large fatigue cracks have formed that can be interpreted as through-film cracks. Quite a number of elements that have been assigned a low value of s do not lead to the formation of fatigue cracks, which can be attributed to shielding effects of nearby cracks, as discussed in Chapter 3.

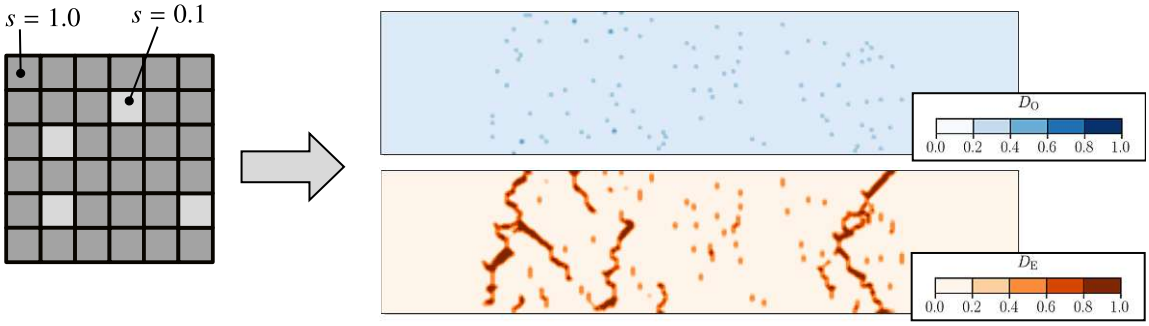

Figure 5.4: Triple junction density approach. The left figure represents a schematic distribution of s based on the triple junctions density. The top right picture depicts the distribution of the damage onset variable D_O in the Cu layer after the initial cycle jump, whereas the bottom right picture shows the distribution of the damage evolution variable D_E after through-film cracks have formed.

Gauss distribution

In this model, the values of s of all elements are defined by a Gaussian random distribution with the expectation of the distribution being $\mu_{\text{Gauss}} = 1.0$ and the standard deviation being $\sigma_{\text{Gauss}} = 0.3$. This means most of the elements have a value of s close to 1.0, but the extreme values can be significantly larger or smaller than 1.0. Negative values are multiplied by -1. A schematic representation of this approach is shown on the left side of Figure 5.5. In contrast to the selected values of the triple junction density approach much lower values of s occur, and cracks begin to form at lower cycle numbers. With the first elements reaching $D_{\text{O}} = 1$, many other elements have values of the damage onset variable D_{O} that are significantly higher than their surroundings, while not yet having reached damage evolution. This is indicated by the darker shades of blue in the top right of Figure 5.5. While the Gauss distribution implies that most of the elements have a similar value of D_{O} as the not enriched section of the Cu layer, it can also be seen that a few elements which have a notable smaller value of D_{O}, caused by their value of s being significantly larger than 1.

The resulting fatigue crack patterns differ from those of the previously discussed triple junction density approach. While distinct cracks that shield their surroundings form again,

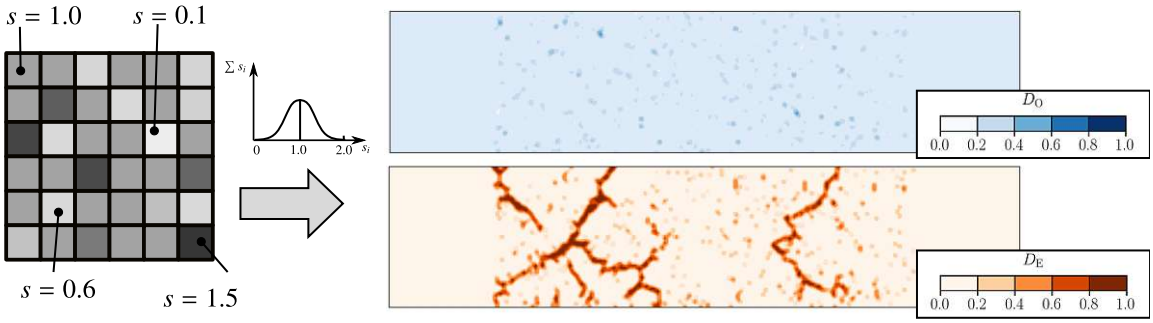

Figure 5.5: Gauss distribution approach. The left figure represents a schematic Gaussian distribution of s. The distribution of the damage onset variable D_{O} in the Cu layer after the first cycle jump is depicted in the upper right figure, whereas the bottom right figure shows the damage evolution variable D_{E} after through-film cracks have formed.

a higher number of smaller fatigue cracks and macrovoids are visible at the end of the simulation.

Continuous uniform distribution

The last s distribution tested in the initial studies is a continuous uniform distribution. Here, all elements are assigned a random value of s, ranging from 0.1 to 1.5, with all values having the same probability. Compared to the other two approaches, this results in more relatively low values of s and thus more damaged elements at lower cycle numbers, as can be seen in Figure 5.6. The resulting fatigue cracks are less pronounced and frayed and a lot of secondary damage in the form of macrovoids is visible. Still, through-film cracks form, but the overall result is less comparable to the experimental cross-section (ref Figure 5.1) than the previous two results.

Summary of the initial studies

Overall, it can be summarized that the triple junction density and the Gauss distribution approaches show promising results in terms of visual comparison with experimental observations. However, to be able to proceed with the calibration of the framework, an approach

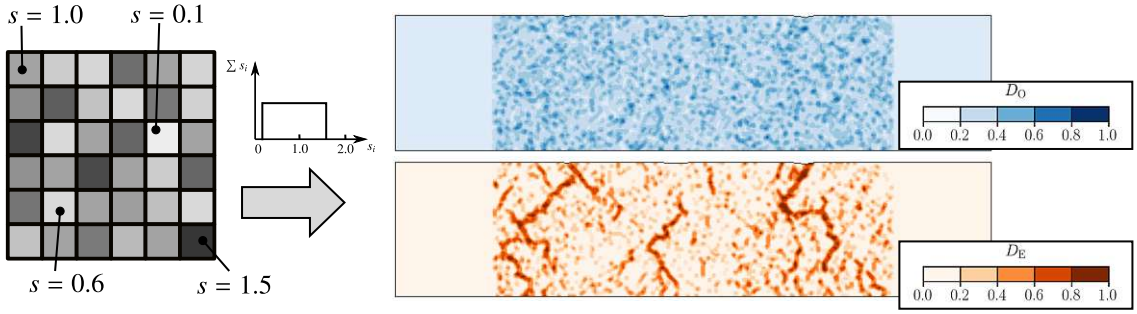

Figure 5.6: The left figure represents a schematic continuous uniform distribution of the parameter s, describing the susceptibility of the material to the formation of voids. The distribution of the damage onset variable D_O in the Cu layer after the first cycle jump is depicted in the upper right figure, whereas the bottom right figure shows the damage evolution variable D_E after through-film cracks have formed.

that is physically motivated and flexible enough to allow calibration is necessary. The triple junction density approach is loosely based on microstructural properties, but a more precise representation would be favorable that also leaves room for calibration of s. The Gauss distribution has more parameters to allow calibration but it lacks any physical motivation. Therefore, the triple junction density approach is extended in a way that allows to better account for the microstructure while still leaving room for calibration.

5.4 Enrichment based on grain misorientation angles

As written in the introduction to this chapter, it is known that the initial voids that later grow into fatigue cracks tend to form at specific locations in the microstructure. Research by the industry partner shows that, for the given Cu metallization, most voids form at grain boundaries, especially at triple junctions [43]. This is illustrated by Figure 5.7. In this figure SEM images obtained by electropolishing [67] after 300 loading cycles (a) and after 750 loading cycles (b) ($T_\mathrm{B} = 100\,^\circ\mathrm{C} \rightarrow T_\mathrm{P} = 400\,^\circ\mathrm{C} \rightarrow T_\mathrm{B}$) are shown. In Figure 5.7 (a) it can be seen that a few voids have already formed, with most of them located at the position of grain triple junctions. Figure (b) shows that after additional 450 loading

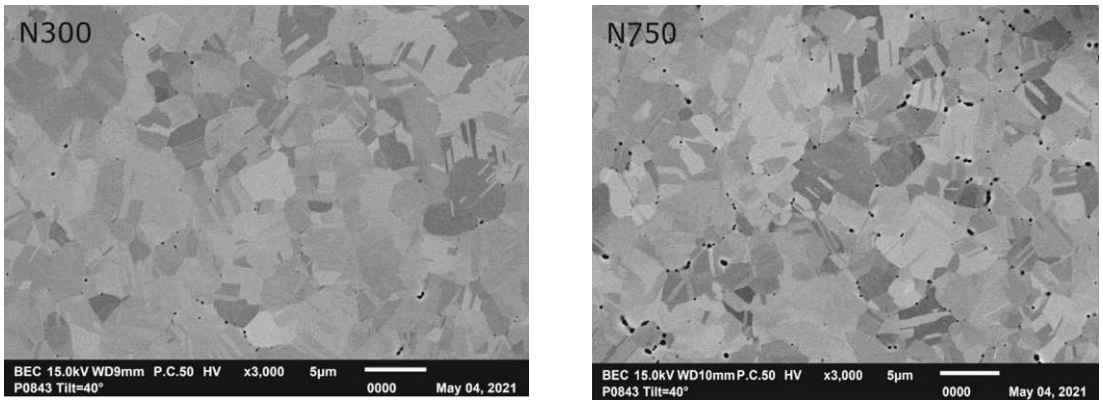

(a) (b)

Figure 5.7: E-polished SEM images of thermo-mechanically stressed Cu metallization layers after 300 (a) and 700 (b) load cycles. Taken from [43].

cycles more voids have formed and that some voids already started to increase in size and to coalescence into fatigue cracks along grain boundaries.

To account for these findings, the triple junction density enrichment approach is modified to a distribution of s that is based on the grain microstructure. Consequently, two questions have to be answered. First, on which microstructural descriptors should the quantitative distribution of s be based and second, how should s be spatially distributed. For the quantitative distribution of s the grain misorientation angles at the position of triple junctions are chosen as the material feature to model the materials' susceptibility to void formation. With currently available information on void nucleation, this approach is considered to be a viable compromise between applicability and accuracy. One way of defining a spatial distribution of the values of s is to specify s for each element individually and independently based on an overall statistical occurrence of triple junctions. However, the spatial distribution component of the grain structure is considered to be too important to be entirely disregarded. Therefore, the information of triple-junction positions and misorientation angles is introduced in the form of actual triple junction distributions obtained from Electron Backscatter Diffraction (EBSD) images.

An exemplary distribution of triple junctions extracted from EBSD images is shown in Figure 5.8 (a). In the enriched framework, such a distribution is superimposed on the FEM mesh. The advantage of using real EBSD images as a basis for the enrichment approach is that the information about grain size and grain boundaries is implicitly included in the simulations, with the mesh being completely independent of the grain structure. An important aspect of this work is to relate the information of the triple junctions shown in Figure 5.8 (a) to the values of s used in the simulations. Accompanying studies [43] conducted by the industry partner have shown that some grain boundaries are more susceptible to voiding than others. Initial voids form especially at triple junctions with at least one misorientation angle of approximately 35°, whereas fewer voids form at significantly lower or higher misorientation angles [86]. The occurrences of the specific misorientation angles of the triple junctions shown in Figure 5.8 (a) are presented in Figure 5.8 (b). It can be seen that the majority of grain boundary misorientation angles are in the range $[30°, 40°]$.

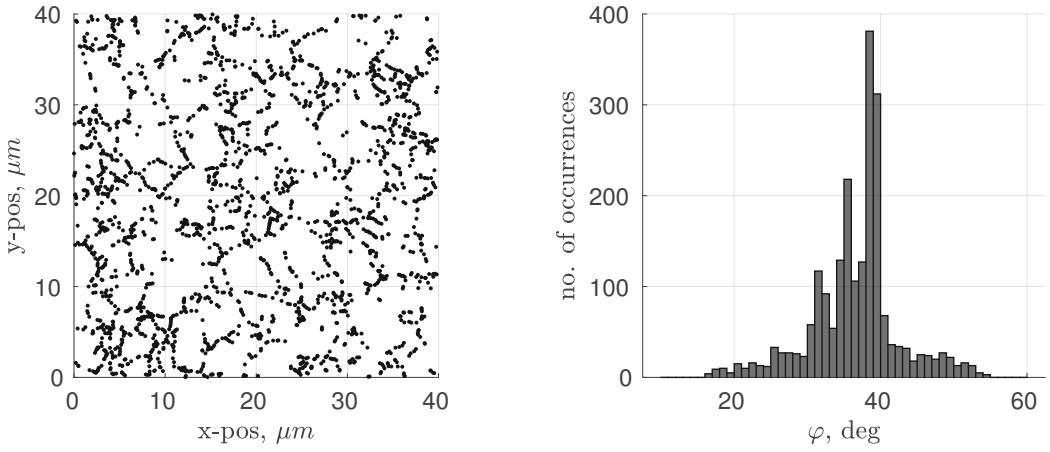

(a) **(b)**

Figure 5.8: Depiction of a representative spatial distribution of triple junctions (a) and histogram (bin size=1°) associated misorientation angle (b) for the given Cu metallization layer.

Based on this information, s is defined corresponding to the misorientation angles between an upper threshold misorientation angle value of 55° and a lower one of 15°. It is subsequently denoted as s_φ and piecewise defined as

$$s_\varphi(\varphi) = \begin{cases} \dfrac{r}{\varphi + a_\varphi} + b_\varphi & 15° \leq \varphi \leq 35° \\ \dfrac{-r}{\varphi + a_\varphi} + b_\varphi & 35° < \varphi \leq 55° \end{cases} \tag{5.2}$$

with a shape parameter r that needs to be determined from experiments and the misorientation angle φ. The constants a_φ, and b_φ, dependent directly on r, the minimum value of s_φ at $\varphi = 35°$, and the previously explained assumption of $s_\varphi(\varphi \geq 55 \vee \varphi \leq 15) = 1$. In Figure 5.9(a) the resulting distribution of s_φ for the grain structure shown in Figure 5.8 is given for an assumed minimum value of $s_\varphi = 0.25$ and various values of r. Since three grain boundaries congregate at each triple junction which all have an individual value of $s_\varphi^{i=1,2,3}$

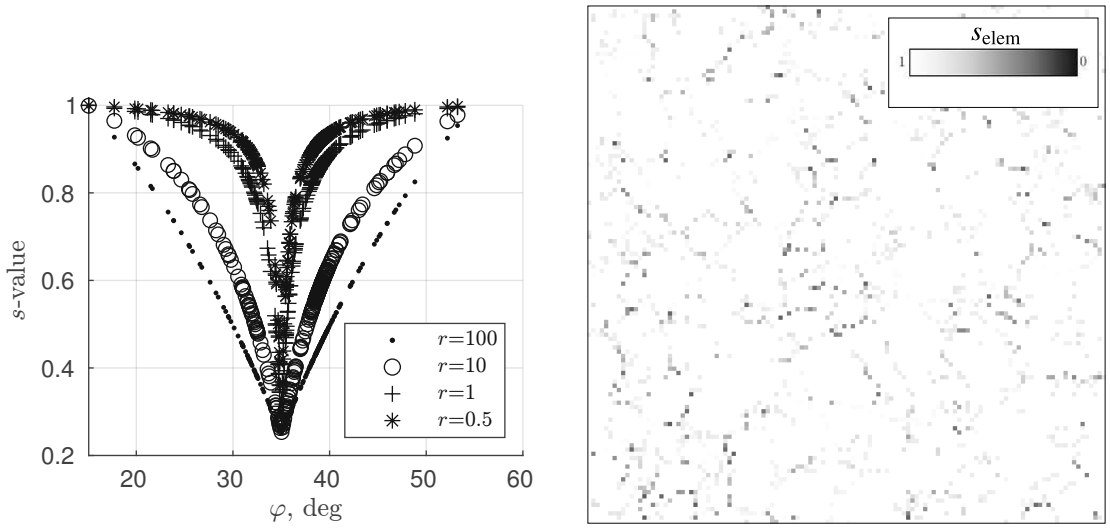

Figure 5.9: Figure (a) shows s_φ of the misorientation angle of Figure 5.8 (b) for various values of the shape parameter r. Figure (b) shows the susceptibility to void formation of individual finite elements s_{elem} based on the triple junction distribution of Figure 5.8 (a) using a mesh size of 0.33 µm and r value equal 0.5.

but only one scalar value per junction can be used within Equation (5.1), the s_{tp} parameter of each triple junction is defined to be $s_{\text{tp}} = \min(s^i_\varphi)$. It has to be emphasized that the shape of the function $s_\varphi(\varphi)$ should be understood as a first approach on how a correlation between misorientation angle and susceptibility to void formation can be described within a CDM fatigue damage framework. Further studies could help to improve this function such that it reflects the actual physical mechanisms.

Each triple junction is located within an element in the FEM model, where the number of triple junctions within the elements depends on the characteristic element size. The values of s associated with a specific finite element are defined on the basis of the values of s_{tp}. If there are multiple triple junctions within an element, s_{elem} is defined to be the smallest value of s_{tp}, otherwise $s_{\text{elem}} = s_{tp}$. The characteristic element size should be chosen within reasonable bounds. The lower bound is determined by requirements on the computing time. The upper bound should be chosen in a way that individual triple junctions, that are prone to voiding, are not overrepresented, i.e., that they do not influence a disproportionately large

area. Figure 5.9 (b) is a schematic representation of how the triple junction distribution of Figure 5.8 (a) translates to the distribution of s_{elem} when a mesh size of 0.33 µm is used. Each pixel represents one element. White elements represent $s = 1$, darker values represent lower values of s.

5.5 Parameter study

The enrichment approach based on misorientation angles is applied to a simplified FEM model of a Cu metallization on a Si substrate similar to the one used for the initial studies. The plane strain model consists of a Cu metallization layer ($h_{\text{Cu}} = 20\,\mu\text{m}$) as is shown in Figure 5.10. The enriched area of the Cu layer is 40 µm wide with 15 µm of Cu with a consistent value of $s_{\text{elem}} = 1$ on both sides. To better represent the loading conditions that occur in corresponding test chips, a full Si thickness ($h_{\text{Si}} = 120\,\mu\text{m}$) is modeled. The boundary conditions are enhanced by including a slider boundary condition on the right

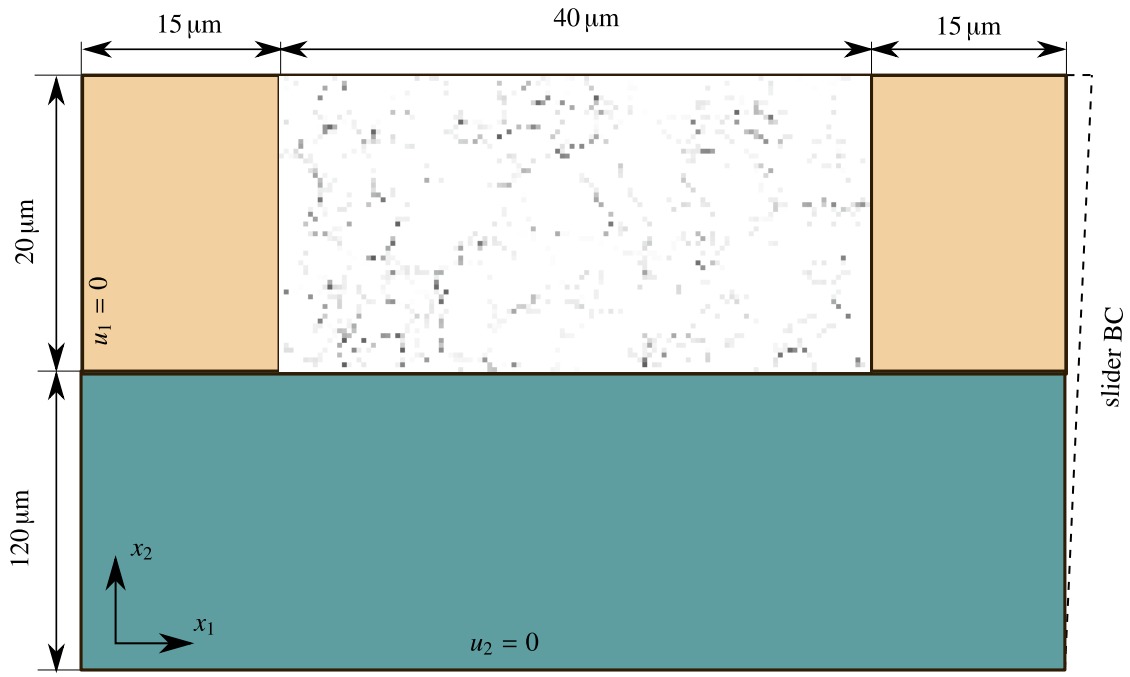

Figure 5.10: Model dimensions and boundary conditions. A schematic representation of the s_{elem}-value is given for the enriched area.

side of the model. This boundary condition consists of multi-nodal kinematic constraints. In the given case, all nodes on the right side of the model have to stay on a straight line between the top node of the Cu metallization and the bottom node of the Si substrate. This allows the entire model to expand in the x_1-direction, while the expansion in the Cu metallization is restrained by the less expanding Si substrate. The remaining boundary conditions, the element types, the material properties, and the heating pulses are the same as for the initial studies (Section 5.3). The fatigue parameters of the FS damage initiation law are taken from the surface studies presented in Chapter 4 ($\gamma'_{\mathrm{f}} = 0.1389$, $c_\gamma = -0.3521$).

To illustrate the capabilities of the approach, two-parameter studies are presented. The first parameter that is being varied is r introduced in Equation (5.2) defining the shape of the distribution of s. Varying its values as shown in Figure 5.9 (a) makes the initiation of fatigue damage more or less sensitive on the chosen minimum misorientation angle. In case of high values ($r > 10$) fatigue damage is expected to initiate at many triple junctions more or less simultaneously. Less fatigue damage initiation is expected for smaller values of r. In this chapter results for r =0.5, 1, 10, and 100 are presented.

The second parameter that is varied is κ_1 from the damage evolution law (cf. Equation (2.10)). This parameter effects how fast the material degrades after damage onset. As an example, results for $\kappa_1 = 1 \times 10^{-7}$, 5×10^{-7}, and 1×10^{-6} are presented. The second parameter of the damage evolution law, κ_2, is set to be 0.45 and $\alpha_{\mathrm{H}}^{\max}$ (cf. Equation (2.9)) is set to 0.006 as stated in [93]. The parameter $s_{\min}$ in Equation (5.2) is set to a fixed value of 0.25.

The simulation results are presented in two different ways. Firstly, the evolving fatigue damage is depicted in terms of conventional contour plots, as shown in Section 5.3. This gives a rough estimate of whether the resulting damage patterns correspond to those observed in actual experimental cross-sections. However, it is not optimal in terms of quantitative

comparability with experimental results. Secondly, the mean fatigue damage for a specific load cycle are calculated as

$$D_{\text{mean}}(N) = \frac{1}{n}\sum_{i=1}^{n} D_{\text{E}}^{(i)}(N) \tag{5.3}$$

with n being the number of elements in the enriched area and $D_{\text{E}}^{(i)}(N)$ the damage evolution variable of element (i) after N cycles.

The results are highly dependent on the particular realization of the triple junction distribution used for the simulation. To mitigate this dependency, multiple simulations based on different triple junction distributions are conducted for each set of κ_1 and r. From these individual simulations, a mean damage $\bar{D}$ over all simulations is calculated as

$$\bar{D}(N) = \frac{1}{m}\sum_{j=1}^{m} D_{\text{mean}}^{(j)}(N) \quad , \tag{5.4}$$

with m being the number of triple junction distributions utilized for the given set of parameters. In the following discussions, the term fatigue damage is used synonymously with $\bar{D}$ unless otherwise stated. Simulations based on six individual EBSD images and are presented in Figure 5.11 for $r = 1$, $\kappa_1 = 5 \times 10^{-7}$. The simulations experience convergence issues after through-film cracks occur. Therefore, some of the simulations stop before reaching 5000 cycles. These aborted simulations are disregarded for the calculation of $\bar{D}(N)$ according to Equation 5.4.

The curves $D_{\text{mean}}^{(j)}(N)$ obtained for the different triple junction distributions have similar shapes which are characterized by three phases. Around 160 cycles, the first elements reach damage onset (D_{O}=1). The number of load cycles to reach this point is strongly dependent on s_{min}, in the sense that a lower value would shift this point to lower cycle numbers. Afterwards damage evolution starts leading to an almost linear increase of fatigue damage lasting until $N \approx 2300$. This initial phase is succeeded by a phase of more pronounced fatigue damage growth which ends around cycle number $N \approx 3500$. The last phase is defined by a slow deceleration of fatigue damage increase per cycle.

In Figure 5.12 the result of the parameter study for the shape parameter r is presented in form of the mean damage variables $\bar{D}(N)$, when $\kappa_1 = 5 \times 10^{-7}$ for all simulations. Although fatigue damage starts at almost the same cycle number ($s_{\min} = \text{const}$) for all values of r, higher values of r result in a much faster increase of $\bar{D}$. All of the curves eventually level out to an almost constant value. For higher values of r the value of $\bar{D}$ at which the curves level

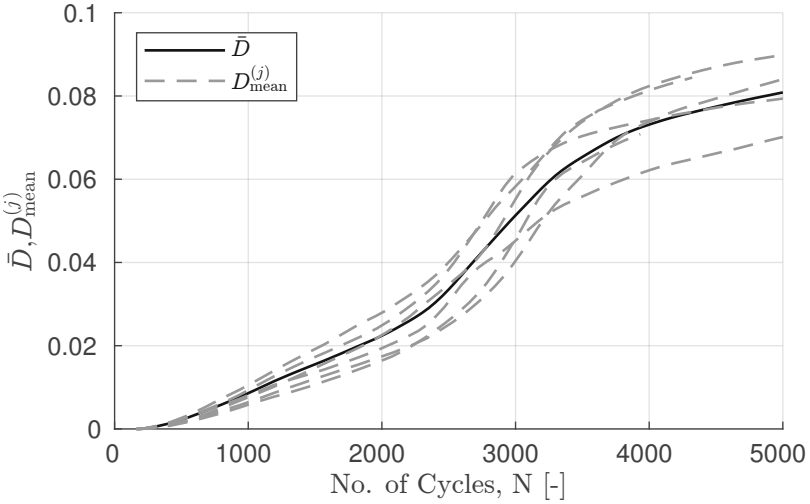

Figure 5.11: This figure shows the $\bar{D}$ against no. of cycle plots of six simulations based on different EBSD images and the corresponding mean value ($r = 1$, $\kappa_1 = 5 \times 10^{-7}$). In this case, four out of the six individual simulation did not abort and are therefore used to calculated $\bar{D}$.

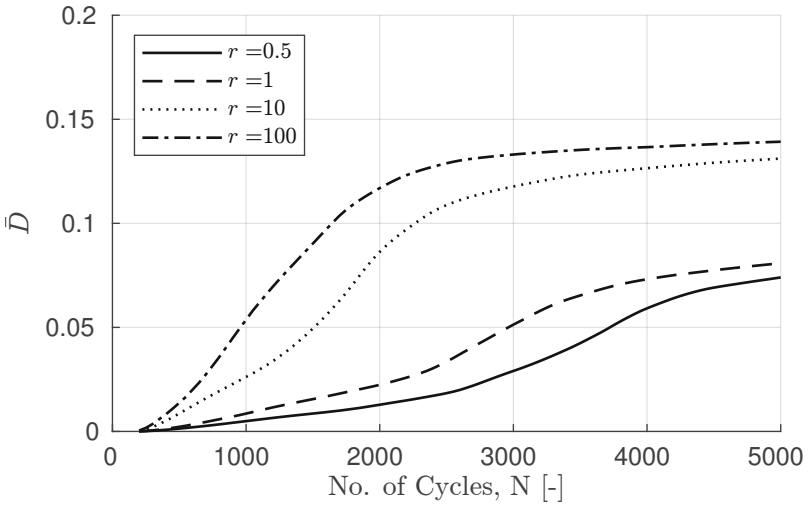

Figure 5.12: This Figure depicts mean $\bar{D}$ values for different values of r.

out is higher and it is reached at lower cycle numbers. These effects can be comprehended referring to Figure 5.9 (a). Higher values of r imply a flatter shape of the s_φ curve, which in turn means that more elements have relative low values of s and therefore initiate damage evolution at lower cycle numbers. The leveling out can be explained by the shielding effects of the long fatigue cracks, which prevent further fatigue crack growth.

These results are further highlighted when looking at the fatigue cracks developing during the simulations as shown in Figure 5.13. In this figure, greyscale contour plots of D_E in the enriched region of the model are given at different cycle numbers but for the same triple junction distribution, respectively. Black areas are undamaged with $D_\mathrm{E} = 0$, whereas white areas indicate completely damaged elements ($D_\mathrm{E} = 1$). For $r = 0.5$ and $r = 1$ much less elements reach a completely damaged state, especially during the first 2000 cycles. The

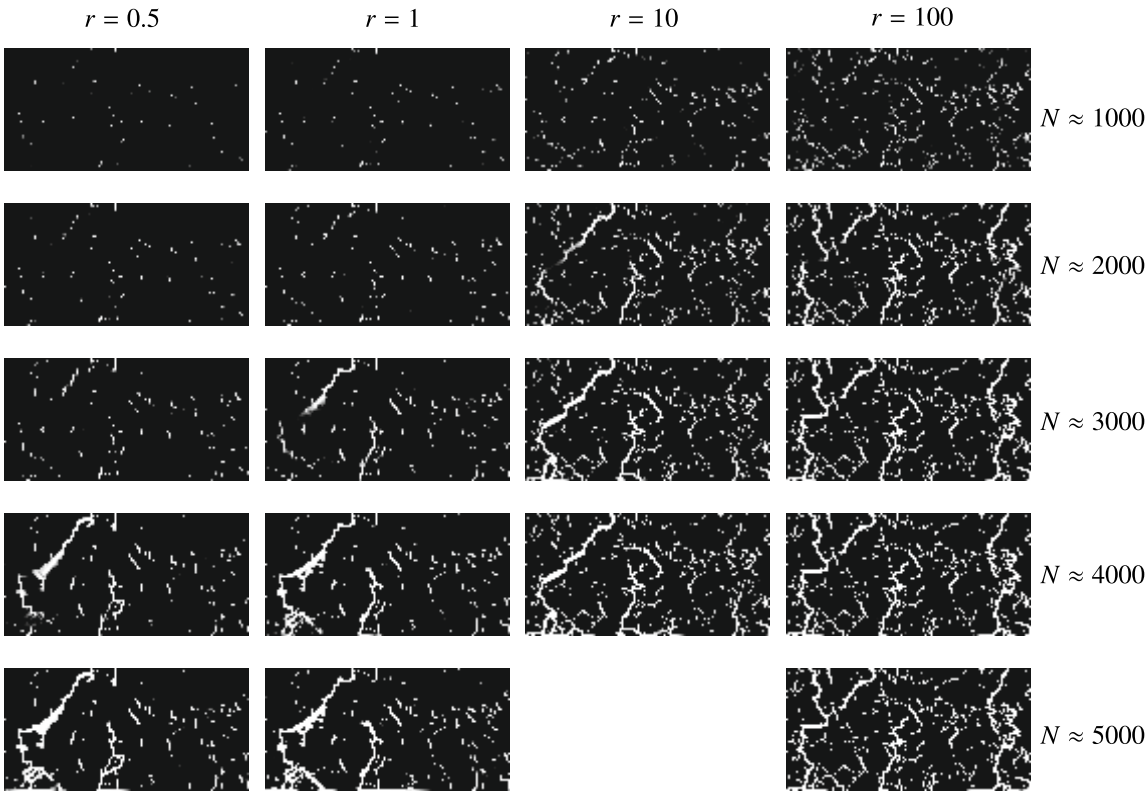

Figure 5.13: Respective images of the enveloping fatigue damage for different values of r. For the given triple junction distribution the simulation for $r = 10$ did not reach 5000 cycles.

damage patterns are dominated by distinct cracks, with less secondary damage in the form of macrovoids and smaller fatigue cracks. In case of $r \geq 10$ more smaller fatigue cracks can be seen. Moreover, the Cu layer seems to be completely damaged at 3000 cycles, with very little additional damage forming afterwards (which confirms to Figure 5.12). Certain aspects of the damage patterns form independently of the value of r, such as the large crack on the left side of the model. This is to be expected since all presented results are based on the same triple junction distribution.

Figure 5.14 shows the second parameter study in which κ_1 is varied while r is kept constant at $r = 1$. The variation of κ_1 influences the growth of fatigue damage directly. Lower values of κ_1 mean that it takes longer for an element that has reached damage onset to become fully damaged at $D_{\mathrm{E}} = 1$. This also means that less shielding effects occur at low cycle numbers, which in turn lead to more damage. The curve of the largest value of κ_1 initially experiences the highest increase of damage while also leveling out the fastest. The other two curves with lower values of κ_1 show initially lower values of $\bar{D}$ but at higher cycle numbers higher values of $\bar{D}$ are reached for the curve for $\kappa_1 = 5 \times 10^{-7}$ surpassing the $\bar{D}$ level of $\kappa_1 = 1 \times 10^{-6}$. The curve for $\kappa_1 = 1 \times 10^{-7}$ does not even level out during the 5000

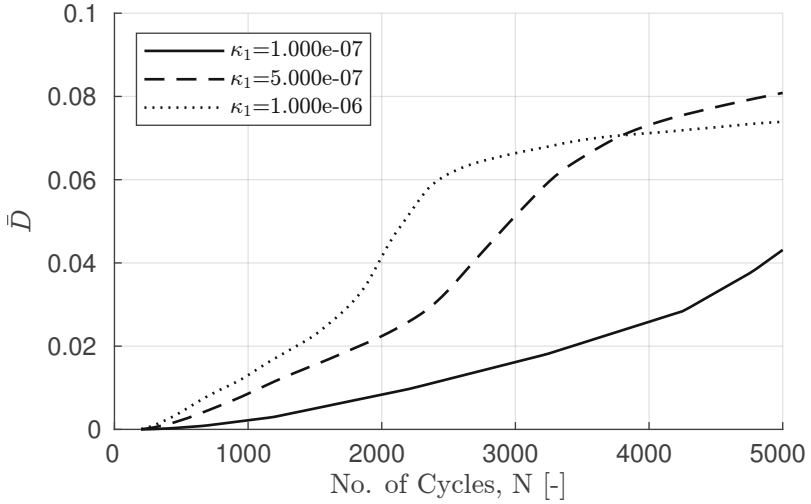

Figure 5.14: This Figure depicts mean $\bar{D}$ values for different values of κ_1 with a constant value of $r = 1$.

cycles. It can be expected that much higher $\bar{D}$ values would be reached if the simulation was continued to higher cycle numbers (i.e. a higher crack density at saturation).

The corresponding contour plots are given in Figure 5.15. It can be seen that in the case of the $\kappa_1 = 1 \times 10^{-7}$, large fatigue cracks have not yet formed at 5000 cycles. In the case of the larger values of κ_1, distinct fatigue cracks have already emerged at 3000 cycles, including a through-film crack being visible for $\kappa_1 = 1 \times 10^{-6}$. In general, it can be concluded that larger values of κ_1 lead to a faster formation of distinct fatigue cracks, which in turn leads to a more pronounced shielding of smaller non-dominant cracks. Therefore, less secondary damage in the form of macrovoids and small fatigue cracks can be observed for higher values of κ_1.

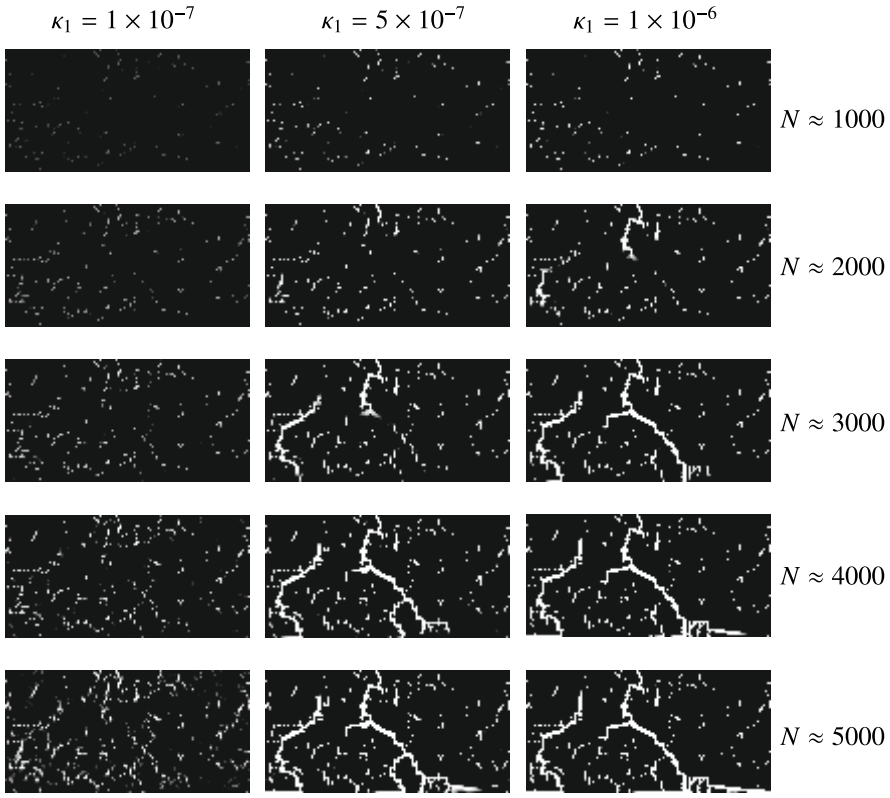

Figure 5.15: Respective images of the enveloping fatigue damage for different values of κ_1 with constant value of $r = 1$.

The last result presented in this chapter is the estimation of the first occurrence of a through-film crack for the individual simulations in terms of cycle numbers. One illustrative example of such a through-film crack is the central fatigue crack shown in Figure 5.15 for $\kappa_1 = 1 \times 10^{-6}$ and $r = 1$ at 3000 cycles. In order to compare the corresponding cycle numbers of the individual simulations, they are summarized as boxplots in Figure 5.16. Figure (a) shows the number of load cycles at which through-film cracks occur for the study on the variation of the shape parameter r. It can be seen that lower values of r lead to higher cycle numbers at which a through-film crack occurs. It is noteworthy that the difference between the median values obtained for $r = 10$ and $r = 100$ is relative small, while $r = 100$ leads to much larger scattering than obtained for $r = 10$. Figure 5.16 (b) depicts the results for the parameter study on κ_1 omitting the results of $\kappa_1 = 1 \times 10^{-7}$, since in that case no through-film cracks have formed during the first 5000 cycles. It is emphasized once again that it takes more loading cycles for simulations utilizing smaller values of κ_1 values to form through-film cracks than for ones with high values of κ_1 as is already indicated in Figure 5.15.

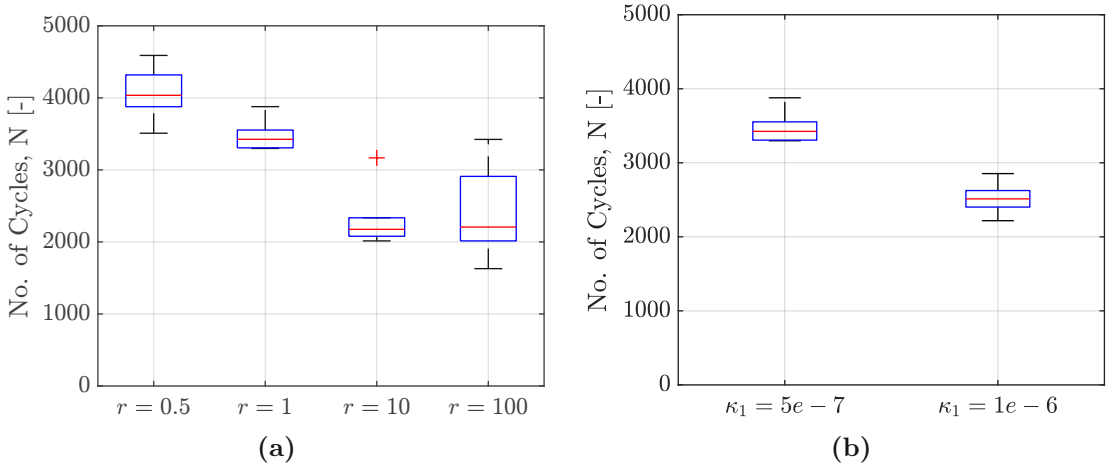

Figure 5.16: Box plot of the cycle numbers of the first appearing through-film cracks during the r value study (a) and the κ_1 study (b)

5.6 Summary

An enrichment approach is presented that allows to incorporate governing information about grain microstructure into an established CDM based fatigue model while keeping the modeling effort in reasonable limits. Previous studies [43] have shown that in micrometer-scale semiconductor devices, the grain structure can determine at which position macrovoids form during thermo-mechanical cyclic loading, which subsequently lead to the formation of fatigue cracks. The presented approach is based on an enrichment by introducing a local parameter that describes the susceptibility to void formation at a particular material pointand consequently the onset of fatigue damage. In difference to the original approach, the enriched formulation is capable of modeling distinct fatigue cracks in absence of geometry induced stress concentrators.

Initial studies utilizing stochastically distributed values of the susceptibility parameter, provide insights into how such an approach influences the fatigue damage predicted using a simplified model of a metallization on an Si substrate. Based on this results, a formulation using information of actual grain microstructures is considered a better approach in terms of physical motivation and also calibration capabilities. The misorientation angles at the position of triple-junctions are chosen to be the microstructural descriptors that are related to the susceptibility of fatigue damage and are consequently the basis for the enrichment. The models are enriched utilizing actual triple-junction distributions taken from EBSD images.

Two parameter studies are presented, highlighting the capabilities of the enrichment approach. The first parameter affects the susceptibility of triple junctions to the formation of voids in terms of their sensitivity to specific grain boundary misorientation angles. Varying this parameter has great influence on the amount of secondary damage that forms during the fatigue simulations. The second parameter affects the damage evolution and thus the number of cycles it takes for microcracks to grow into macrocracks and how fast macrocracks subsequently form through-film cracks. Results of these studies are presented in the form of mean damage variables and fatigue crack contour plots. The parameter studies in-

dicate great calibration possibilities, and the contour plots are comparable to experimental images even at this early stage. The results are further utilized in the next chapter, which focuses on comparison to experimental results and the calibration of the framework.

Chapter 6

Parameter Estimation for the Enriched Bulk Fatigue Modeling Approach

6.1 Introduction

In Chapter 5, an approach is presented that allows to take information about the microstructure into account when simulating fatigue damage. It is demonstrated how the rate at which fatigue damage emerges and the amount and size of fatigue cracks can be influenced and controlled within simulation by applying this approach. A first comparison of simulation results with SEM images of a cross-section of an experimentally tested DUT is promising, yet a quantitative comparison and calibration to experimental results is inevitable if one wants to make a conclusive statement about the capabilities of the proposed approach. In this context, it needs to be kept in mind that the main interest is to predict the load cycle number when first through-film cracks form.

As a continuation of the previous chapter, this chapter discusses how simulated and experimental results of fatigue analyses can be compared in a meaningful way. The main goal is to estimate the parameters of the fatigue damage evolution law introduced in Chapter

2 and the parameters associated with the enrichment approach presented in Chapter 5. Several approaches for performing this comparison are presented and discussed, with the most suitable comparison approach being used in a parameter fitting study. In addition, the framework with the parameters estimated for the damage evolution law and the enrichment approach is applied to a large FEM model of an experimental test device.

6.2 Available experimental data

The experimental results presented in Chapter 4 are not suitable for this case, since only the surface is inspected and no statements regarding through-film cracks can be made. Therefore, additional experimental analyses focusing on the evolution of fatigue cracks inside the metallization layer are conducted by the industrial partner KAI. These analyses are done utilizing layout-B poly-heaters shown in Figure 4.1 with the loading conditions described in Chapter 4. Cross-sections are analyzed providing information on the formation of fatigue damage within the Cu metallization. The cross-sections are obtained by the Focused Ion Beam (FIB) technique and subsequent SEM image analysis. Since it is not possible to continue the cyclic temperature loading of the poly-heater after cross-sections have been prepared, multiple experiments are performed and analyzed after different cycle numbers.

Three experiments are conducted for each considered load cycle number, with two cross-sections being analyzed for each experiment. The respective cycle numbers are: $N^{\text{exp}} = [200, 1000, 1750, 2500, 3750, 5000]$. To quantify the visible fatigue damage in the cross-sections, it is necessary to binarize the images. Similar to the approach discussed in Section 4, Otsu's method is used to divide the images into damaged and undamaged regions. An exemplary comparison between the original SEM cross-section image and the binarized result is given in Figure 6.1. White areas mark macrovoids and fatigue cracks. In the binarized image, cracks of various sizes as well as macrovoids are well visible. All of these binarized images are cropped to focus on the central area of the layout-B poly-heater, where

a relatively uniform distribution of fatigue damage occurs (cf. Figure 4.13) and to avoid the regions where edge effects influence the formation of fatigue cracks.

The visible damage within the respective images is summarized into one damage variable similar to Equation (5.3). Instead of elements, this equation evaluates the pixels of the images, with the undamaged ones having a value of 0 and the damaged ones having a value of 1. Subsequently, the 6 images available for each cycle number are summarized similar to Equation (5.4) as

$$\bar{D}^{\mathrm{exp}}(N^{\mathrm{exp}}) = \frac{1}{6}\sum_{i=1}^{6}\frac{px_{\mathrm{d}}^{i}(N^{\mathrm{exp}})}{px^{i}(N^{\mathrm{exp}})} \quad , \tag{6.1}$$

to obtain an experimental mean damage variable $\bar{D}^{\mathrm{exp}}$. Here, px_{d}^{i} is the number of pixels which are classified as damaged in cross-section i (out of six) evaluated at the load cycle number N^{exp}. The number of all pixels, damaged and undamaged, in the corresponding cross-section is denoted as px^{i}.

The results of are presented in Figure 6.2 as percentage of damaged pixels for the corresponding load cycles. Here, the solid line represents $\bar{D}^{\mathrm{exp}}$, while the vertical bars indicate the minimum and the maximum values of $px_{\mathrm{d}}^{i}/px^{i}$ obtained from the images of the individual cross-sections. The large scattering in the measured fatigue damage is to be expected because many steps are involved in the processing of the cross-section and the subsequent

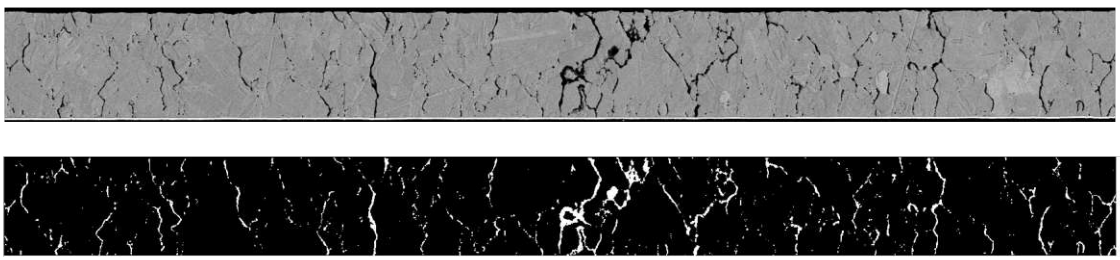

Figure 6.1: Cross-section SEM image of a layout B poly-heater after 5000 cycles (top) and the corresponding binarized image highlighting the fatigue cracks (bottom).

image analysis, which can lead to post-processing adulterations, e.g. remnants of the FIB process. The results show that the fatigue damage increases steadily, with the most significant increase being between 1750 and 2500 cycles.

6.3 Post-processing and comparison

The next step is to compare the experimental results with the simulation. It is important to keep in mind which values are being compared and to assess whether such a comparison is meaningful. One of the simulations presented in Chapter 5 ($\kappa_1 = 5 \times 10^{-7}$, $r = 1$) is used as reference result for the post-processing steps. Initially, $\bar{D}^{\text{exp}}$ (Eqn. 6.1) evaluated for the experiments and $\bar{D}^{\text{sim}}$ (Eqn. 5.4) resulting from the simulations are compared and shown in Figure 6.3. The fatigue damage as seen in simulations and experiments is in the same range. Especially, during the first 2000 load cycles, the extent of fatigue damage is remarkably similar. At higher load cycle numbers, the two curves diverge. However, this first comparison between experimental and simulated results should be interpreted with caution. One significant aspect in this context is the characteristic element length,

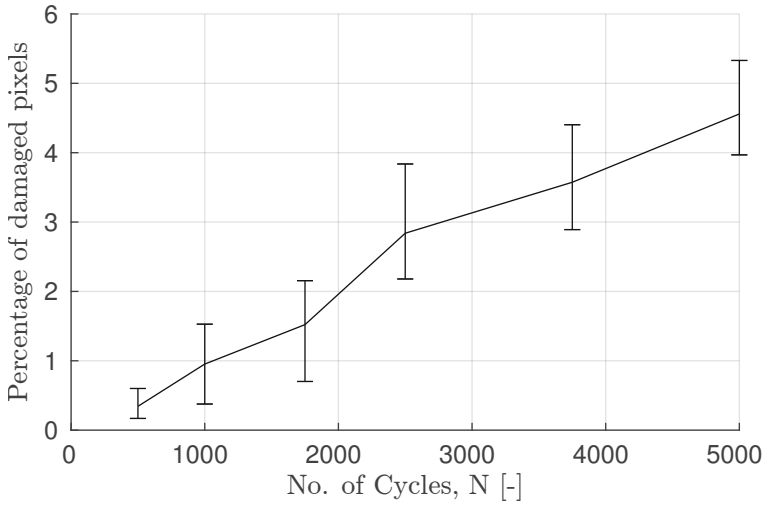

Figure 6.2: Percentage of the pixels identified as damaged over the respective load cycle numbers. The solid line shows the mean values from the different cross-sectional SEM images, at the respective cycles numbers. The vertical bars indicate the corresponding minimum and maximum values.

hereafter called mesh size, of the simulation in comparison to the pixel resolution of the SEM images. For the simulations, a mesh size of 0.33 µm is used. A smaller mesh size raises problems in terms of numerical stability and computing time. In the case of the SEM images, the length of one pixel is equal to 0.033 µm. In the simulations, the mesh size is the minimum crack width, while much finer cracks can occur and are also detected in the experiments. Figure 6.4 shows a comparison between a contour plot of a simulation and a section of one of the SEM images. The relatively similar shape of the through-film cracks seen in this figure for both results is purely coincidental and it must be emphasized that the simulation does not aim to replicate the exact fatigue crack patterns as seen in the experimental cross-sections.

The objective of the simulation is merely to be comparable in terms of the amount of visible fatigue damage and the shape of the fatigue cracks at the respective cycle numbers. For example, the overall length of fatigue cracks should be reproduced. In the case of Figure 6.4 the overall fatigue crack pattern of the simulation appears to be a good representation of the damage visible in the binarized SEM image, but the fatigue cracks in the experimental analysis are much finer which can not be reproduced by the simulation. To address

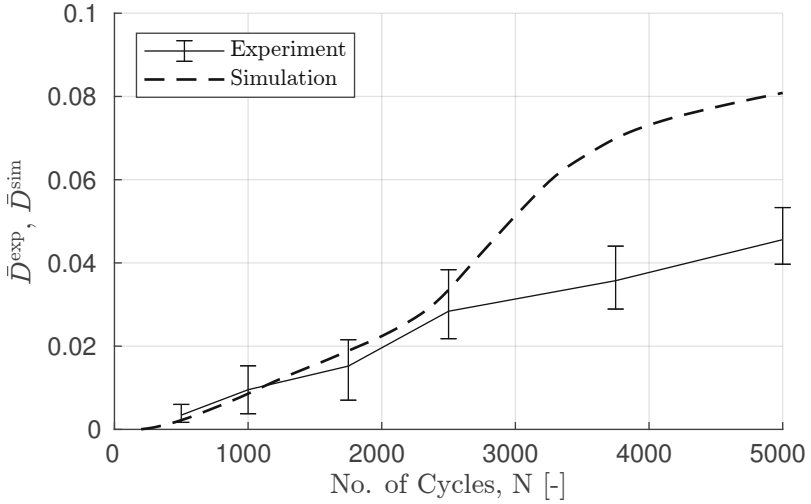

Figure 6.3: Mean fatigue crack value $\bar{D}$ from the experiments and an exemplary simulation.

these differences in representation, several approaches are being explored to provide better comparability between simulation and experiment.

6.3.1 Comparison of pixel size to mesh size

Since it is not feasible to reduce the mesh size of the simulation to the image resolution of the experiments for computational time and numerical stability reasons, it is possible to do the opposite and reduce the resolution in the experimental post-processing to match the simulations. The idea is to deliberately use an interpolation method that favors damaged pixels to widen the cracks and to obtain the same minimum crack width in the experiments as obtained in the simulations. Therefore, a second grid with the mesh size of the simulation is laid on top of the original one. The pixels of the second mesh are counted as damaged if a certain threshold of damaged subpixels of the original mesh is reached. This is schematically presented in Figure 6.5 for a threshold of 30% of damaged subpixels. The larger cracks are straightened and partly widened, while smaller macrovoids are neglected.

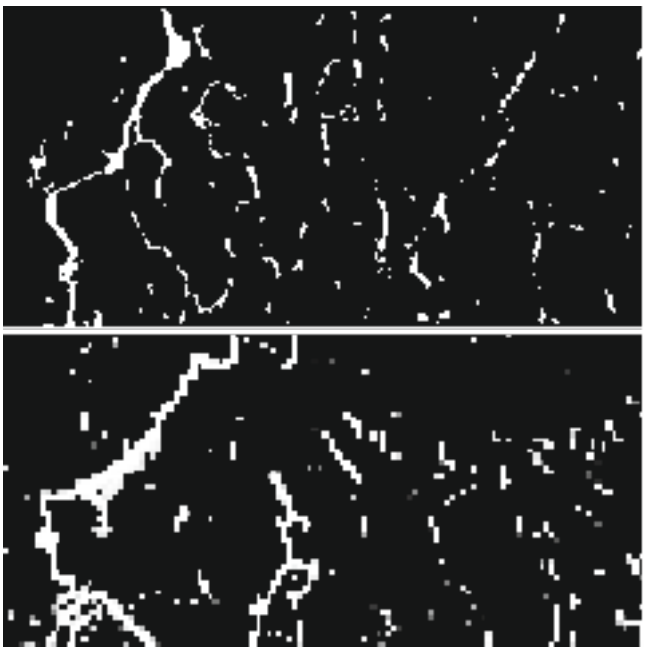

Figure 6.4: Comparison between experimental (top) and simulated (bottom) crack patterns after 5000 loading cycles.

With a threshold of 30%, this approach is applied to the experimental images, resulting in fatigue cracks that have the same minimum width as the simulated ones. From the images adjusted in this way, a mean value similar to Equation (5.4) can be calculated, denoted as $\bar{D}^{\text{exp}}_{\text{msh}}(\text{N})$. Figure 6.6 depicts $\bar{D}^{\text{exp}}_{\text{msh}}(N)$ and $\bar{D}^{\text{sim}}(N)$ as a function of load cycle numbers. Especially at the later stage, the two curves are now much closer together than in the initial comparison in Figure 6.3. With the enlarged pixel size, a larger portion of the image is registered as being damaged.

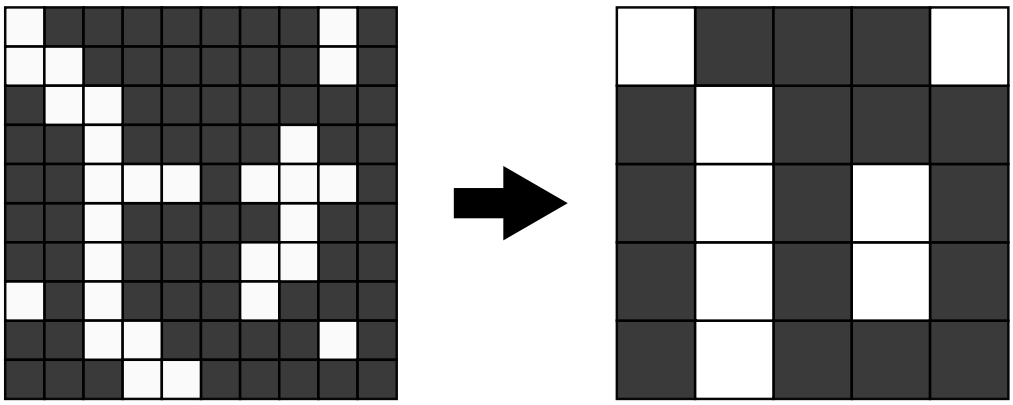

Figure 6.5: Schematic representation of the artificial coarsening of the experimental results.

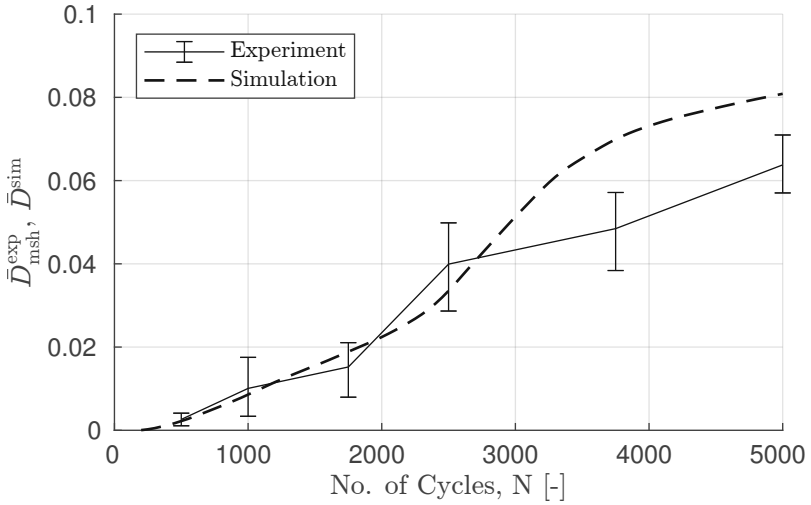

Figure 6.6: Comparison of the artificial coarsened experimental and the simulated fatigue damage values over 5000 load cycles.

While this approach partially leads to a better comparability between experiments and simulations, it also has weaknesses. Firstly, it includes an additional parameter that has to be defined. This is the threshold of damaged subpixels in the original resolution, at which the new larger pixel is counted as being damaged. For Figure 6.6 this value is used to be 30% but other values could also be chosen, influencing the results. Secondly, through this process fatigue damage information is lost as smaller macrovoids might be removed.

6.3.2 Skeletonization

The most important characteristic of the here studied fatigue cracks is their length, since most cracks form vertically and through-film cracks are the main focus of interest. Therefore, another approach for comparing simulated and experimentally determined results is to compare the length of all fatigue cracks detected. Estimating the length of all cracks in such an experimental cross-section or simulation is not a straightforward task. Path length estimations are often used in the field of medical image processing [6, 45] utilizing classic pathfinding algorithms, such as Dijkstra's algorithm [19]. In these studies, it is important that the length of the object in question is measured as accurately as possible.

This is not the case for the approach presented here, as the goal is to calibrate fatigue material parameters of bulk material. Therefore, the aim is to find a characteristic value representing the overall damage state of the material and that is comparable to the experimentally obtained results. Consequently, the length of the individual fatigue cracks is of less importance. A simple approach that can be used as an initial estimate is to skeletonize the original images and to calculate a preliminary overall crack length parameter based on these images.

Skeletonization reduces all detected fatigue cracks to one pixel or element wide structures, while keeping essential characteristics. The algorithm implemented in MATLAB and utilized in this work is based on [51] and is given in Appendix B. A schematic depiction of this process is given in Figure 6.7. The two pixels/element wide crack in the left image is reduced to a one pixel/element wide crack on the right side, with diagonal cracks only

being connected at the edges. This process can be applied to the experimental results as well as to the simulation results. Since this approach is limited to binary images, the results of the simulations must first be converted to the appropriate format. The conducted simulations are based on a regular quadratic mesh, which makes this conversion relatively straightforward. The value of the damage variable associated with damage evolution D_{E} of every element can be translated to a gray scale entry in an image matrix, which can subsequently be binarized and skeletonized. The elements are binarized in such a manner that all elements that have reached the damage onset criterion $D_{\mathrm{O}} = 1, D_{\mathrm{E}} = 0$ are evaluated as fully damaged.

An exemplary image showing the influence of the skeletonization on the results of the simulation is shown in Figure 6.8. The relative broad fatigue cracks are reduced to a single line of elements, while general characteristics of the fatigue cracks are kept intact. Smaller macrovoids are not removed by this approach.

From the skeletonized data, a damage density can be calculated for both the experimental and the simulated results, providing an estimate of the crack length per area. This is done in an equivalent way for simulation and experiment. First, the number of pixels and elements which are registered as damaged are multiplied with the characteristic element or

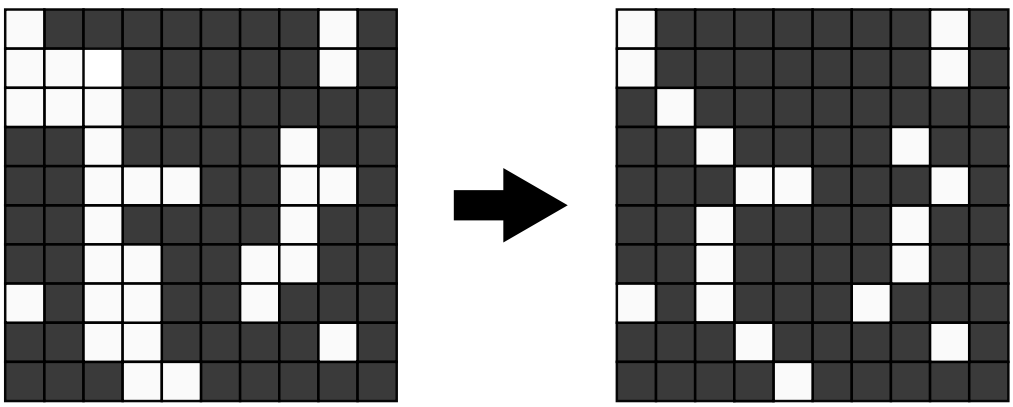

Figure 6.7: Schematic representation of the skeletonization process.

pixel length, respectively. To relate these values to the corresponding area, the results are divided by the area of the respective image or simulation section.

Taking the mean value over the six available simulations based on different triple junction distributions (cf. Equation (5.4)) this reads as

$$\bar{D}_{\mathrm{skl}}^{\mathrm{sim}}(N) = \frac{1}{6}\sum_{i=1}^{6} \frac{e_{\mathrm{d,skel}}^{i}(N)\cdot l_{\mathrm{e}}}{e^{i}(N)\cdot l_{\mathrm{e}}^{2}} \quad , \tag{6.2}$$

with $e_{\mathrm{d,skel}}$ being the number of elements which are counted as damaged after skeletonization. The overall number of elements is denoted as e, i describes the respective triple junction distribution, and l_{e} the element length of the quadratic elements.

The corresponding value for the experiments is given as

$$\bar{D}_{\mathrm{skl}}^{\mathrm{exp}}(N) = \frac{1}{6}\sum_{i=1}^{6} \frac{px_{\mathrm{d,skel}}^{i}(N^{\mathrm{exp}})\cdot l_{\mathrm{px}}}{px^{i}(N^{\mathrm{exp}})\cdot l_{\mathrm{px}}^{2}} \quad , \tag{6.3}$$

with $px_{\mathrm{d,skel}}(N^{\mathrm{exp}})$ with the number of pixels which are classified as damaged after the skeletonization. The superscript i describes the respective cross-sections taken at load cycle number N^{exp} with the overall number of pixels px^{i}. To obtain a value representing a

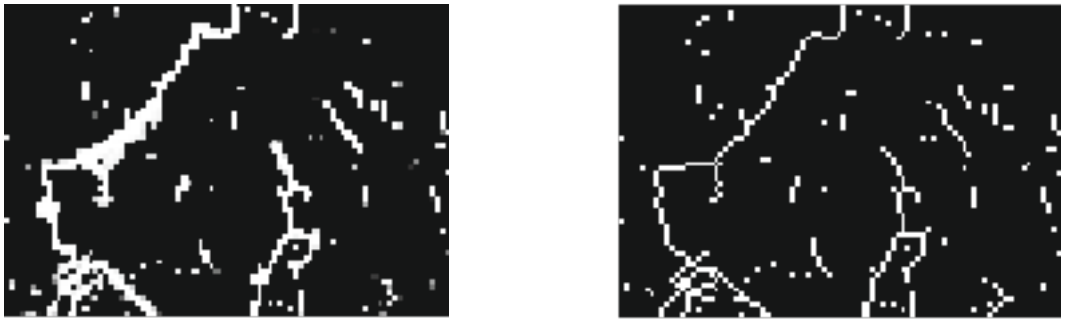

a) b)

Figure 6.8: Skeletonization of a simulated crack pattern: a) original result, b) skeletonized result.

crack length per area, a corresponding length value l_{px} must be introduced. This value is given by the experimental setup as the length that one pixel represents at the given distance of the camera setup.

Figure 6.9 shows the comparison between the experimentally obtained results and the results obtained by the simulations. During the first 2500 loading cycles the agreement is already astonishingly good, however, for higher cycle numbers, the simulations overestimate the fatigue crack length per area.

While it would be possible to calibrate the framework utilizing this comparison method, one aspect is not yet optimally solved. Diagonal cracks are underrepresented since diagonally connecting pixels are also only multiplied with the length of the edges of one pixel/element, and not the diagonal length. Therefore, the approach is further extended to better represent the actual length of the cracks.

6.3.3 Crack-length estimation

For a better representation of diagonal fatigue cracks, a simple weighing of the individual pixels of the skeletonized results is performed. Since the goal is to adjust for diagonal cracks,

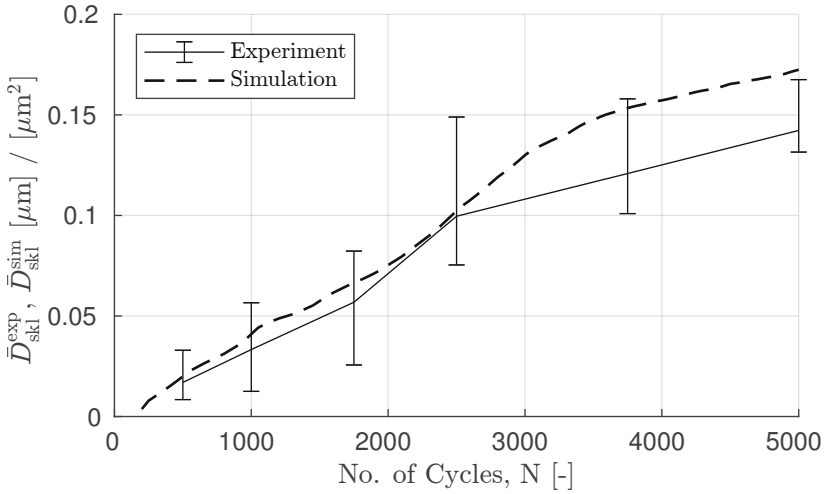

Figure 6.9: Comparison of the skeletonized experimental and simulated fatigue damage values over 5000 load cycles.

this weighting is based on the four diagonally adjacent pixels and elements, respectively. Three cases are distinguished, as shown in Figure 6.10. The assumed crack path is indicated by the dashed line. In case (a) there are no diagonally adjacent damaged pixels, therefore the weighing of the central pixel is 1. In case (b) there is one diagonally connected pixel, resulting in a weighing factor of $0.5 + \sqrt{2}/2 \approx 1.2$. In the case of two or more diagonally adjacent damaged pixels (c) a diagonal crack is assumed and a weighing factor of $\sqrt{2} \approx 1.4$ is used. Branching is not specifically addressed in this approach because its influence on the total length of the fatigue cracks is assumed to be negligible.

The approach is illustrated in a larger schematic example in Figure 6.11. On the left side, the original image is shown. On the right side, the skeletonized image with the corresponding

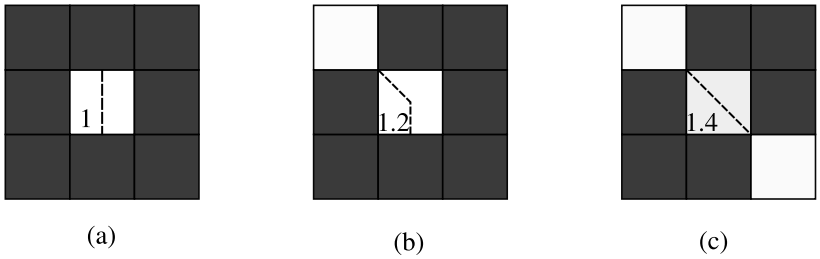

Figure 6.10: The three cases are differentiated to better represent diagonal fatigue cracks.

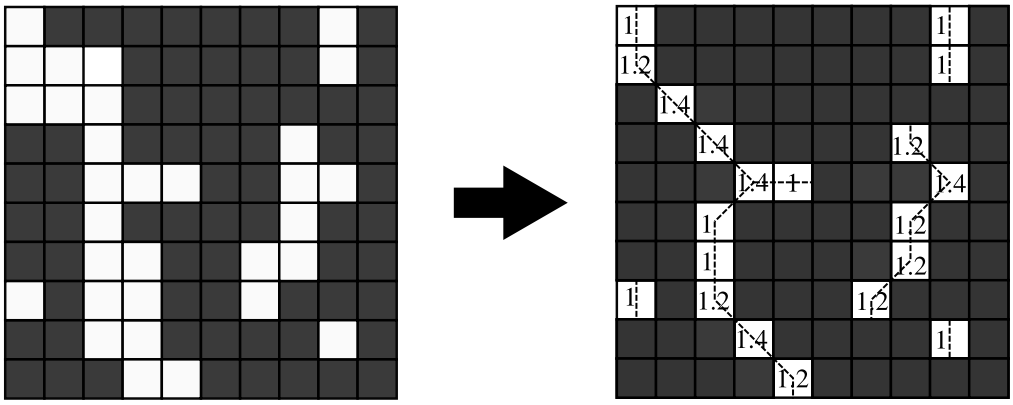

Figure 6.11: Schematic representation of the fatigue crack length assumption approach. The dashed lines represent the assumed fatigue crack path.

weighing factors is presented. Summing up the weighted values of the skeletonized results and multiplying them with the corresponding characteristic pixel/element length gives a good estimate of the length of the observed fatigue cracks. As described previously, these values are referred to the corresponding areas and are averaged over the individual simulations and experiments, respectively. For the simulations and experiments, the measures describing the crack-length per area are denoted as $\bar{D}_{\mathrm{cl}}^{\mathrm{sim}}(N)$ and $\bar{D}_{\mathrm{cl}}^{\mathrm{exp}}(N)$, respectively.

Figure 6.12 depicts $\bar{D}_{\mathrm{cl}}^{\mathrm{sim}}(N)$ and $\bar{D}_{\mathrm{cl}}^{\mathrm{exp}}(N)$ against the number of load cycles. The curves look similar to those of the skeletonization approach, but the overall crack-length per µm^2 is around 10% higher for both experiments and simulations due to the consideration of the diagonal cracks in both experiment and simulation. Overall, this approach provides good comparability between experiments and simulations. It results in a comprehensible value, and it is fast to compute without needing any manual engagement. Therefore, this approach is utilized in the following for the parameter estimation.

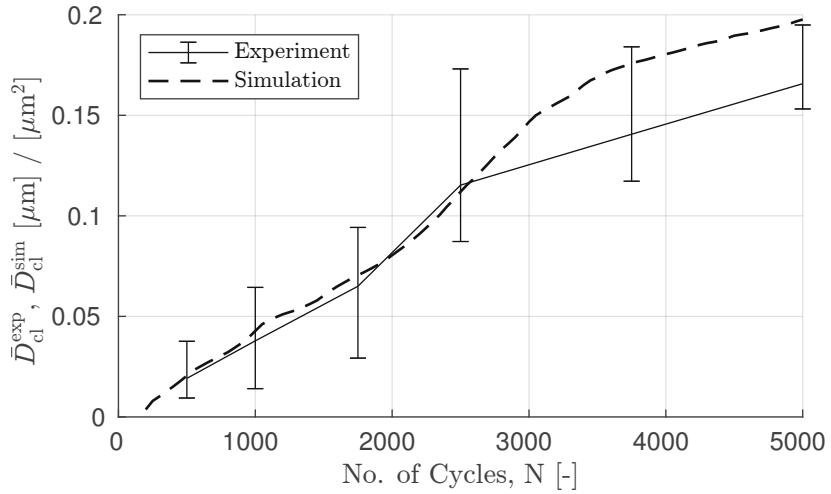

Figure 6.12: Comparison of the experimental and simulated fatigue crack-length per area values over 5000 load cycles.

Table 6.1: Estimated fatigue properties of copper

$\varkappa$	γ'_{f}	c_γ	α	κ_1	κ_2	s_{min}	r
1	0.1389	−0.3521	0.0006	varied	0.45	0.25	varied

6.4 Parameter estimation

A parameter study is presented that focuses on finding a good estimate for the two parameters κ_1 (cf. Equation (2.10)) and r (cf. Equation (5.2)). This study is a continuation of the parameter study presented in Chapter 5 with a more in depth parameter variation. The geometry, material properties, and boundary conditions used are the same used in the simulations presented in Section 5.5. The parameters of the damage onset law are taken from Chapter 4. The parameters necessary to model fatigue damage evolution are the same as used in Chapter 5. All parameters are briefly summarized in Table 6.1. The choice of s_{min} is motivated by studies of the industrial partner, which focus on the first occurrence of voids [43]. The value s_{min} is chosen in a way that the appearance of the first experimentally measured macrovoids coincides with the first occurrence of $D_{\mathrm{E}} = 1$, i.e. the first occurrence of a fully damaged element, in the simulations.

The results of nine combinations for the three values of r, 1, 0.75, and 0.5 and the three values of κ_1, 4×10^{-7}, 6×10^{-7}, and 8×10^{-7} are presented here in terms of the simulated crack-length $\bar{D}_{\mathrm{cl}}^{\mathrm{sim}}(N)$. The shape parameter r affects the void nucleation behavior at the triple junctions, with smaller values corresponding to less voiding. The parameter κ_1 influences the damage evolution, i.e., the growth from microvoids up to the formation of macrovoids and the subsequent formation of fatigue cracks.

The results of the simulations are presented in Figure 6.13 together with the experimental results. Each of the three plots shows the results for a constant value of r and three different values of κ_1. It can be seen that lower values of r lead to less detected crack-length per area during the earlier stages of the simulated fatigue life. For $r = 1$ and $r = 0.75$, all three curves fit the experimental results well during the first 2000 cycles. In contrast, $r = 0.5$ results in significantly less damage than experimentally detected. Nevertheless, an

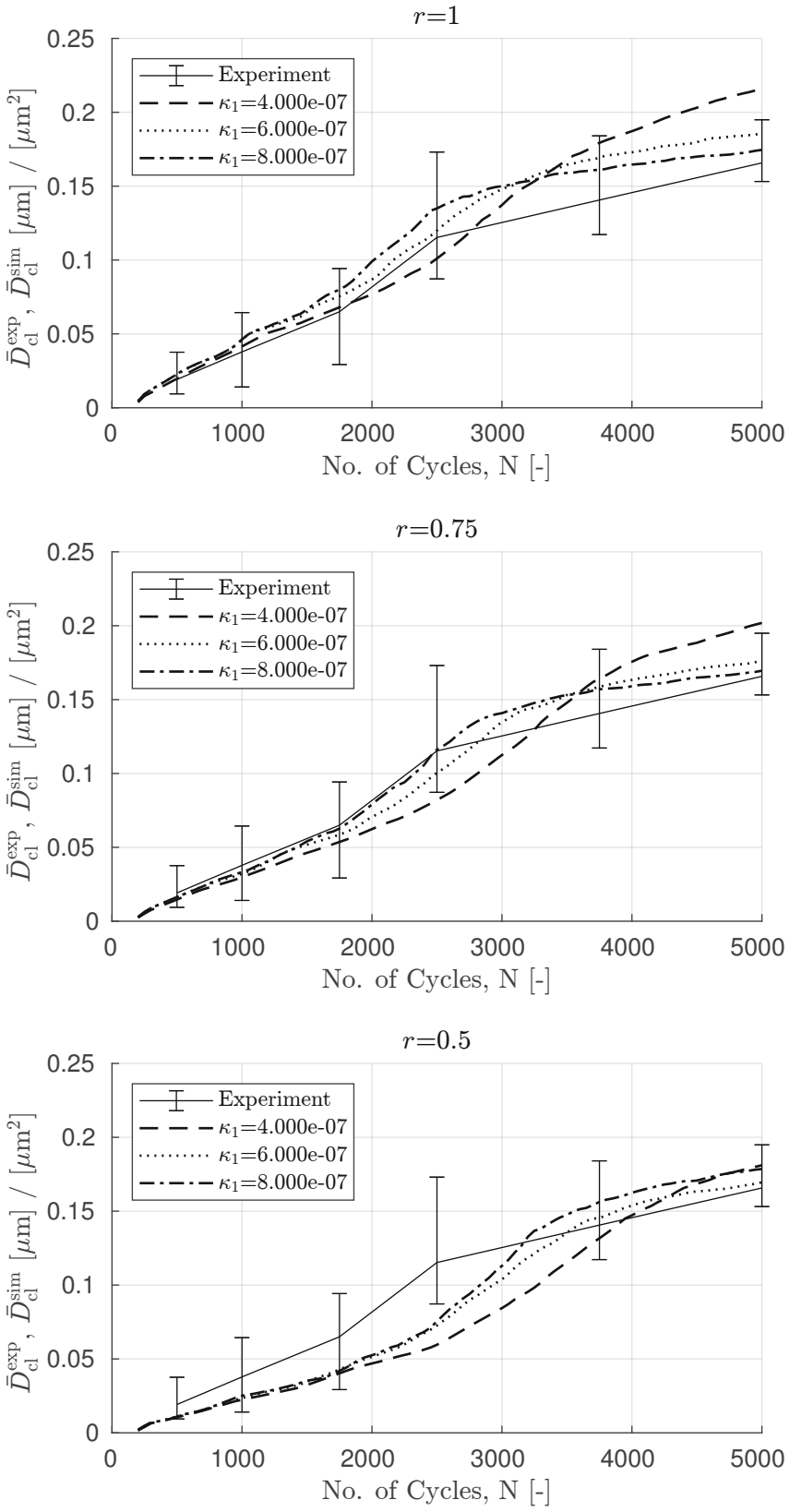

Figure 6.13: Results of the parameter estimation simulations showing the fatigue crack-length per area. The first Figure shows the results for $r = 1$, the second for $r = 0.75$, and the third for $r = 0.5$.

accelerated crack growth rate between 2000 and 4000 cycles leads to a final value of $\bar{D}_{\mathrm{cl}}^{\mathrm{sim}}$ at 5000 cycles, which is very similar to those obtained with $r = 1$ or $r = 0.75$, respectively.

As mentioned before, larger values of κ_1 lead to a faster formation of macrovoids and subsequent fatigue cracks. This leads to an earlier onset of shielding effects, resulting in higher values of $\bar{D}_{\mathrm{cl}}^{\mathrm{sim}}(N)$ at about 2500 cycles, but in lower ones at 5000 cycles.

6.4.1 Mean squared error

Overall, the results are very promising, with some of the parameter combinations are in good accordance with the experimental results. To find the pair of r and $\varkappa_1$ that provides the best match with the experimental results, a MSE approach is applied. The MSE value is calculated at the six data points of the experiment as

$$g = \frac{1}{6}\sum_{i=1}^{6}(\bar{D}_{\mathrm{cl}}^{\mathrm{exp}}(N_i) - \bar{D}_{\mathrm{cl}}^{\mathrm{sim}}(N_i))^2 \quad . \tag{6.4}$$

The results are given in Table 6.2. The combination $r = 0.75$ and $\kappa_1 = 8 \times 10^{-7}$ results in the best fit between simulation and experiment, and is referred to as the estimated parameter set. In Figure 6.13, it can be seen that for this combination, the simulation results agree very closely with the experimental results for the first four data points and

r	κ_1	g
1	4×10^{-7}	7.08×10^{-4}
	6×10^{-7}	2.37×10^{-4}
	8×10^{-7}	1.98×10^{-4}
0.75	4×10^{-7}	5.31×10^{-4}
	6×10^{-7}	1.23×10^{-4}
	8×10^{-7}	0.53×10^{-4}
0.5	4×10^{-7}	7.23×10^{-4}
	6×10^{-7}	4.36×10^{-4}
	8×10^{-7}	4.60×10^{-4}

Table 6.2: The MSE values of experimental and simulated crack-length per area values.

only start deviating marginally from the experimental curve afterward. Two slightly worse but still good fits are: $r = 0.75$, $\kappa_1 = 6 \times 10^{-7}$ and $r = 1$, $\kappa_1 = 8 \times 10^{-7}$.

6.4.2 Fatigue crack patterns

Figure 6.14 shows results of simulated and experimentally observed fatigue cracks for cycle numbers 1000, 1750, and 5000, respectively. For each cycle number, part of an experimentally obtained cross-section is presented at the top. These experimental cross-sections are compared to results of simulations at the respective cycle numbers. The simulated results are based on three different EBSD triple junction distributions, all using the best fitting parameters $r = 0.75$ and $\kappa_1 = 8 \times 10^{-7}$. Neither the experimental nor the simulated results are skeletonized.

The experimental results at 1000 cycles show many large voids and also some emerging fatigue macrocracks. In the simulations, relative similar damage patterns can be seen, with fatigue damage emerging at the most critical triple junctions. While larger fatigue cracks have not formed up to this point, some of the initially small macro cracks are already connected. After 1750 cycles, significantly larger fatigue cracks have formed in the experiments and also in the simulations. In both cases, no through-film crack can be observed. Within the experiments, the visible fatigue cracks are arranged predominately in vertical direction. The simulated fatigue cracks are slightly more diagonally aligned. This can be attributed to the FS fatigue criterion used for describing damage initiation, as it is based on the shear-strain amplitude (c.f. Equation 2.3). The images at 5000 load cycles are characterized by through-film cracks in the experiments and the simulations. For the experiments, one has to consider the 3D extension of the cracks, which are reduced to a 2D representation. This means that some of the fatigue cracks that appear to be unconnected in the cross-section are most likely linked out-of-plane. In all three simulations, a through-film crack has formed. In the left and the center simulation, a dominant crack and a few relatively small cracks are predicted. In the right image, two fatigue cracks have formed that are comparable in size.

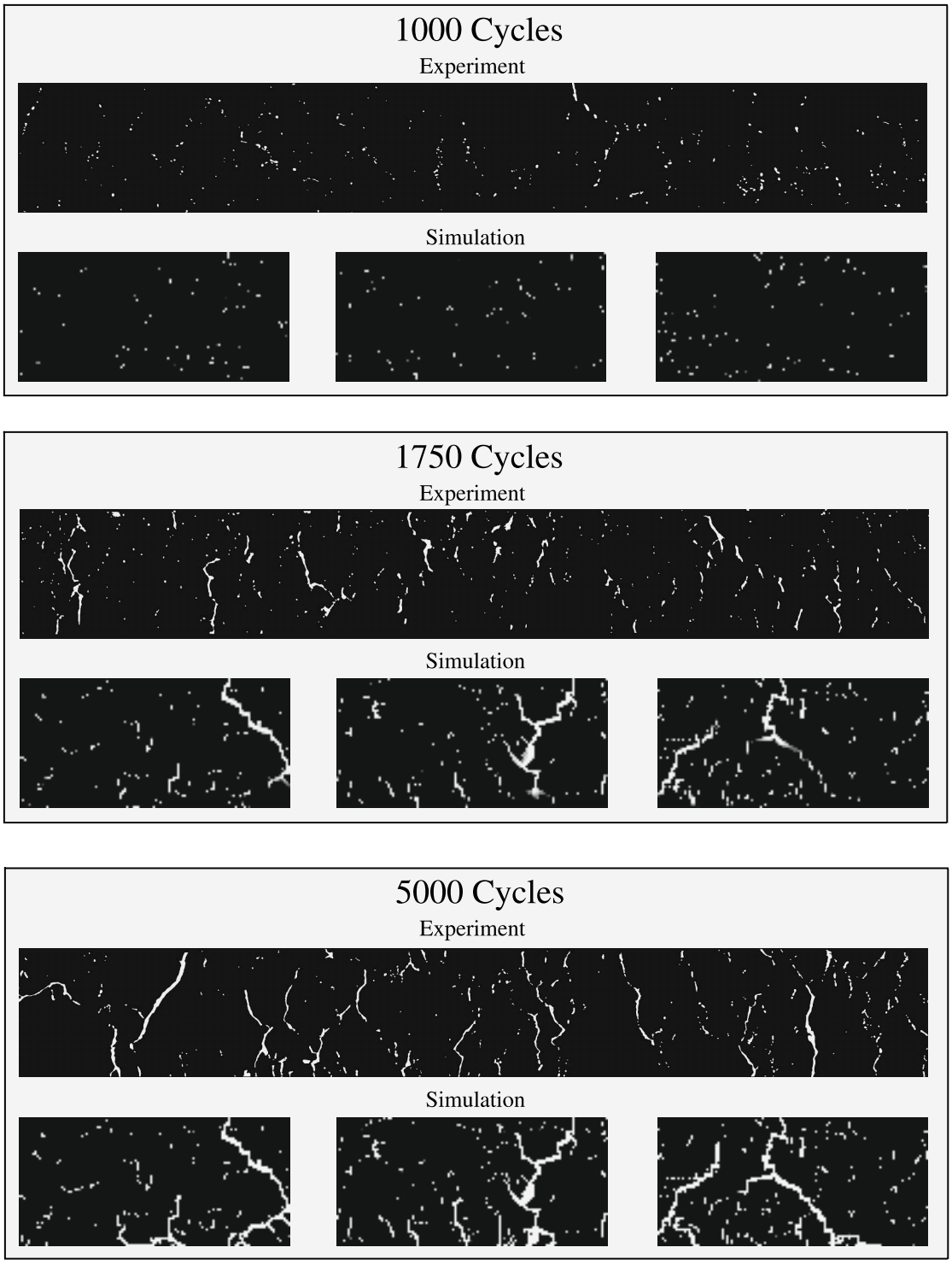

Figure 6.14: Result of the best fitting parameter simulations and corresponding experiments showing the developing fatigue crack patterns at three load cycle numbers. The simulations are based on three different EBSD triple junction distributions and the parameters $r = 0.75$ and $\kappa_1 = 8 \times 10^{-7}$.

Noteworthy is the previously discussed crack width discrepancy between experiments and simulations, which can be attributed to the coarse mesh size of the simulations. Leaving that aside, the simulated results are in good agreement with the experimental ones.

6.4.3 Through-film crack cycle numbers

As a final result of the parameter study, the number of cycles until the first appearance of a through-film crack is presented for each of the parameter sets. The number is determined the same way as in Chapter 5, utilizing a pathfinding algorithm. The obtained load cycle numbers are presented in Figure 6.15. The general trend shows that lower values of the shape parameter r lead to a higher number of load cycles until a through-film crack has formed. This trend is visible in Figure 6.13, where the shift to higher cycle numbers indicates a later overall formation of fatigue damage. Lower values of κ_1 also lead to higher load cycle numbers. Comparing these results to results presented in Figure 6.13, it can be seen that after through-films cracks have formed, the increase in additional crack-length slows down. Once again, this shows the shielding effects of long fatigue cracks.

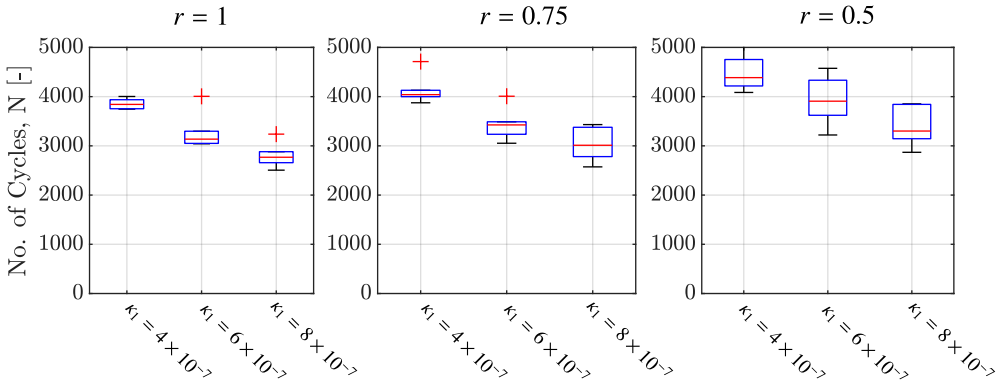

Figure 6.15: Cycle numbers until the first through-film crack has formed of the enrichment calibration study.

6.5 Application

An important requirement in the development of the enriched bulk fatigue damage model is its applicability to larger structures. To demonstrate the concept, the modeling approach is used to simulate fatigue damage in the poly-heater model of layout A as presented in Chapter 4. This DUT is of particular interest because of its spatially inhomogeneous temperature fields, which strongly influence the formation of fatigue damage.

The same model is used in terms of material properties, geometry, and boundary conditions as in Chapter 4. The fatigue and enrichment parameters are those with the best fit found in Section 6.4.1. For the enrichment, the same EBSD maps as for the parameter estimation studies are used by combining the 20 x 40 µm slices vertically side by side. As an example, two triple junction distributions with different sequences of 20 x 40 µm slices are created and used for two enriched CDM modeling simulations (I and II).

Instead of terminating the simulation after calculating the initial FIP, as done in Chapter 4, a modeling sequence is performed as schematically shown in Figure 6.16. This modeling

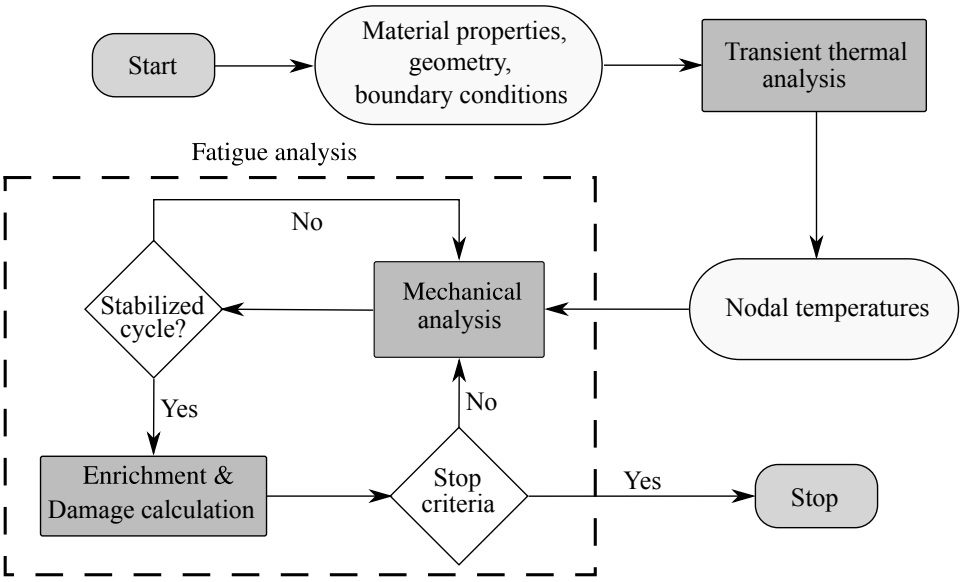

Figure 6.16: Simplified representation of the simulation procedure featuring the enriched bulk fatigue model.

cycle is similar to the one discussed in Chapter 3 but the nodal temperatures are not recalculated after fatigue damage has emerged. This is because the structure of the poly-heater, in combination with fatigue cracks that completely block heat conduction in the 2D representation, can lead to thermal isolation in some parts of the Cu metallization layer.

The simulations are run until a significant amount of fatigue cracks has accumulated and through-film cracks are observed. The resulting fatigue damage patterns are shown in Figure 6.17 and are compared to a SEM image of a corresponding experimental cross-section taken after 5000 cycles. The experimental procedure is as described in Section 4.2. At this cycle number, many fatigue cracks have formed. In the zone where high

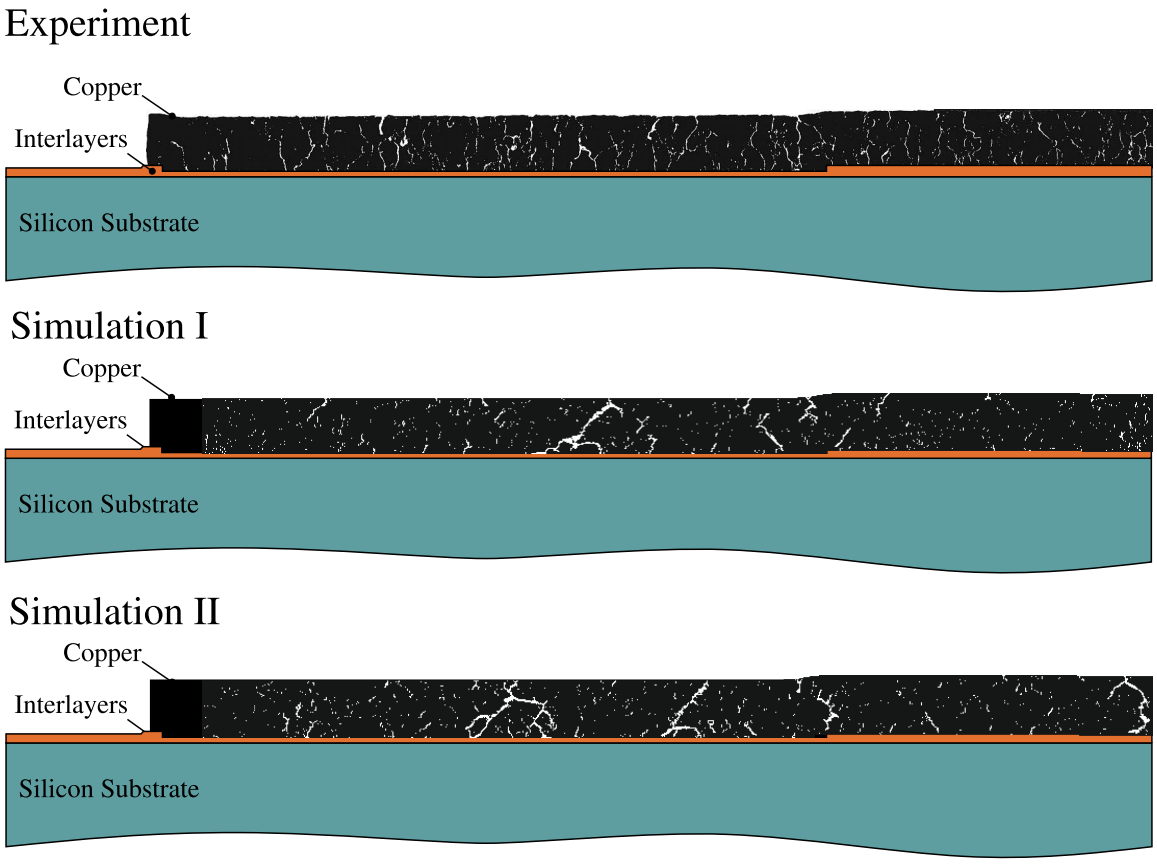

Figure 6.17: Resulting fatigue cracks in the layout A poly-heater as seen in the experimental analysis (top) and the two simulations featuring different triple junction distributions (bottom). Simulation I is depicted after 1456 cycles, simulation II after 1634 cycles.

temperatures occur, see Figure 4.7 in Chapter 4, more fatigue cracks are observed. Further experimental results are discussed more extensively in Chapter 4. It is noteworthy that one fatigue crack has emerged at the position of the surface irregularities caused by the 1.5 µm step in the copper metallization, as predicted in Chapter 4.

For simulation I, the fatigue damage after 1456 cycles is depicted. One large and dominant fatigue crack has formed at a central position in the region where the highest temperatures occur (cf. Figure 4.7) and many smaller fatigue cracks can be seen at different positions in the metallization layer. A fatigue crack has initiated at the Cu surface irregularity. Less fatigue damage has formed in the colder regions of the metallization layer, close to the center and the edges of the poly-heater, respectively. For simulation II (featuring a different triple junction distribution) the visible fatigue damage after 1634 cycles is shown. More fatigue cracks have formed than in simulation I. Two through-film cracks are visible in the region of high temperature, and again fatigue cracks can be seen at the position of the concave part of the small step in the surface topology. Another large fatigue crack has formed near the center of the poly-heater.

This example shows that the approach can be applied to larger 2D structures, since fatigue cracks form at the expected positions and since the corresponding cycle numbers are in a reasonable range. Overall, a good qualitative representation of the experiments is provided by the simulations.

6.6 Summary

The results presented in this chapter show that the calibration of a fatigue modeling framework based on experimental cross-sections is possible. Nevertheless, some limitations and open points have to be discussed.

The first point concerns how the susceptibility of the material to the formation of voids (s-value) is defined by introducing an additional parameter s into the framework. As explained in Chapter 5, the parameter is based on the misorientation angle at the position of triple

junctions. This is motivated by the current state of knowledge regarding the formation of microvoids in Cu metallizations. Further investigations might indicate a different critical microstructural descriptors or suggest a generally different relation between misorientation angle φ and s as described in Equation 5.2.

While the combination of parameters presented in this chapter results in a very good fit for the available experimental result, other combinations might provide better results for a broader range of applications. Different maximum temperatures or generally different load pulse types might result in different sets of fatigue parameters, or would even require temperature-dependent ones. This also leads to the next limitation, which is the relatively limited amount of experimental data. Further experimental studies would allow the parameters to be adjusted for different loading scenarios. However, it must also be pointed out that such experimental analyses are extremely resource and time-consuming.

The last limitation which has to be mentioned is the currently solely 2D application of the enrichment approach. In reality, fatigue cracks have a complex 3D shape in such devices. And it must be assumed that the formation of microvoids is also related to the properties of the 3D microstructure. Since the experimental images used for comparison and calibration are also only 2D representations and the main goal is an estimation of through-film cracks, the approach indicates potential as an initial assessment tool.

The studies presented in this chapter provide a way to compare fatigue cracks as seen in experimental cross-sections with simulated fatigue cracks from corresponding 2D thermo-mechanical simulations. It is demonstrated that by adjusting only two parameters, a very good fit between experiment and simulation can be achieved. Using the obtained set of parameters to model the formation of fatigue cracks within a larger test device also yields promising results.

Chapter 7

Conclusion

Power semiconductors are one of the cornerstones of modern technology and are used in almost every state-of-the-art electronic device. With decreasing component sizes and increasing reliability requirements, it is becoming more and more important that failure mechanisms are well understood and predictable. This has prompted the development of physical lifetime models, that are intended to represent the actual physical mechanisms behind device failure. The development and application of such models is a challenging task. In addition to their complex formulation, the necessary parameter calibration requires appropriate experimental data, which is difficult to obtain in the case of semiconductor device length scales.

The present work focuses on the application, calibration, and enhancement of the continuum damage mechanics based physical lifetime model developed in [47, 93]. This model intends to predict the formation of fatigue cracks in the copper metallization layer of Double–diffused Metal–Oxide–Semiconductor devices. The main cause for the formation of these types of fatigue cracks is thermo-mechanical loading due to repeated electrical overload pulses introducing high amounts of thermal energy.

In the original continuum damage mechanics based physical lifetime modeling framework, the local fatigue life of the material is split into two stages. In Stage I, a multiaxial Fatemi-Socie fatigue criterion is used to represent void accumulation and microcrack nucleation.

Stage II is based on an energy-based fatigue criterion and describes the growth and coalescence of microcracks until the formation of macroscopic fatigue cracks. The local influence of the growing microcrack is represented by a reduction of the local material integrity. Together with a cycle jump technique and implemented within the framework of the finite element method, this approach is capable of modeling the evolution of fatigue cracks in homogenized metallization layers. The calibration of the material parameters of the modeling framework associated with Stages I and II requires (i) a realistic representation of the actual thermo-mechanical loading conditions in actual devices and (ii) the ability to compare the experimental data with simulation results in a reproducible manner.

In order to correctly represent the thermo-mechanical loading conditions being present within semiconductors, the original framework was first incorporated into a transient thermo-mechanical simulation strategy. To show the capabilities of the simulation strategy, multiple simplified DMOS cells are subjected to different loading conditions featuring thermal gradients and cells with accelerated damage initiation. It is shown that thermal gradients affect the formation of fatigue damage in a sense that higher temperatures correlate with a faster formation of fatigue damage and consequently a faster emergence of fatigue cracks. Furthermore, fatigue cracks slow down the crack growth of other fatigue cracks in their vicinity.

Initial comparisons between thermo-mechanical experiments and simulations are made by relating the fatigue damage visible on the surface of the copper metallization of test devices to numerical results presented in the form of a Fatemi-Socie fatigue indication parameter. Based on this comparison, it is possible to calibrate the material parameters of the Coffin-Manson relation type fatigue law applied in Stage I of the physical lifetime modeling framework. The study highlights again the influence of lateral thermal gradients and also emphasizes that the formation of fatigue damage is strongly accelerated by irregularities on the copper surface. Furthermore, it becomes apparent that fatigue cracks also form away from mechanical stress concentrators and initiate at microstructural features of the metallization layer, such as triple junctions. This influence of the microstructure on the

formation of fatigue damage cannot be considered within the original formulation of the physical lifetime model.

To account for the influence of microstructural properties on the emergence of fatigue damage, an enrichment approach is proposed. Within this approach, a spatially varying parameter describing the susceptibility of the material to the initiation of fatigue damage is introduced. Various studies testing the influence of such a parameter on the formation of macroscopic fatigue cracks are conducted. Eventually, the parameter is based on the misorientation angles at the position of triple junctions. Parameter studies are conducted and presented, which indicate promising comparative possibilities with experimental results and good calibration capabilities.

Finally, a methodology is presented which enables a meaningful comparison between experimental results and numerical ones obtained using the enrichment approach. The experimental results are obtained from cross-sections of test devices experiencing no significant lateral thermal gradients. For comparing experimental and simulated results, the approximate crack-length per area is calculated for both instances. Based on this comparison method, the numerical approach is calibrated by a variation of parameters. A well-fitting combination of parameters can be found which represents the experimental formation of fatigue damage well.

The results presented here demonstrate the possibilities of the enrichment approach and its capability as a physical lifetime model for power semiconductors devices. Further research and experimental results are needed to validate the promising results and extend the scope of the approach.

Appendix A

Material Properties

The assumed temperature independent elastic material properties of cubic anisotropic Si are presented in Table A.1. It represents the material properties of a standard (100) Si wafer with the principal axes being aligned with the crystal directions [100], [010] and [001]. Further material properties of Si are assumed to be isotropic and can be found in Table A.2.

The temperature independent thermo-elastic and thermo-physical properties of the copper metallization taken from [47] are given in Table A.3. A temperature dependent formulation of a Chaboche model based on [105] is used to describe the plastic response of Cu (refer to Table A.4).

To calculate the FIP (Equation (4.2)) the two material parameters κ and σ_Y are required. These values are taken from [95] as $\kappa = 1.0$ and $\sigma_Y = 125\,\text{MPa}$. A temperature depended definition of σ_Y based on $\sigma_{Y,\text{chab}}$ would go beyond the scope of this work.

Table A.1: Elastic engineering moduli of Si [35]

$E_1 = E_2 = E_3$	$\nu_{12} = \nu_{23} = \nu_{31}$	$G_{12} = G_{23} = G_{31}$
GPa	-	GPa
130	0.28	79.6

Table A.2: Thermo physical properties of Si [5, 71], with the reference temperature for the CTE being 293 °C

Temperature K	CTE $10^{-6}\,\mathrm{K}^{-1}$	ρ $\frac{\mathrm{kg}}{\mathrm{m}^3}$	λ $\frac{\mathrm{W}}{\mathrm{m\,K}}$	c $\frac{\mathrm{J}}{\mathrm{kg\,K}}$
325	2.76	2360	71	730.80
400	3.21	2360	61	782.52
475	3.52	2360	53	816.32
550	3.72	2360	47	837.38
625	3.88	2360	42	854.16
700	3.99	2360	38	867.17

Table A.3: Temperature independent thermo-elastic and thermo-physical properties of polycrystalline Cu

E GPa	ν -	CTE $10^{-6}\,\mathrm{K}^{-1}$	ρ $\frac{\mathrm{kg}}{\mathrm{m}^3}$	λ $\frac{\mathrm{W}}{\mathrm{m\,K}}$	c $\frac{\mathrm{J}}{\mathrm{kg\,K}}$
100	0.35	16.7	8960	385	385

The material properties of the interlayers are taken from [44] and [47]. The reference temperature for the CTE of all materials is assumed to be 20 °C.

Table A.4: Temperature dependent plastic parameters of Cu

Temperature K	$\sigma_{\mathrm{Y,chab}}$ MPa	C_1 MPa	γ_1 -
163	157	2000	9.0
293	142	1800	8.5
398	130	1600	8.0
473	107	1400	7.5
673	79	1200	7.0

Table A.5: Material properties of the interlayers

	E GPa	ν	CTE $10^{-6}\mathrm{K}^{-1}$	ρ $\frac{\mathrm{kg}}{\mathrm{m}^3}$	λ $\frac{\mathrm{W}}{\mathrm{m\,K}}$	c $\frac{\mathrm{J}}{\mathrm{kg\,K}}$
SiN	305	0.262	2.60	3190	260	761
SiO_2	72	0.17	8.10	2180	1.38	750
barrier	260	0.26	4.5	19250	163	134
metal-1 Al	70	0.35	24.0	2700	210	900

Appendix B

Skeletonization

The skeletonization algorithm utilized in this work is one of the two included in MATLAB based on [51]. In the following the description of the algorithm is reproduced one to one from the MATLAB manual [37]. It consists of two subiterations that together form one iteration of the thinning algorithm:

1. In the first subiteration: delete pixel p if and only if G_1, G_2, and G_3 are all satisfied.
2. In the second subiteration: delete pixel p if and only if G_1, G_2, and $G_3{}'$ are all satisfied.

Condition G_1:

$$X_H(p) = 1 \tag{B.1}$$

where

$$X_H(p) = \sum_{i=1}^{4} b_i \tag{B.2}$$

$$b_i = \begin{cases} 1, \text{ if } x_{2i-1} \text{ and } (x_{2i} = 1 \text{ or } x_{2i+1} = 1) \\ 0, \text{ otherwise} \end{cases} \tag{B.3}$$

$x_1, x_2, ..., x_8$ are the values of the eight neighbors of p, starting with the east neighbor and number in counter-clockwise order.

Condition G_2:

$$2 \leq \min\{n_1(p), n_2(p)\} \leq 3 \tag{B.4}$$

where

$$n_1(p) = \sum_{k=1}^{4} x_{2k-1} \vee x_{2k} \tag{B.5}$$

$$n_2(p) = \sum_{k=1}^{4} x_{2k} \vee x_{2k+1} \tag{B.6}$$

Condition G_3:

$$(x_2 \vee x_3 \vee \bar{x}_8) \wedge x_1 = 0 \tag{B.7}$$

Condition G_3':

$$(x_6 \vee x_7 \vee \bar{x}_4) \wedge x_5 = 0 \tag{B.8}$$

In the given case the iterations are repeated until no changes are made during one step.

Bibliography

[1] T. Aichinger, M. Nelhiebel, and T. Grasser. Unambiguous identification of the NBTI recovery mechanism using ultra-fast temperature changes. In *2009 IEEE International Reliability Physics Symposium*, pages 2–7. IEEE, 2009.

[2] T. Aichinger, M. Nelhiebel, S. Einspieler, and T. Grasser. In situ poly heater—a reliable tool for performing fast and defined temperature switches on chip. *IEEE Transactions on Device and Materials Reliability*, 10(1):3–8, 2010.

[3] S. Amiable, S. Chapuliot, A. Constantinescu, and A. Fissolo. A comparison of lifetime prediction methods for a thermal fatigue experiment. *International Journal of Fatigue*, 28(7):692–706, 2006.

[4] M. Andresen, G. Buticchi, and M. Liserre. Thermal stress analysis and MPPT optimization of photovoltaic systems. *IEEE Transactions on Industrial Electronics*, 63 (8):4889–4898, 2016.

[5] M. Asheghi, K. Kurabayashi, R. Kasnavi, and K. E. Goodson. Thermal conduction in doped single-crystal silicon films. *Journal of Applied Physics*, 91(8):5079–5088, 2002.

[6] G. Bal, J. Diebold, E. W. Chambers, E. Gasparovic, R. Hu, K. Leonard, M. Shaker, and C. Wenk. Skeleton-based recognition of shapes in images via longest path matching. In *Association for Women in Mathematics Series*, pages 81–99. Springer International Publishing, 2015.

[7] J. A. Bannatine and D. F. Socie. A variable amplitude multiaxial fatigue life prediction method. In *Third International Conference on Biaxial/Multiaxial Fatigue*, Stuttgart, 1989.

[8] C. Bathias and A. Pineau, editors. *Fatigue of Materials and Structures*. John Wiley & Sons, Inc., 2013.

[9] R. Bayerer, T. Herrmann, T. Licht, J. Lutz, and M. Feller. Model for power cycling lifetime of IGBT modules - various factors influencing lifetime. In *5th International Conference on Integrated Power Electronics Systems*, pages 1–6. IEEE, 2008.

[10] S. Bigl. *Thermo-mechanical behaviour of thick copper metallizations for power electronics*. PhD thesis, Montanuniversität Leoben, 2017.

[11] B. Bose. Global warming: Energy, environmental pollution, and the impact of power electronics. *IEEE Industrial Electronics Magazine*, 4(1):6–17, 2010.

[12] M. W. Brown and K. J. Miller. A theory for fatigue failure under multiaxial stress-strain conditions. *Proceedings of the Institution of Mechanical Engineers*, 187(1): 745–755, 1973.

[13] A. Brunko, W. Holzke, H. Groke, B. Orlik, and N. Kaminski. Model-based condition monitoring of power semiconductor devices in wind turbines. In *2019 21st European Conference on Power Electronics and Applications (EPE '19 ECCE Europe)*, pages 1–9. IEEE, 2019.

[14] R. Darveaux. Effect of simulation methodology on solder joint crack growth correlation and fatigue life prediction. *Journal of Electronic Packaging*, 124(3):147–154, 2002.

[15] *ABAQUS Analysis User's Guide. V6(2016)*. Dassault Systemes Simulia Corp., Providence, RI, USA, 2016.

[16] S. de Filippis. *Modeling, simulation and validation of the electro–thermal interaction in power MOSFETs*. PhD thesis, Università degli Studi di Napoli Federico II, 2013.

[17] S. de Filippis, V. Košel, D. Dibra, S. Decker, H. Köck, and A. Irace. ANSYS based 3d electro-thermal simulations for the evaluation of power MOSFETs robustness. *Microelectronics Reliability*, 51(9-11):1954–1958, 2011.

[18] D. Dibra, M. Stecher, S. Decker, A. Lindemann, J. Lutz, and C. Kadow. On the origin of thermal runaway in a trench power MOSFET. *IEEE Transactions on Electron Devices*, 58(10):3477–3484, 2011.

[19] E. W. Dijkstra. A note on two problems in connexion with graphs. *Numerische Mathematik*, 1(1):269–271, 1959.

[20] C. Durand, M. Klingler, D. Coutellier, and H. Naceur. Study of fatigue failure in al-chip-metallization during power cycling. *Engineering Fracture Mechanics*, 138: 127–145, 2015.

[21] C. Durand, M. Klingler, D. Coutellier, and H. Naceur. Power cycling reliability of power module: A survey. *IEEE Transactions on Device and Materials Reliability*, 16 (1):80–97, 2016.

[22] S. P. Eiser. *An extension to Nitsche-type mortaring for non-conforming finite elements*. PhD thesis, TU Wien, 2016.

[23] J. Falck, C. Felgemacher, A. Rojko, M. Liserre, and P. Zacharias. Reliability of power electronic systems: An industry perspective. *IEEE Industrial Electronics Magazine*, 12(2):24–35, 2018.

[24] G. H. Farrahi, M. Azadi, G. Winter, and W. Eichlseder. A new energy-based isothermal and thermo-mechanical fatigue lifetime prediction model for aluminium-silicon-magnesium alloy. *Fatigue & Fracture of Engineering Materials & Structures*, 36(12): 1323–1335, 2013.

[25] A. Fatemi and P. Kurath. Multiaxial fatigue life predictions under the influence of mean-stresses. *Journal of Engineering Materials and Technology*, 110(4):380–388, 1988.

[26] A. Fatemi and D. F. Socie. A critical plane approach to multiaxial fatigue damage including out-of-phase loading. *Fatigue & Fracture of Engineering Materials and Structures*, 11(3):149–165, 1988.

[27] C. E. Feltner and J. D. Morrow. Microplastic strain hysteresis energy as a criterion for fatigue fracture. *Journal of Basic Engineering*, 83(1):15–22, 1961.

[28] L. B. Freund and S. Suresh. *Thin Film Materials*. Cambridge University Press, 2004.

[29] T. Gocmez, A. Awarke, and S. Pischinger. A new low cycle fatigue criterion for isothermal and out-of-phase thermomechanical loading. *International Journal of Fatigue*, 32(4):769–779, 2010.

[30] M. Held, P. Jacob, G. Nicoletti, P. Scacco, and M.-H. Poech. Fast power cycling test of IGBT modules in traction application. In *Proceedings of Second International Conference on Power Electronics and Drive Systems*, volume 1, pages 425–430. IEEE, 1997.

[31] M. Held, P. Jacob, G. Nicoletti, P. Scacco, , and M.-H. Poech. Fast power cycling test for insulated gate bipolar transistor modules in traction application. *International Journal of Electronics*, 86(10):1193–1204, 1999.

[32] N. Heuck, K. Guth, M. Thoben, A. Mueller, N. Oeschler, L. Boewer, R. Speckels, S. Krasel, and A. Ciliox. Aging of new interconnect-technologies of power-modules during power-cycling. In *CIPS 2014; 8th International Conference on Integrated Power Electronics Systems*, pages 1–6, 2014.

[33] P. Hoffmann, M. Nelhiebel, B. Karunamurthy, H. E. Pettermann, and M. Todt. Simulation of fatigue damage in clusters of DMOS cells subjected to non-uniform transient thermo-mechanical loading. In *2020 21st International Conference on Thermal, Mechanical and Multi-Physics Simulation and Experiments in Microelectronics and Microsystems (EuroSimE)*, pages 1–9. IEEE, 2020.

[34] P. Hoffmann, S. Moser, C. Kofler, M. Nelhiebel, D. Tscharnuter, B. Karunamurthy, H. E. Pettermann, and M. Todt. Thermomechanical fatigue damage modeling and

material parameter calibration for thin film metallizations. *International Journal of Fatigue*, 155:106627, 2022.

[35] M. A. Hopcroft, W. D. Nix, and T. W. Kenny. What is the Young's modulus of silicon? *Journal of Microelectromechanical Systems*, 19(2):229–238, 2010.

[36] R. Hormozi, F. Biglari, and K. Nikbin. Experimental study of type 316 stainless steel failure under LCF/TMF loading conditions. *International Journal of Fatigue*, 75: 153–169, 2015.

[37] T. M. Inc. *MathWorks Documentation (R2023a)*. Natick, Massachusetts, United States, 2023. URL `https://www.mathworks.com/help/images/ref/bwmorph.html`.

[38] P. Jacob. Reliability testing and analysis of igbt power semiconductor modules. In *IEE Colloquium on IGBT Propulsion Drives*, page 4/1–4/5. IEE, 1995.

[39] M. Junghaenel and U. Scheuermann. Impact of load pulse duration on power cycling lifetime of chip interconnection solder joints. *Microelectronics Reliability*, 76-77:480–484, 2017.

[40] W. Kanert. Active cycling reliability of power devices: Expectations and limitations. *Microelectronics Reliability*, 52(9-10):2336–2341, 2012.

[41] J. G. Kassakian and T. M. Jahns. Evolving and emerging applications of power electronics in systems. *IEEE Journal of Emerging and Selected Topics in Power Electronics*, 1(2):47–58, 2013.

[42] B. Khong, M. Legros, P. Dupuy, C. Levade, and G. Vanderschaeve. Alterations induced in the structure of intelligent power devices by extreme electro-thermal fatigue. *Physica Status Solidi (c)*, 4(8):2997–3001, 2007.

[43] M. Kleinbichler, C. Kofler, M. Stabentheiner, M. Reisinger, S. Moser, J. Zechner, M. Nelhiebel, and E. Kozeschnik. Quantitative analysis of void initiation in thermo-mechanical fatigue of polycrystalline copper films. *Microelectronics Reliability*, 127: 114387, 2021.

[44] H. Köck. *Experimental and numerical study on heat transfer problems in microelectronic devices.* PhD thesis, University of Klagenfurt, 2012.

[45] P. Konglerd, C. Reeb, F. Jansson, and J. A. Kaandorp. Quantitative morphological analysis of 2D images of complex-shaped branching biological growth forms: the example of branching thalli of liverworts. *BMC Research Notes*, 10(103):1–6, 2017.

[46] V. Košel. *Thermo-Mechanical Analysis of Smart Power Switches under Dynamic Thermal Stress Conditions.* PhD thesis, Slovak University of Technology, Bratislava, 2009.

[47] G. Kravchenko. *Numerical simulations of fatigue crack problems in semiconductor devices subjected to thermomechanical loading.* PhD thesis, TU Wien, 2014.

[48] G. Kravchenko, B. Karunamurthy, M. Nelhiebel, and H. E. Pettermann. Finite element analysis of fatigue cracks formation in power metallisation of a semiconductor device subjected to active cycling. In *2013 14th International Conference on Thermal, Mechanical and Multi-Physics Simulation and Experiments in Microelectronics and Microsystems (EuroSimE)*, pages 1–6. IEEE, 2013.

[49] B. Kroposki, C. Pink, R. DeBlasio, H. Thomas, M. Simões, and P. K. Sen. Benefits of power electronic interfaces for distributed energy systems. *IEEE Transactions on Energy Conversion*, 25(3):901–908, 2010.

[50] H. Köck, V. Košel, C. Djelassi, M. Glavanovics, and D. Pogany. IR thermography and FEM simulation analysis of on-chip temperature during thermal-cycling power-metal reliability testing using in situ heated structures. *Microelectronics Reliability*, 49(9-11):1132–1136, 2009.

[51] L. Lam, S.-W. Lee, and C. Suen. Thinning methodologies-a comprehensive survey. *IEEE Transactions on Pattern Analysis and Machine Intelligence*, 14(9):869–885, 1992.

[52] J. H. Lau, S. H. Pan, and C. Chang. A new thermal-fatigue life prediction model for wafer level chip scale package (WLCSP) solder joints. *Journal of Electronic Packaging*, 124(3):212–220, 2002.

[53] J. Leppänen, G. Ross, V. Vuorinen, J. Ingman, J. Jormanainen, and M. Paulasto-Kröckel. A humidity-induced novel failure mechanism in power semiconductor diodes. *Microelectronics Reliability*, 123:114207, 2021.

[54] X. Liu. *Processing and Reliability Interconnection Assessment of Solder for Power Chips Joint*. PhD thesis, Virginia Polytechnic Institute and State University, 2001.

[55] W.-S. Loh, M. Corfield, H. Lu, S. Hogg, T. Tilford, and C. M. Johnson. Wire bond reliability for power electronic modules - effect of bonding temperature. In *2007 International Conference on Thermal, Mechanical and Multi-Physics Simulation Experiments in Microelectronics and Micro-Systems. EuroSime 2007*, pages 1–6. IEEE, 2007.

[56] J. Lutz. Semiconductor power devices as key technology for a future sustainable society. In *Power Electronic Components and their Applications 2017; 7. ETG-Symposium*, pages 1–15, 2017.

[57] J. Lutz, H. Schlangenotto, U. Scheuermann, and R. D. Doncker. *Semiconductor Power Devices*. Springer International Publishing, 2018.

[58] K. Ma, M. Liserre, and F. Blaabjerg. Lifetime estimation for the power semiconductors considering mission profiles in wind power converter. In *2013 IEEE Energy Conversion Congress and Exposition*, pages 590–602. IEEE, 2013.

[59] E. Macha and C. Sonsino. Energy criteria of multiaxial fatigue failure. *Fatigue Fracture of Engineering Materials and Structures*, 22(12):1053–1070, 1999.

[60] A. Maligno, D. Whalley, and V. Silberschmidt. Thermal fatigue life estimation and delamination mechanics studies of multilayered MEMS structures. *Microelectronics Reliability*, 52(8):1665–1678, 2012.

[61] A. Manonukul and F. P. E. Dunne. High– and low–cycle fatigue crack initiation using polycrystal plasticity. *Proceedings of the Royal Society of London. Series A: Mathematical, Physical and Engineering Sciences*, 460(2047):1881–1903, 2004.

[62] D. Martineau, T. Mazeaud, M. Legros, P. Dupuy, C. Levade, and G. Vanderschaeve. Characterization of ageing failures on power MOSFET devices by electron and ion microscopies. *Microelectronics Reliability*, 49(9-11):1330–1333, 2009.

[63] D. Martineau, C. Levade, M. Legros, P. Dupuy, and T. Mazeaud. Universal mechanisms of al metallization ageing in power MOSFET devices. *Microelectronics Reliability*, 54(11):2432–2439, 2014.

[64] M. A. Miner. Cumulative damage in fatigue. *Journal of Applied Mechanics*, 12: 159–164, 1945.

[65] M. Mori. Power semiconductor devices creating comfortable low-carbon society. Technical report, Hitachi, 2008.

[66] S. Moser, G. Zernatto, M. Kleinbichler, M. Nelhiebel, J. Zechner, M. J. Cordill, and R. Pippan. A novel setup for in situ monitoring of thermomechanically cycled thin film metallizations. *JOM*, 71(10):3399–3406, 2019.

[67] S. Moser, M. Kleinbichler, S. Kubicek, J. Zechner, and M. J. Cordill. Electropolishing—a practical method for accessing voids in metal films for analyses. *Applied Sciences*, 11(15):7009, 2021.

[68] S. Murakami. *Continuum Damage Mechanics*. Springer Netherlands, 2012.

[69] M. Nelhiebel, R. Illing, C. Schreiber, S. Wöhlert, S. Lanzerstorfer, M. Ladurner, C. Kadow, S. Decker, D. Dibra, H. Unterwalcher, M. Rogalli, W. Robl, T. Herzig, M. Poschgan, M. Inselsbacher, M. Glavanovics, and S. Fraissé. A reliable technology concept for active power cycling to extreme temperatures. *Microelectronics Reliability*, 51(9-11):1927–1932, 2011.

[70] M. Nelhiebel, R. Illing, T. Detzel, S. Wöhlert, B. Auer, S. Lanzerstorfer, M. Rogalli, W. Robl, S. Decker, J. Fugger, and M. Ladurner. Effective and reliable heat management for power devices exposed to cyclic short overload pulses. *Microelectronics Reliability*, 53(9-11):1745–1749, 2013.

[71] Y. Okada and Y. Tokumaru. Precise determination of lattice parameter and thermal expansion coefficient of silicon between 300 and 1500 K. *Journal of Applied Physics*, 56(2):314–320, 1984.

[72] A. Palmgren. Die Lebensdauer von Kugellagern. *Zeitschrift des Vereines Deutscher Ingenieure*, 68(14):339–341, 1924.

[73] I. Papadopoulos. A comparative study of multiaxial high-cycle fatigue criteria for metals. *International Journal of Fatigue*, 19(3):219–235, 1997.

[74] J. Park. Evaluation of an energy-based approach and a critical plane approach for predicting constant amplitude multiaxial fatigue life. *International Journal of Fatigue*, 22(1):23–39, 2000.

[75] T. M. A. Pelisset. *Degradation analysis of thin die-attach layer under cyclic thermal load in microelectronics packaging.* PhD thesis, Montanuniversität Leoben, 2015.

[76] M. Pfost, C. Boianceanu, H. Lohmeyer, and M. Stecher. Electrothermal simulation of self-heating in DMOS transistors up to thermal runaway. *IEEE Transactions on Electron Devices*, 60(2):699–707, 2013.

[77] S. Pietranico, S. Lefebvre, S. Pommier, M. B. Bouaroudj, and S. Bontemps. A study of the effect of degradation of the aluminium metallization layer in the case of power semiconductor devices. *Microelectronics Reliability*, 51(9-11):1824–1829, 2011.

[78] J. Popović-Gerber, J. A. Oliver, N. Cordero, T. Harder, J. A. Cobos, M. Hayes, S. C. O'Mathuna, and E. Prem. Power electronics enabling efficient energy usage: Energy savings potential and technological challenges. *IEEE Transactions on Power Electronics*, 27(5):2338–2353, 2012.

[79] E. A. Poshtan, S. Rzepka, C. Silber, and B. Wunderle. An in-situ numerical–experimental approach for fatigue delamination characterization in microelectronic packages. *Microelectronics Reliability*, 62:18–25, 2016.

[80] W. Robl, M. Melzl, B. Weidgans, R. Hofmann, and M. Stecher. Last metal copper metallization for power devices. *IEEE Transactions on Semiconductor Manufacturing*, 21(3):358–362, 2008.

[81] R. Ruffilli. *Fatigue mechanisms in Al-based metallizations in power MOSFETs*. PhD thesis, Université Paul Sabatier - Toulouse III, 2017.

[82] F. Saghaeian, M. Lederer, A. Hofer, J. Todt, J. Keckes, and G. Khatibi. Investigation of high cyclic fatigue behaviour of thin copper films using MEMS structure. *International Journal of Fatigue*, 128:105179, 2019.

[83] M. D. Sangid. The physics of fatigue crack initiation. *International Journal of Fatigue*, 57:58–72, 2013.

[84] J. Schindelin, I. Arganda-Carreras, E. Frise, V. Kaynig, M. Longair, T. Pietzsch, S. Preibisch, C. Rueden, S. Saalfeld, B. Schmid, J.-Y. Tinevez, D. J. White, V. Hartenstein, K. Eliceiri, P. Tomancak, and A. Cardona. Fiji: an open-source platform for biological-image analysis. *Nature Methods*, 9(7):676–682, 2012.

[85] R. Schmidt, F. Zeyss, and U. Scheuermann. Impact of absolute junction temperature on power cycling lifetime. In *2013 15th European Conference on Power Electronics and Applications (EPE)*, pages 1–10. IEEE, 2013.

[86] S. Semboshi, M. Sato, Y. Kaneno, A. Iwase, and T. Takasugi. Grain boundary character dependence on nucleation of discontinuous precipitates in cu-ti alloys. *Materials*, 10(4):415, 2017.

[87] N. Shammas. Present problems of power module packaging technology. *Microelectronics Reliability*, 43(4):519–527, 2003.

[88] R. Sleik, M. Glavanovics, S. Einspieler, A. Muetze, and K. Krischan. Modular test system architecture for device, circuit and system level reliability testing. In *2016 IEEE Applied Power Electronics Conference and Exposition (APEC)*, pages 759–765. IEEE, 2016.

[89] K. Smith, T. Topper, and P. Watson. A stress–strain function for the fatigue of metals. *Journal of Materials*, 5:767–778, 1970.

[90] T. Smorodin, J. Wilde, P. Alpern, and M. Stecher. Investigation and improvement of fast temperature-cycle reliability for DMOS-related conductor path design. In *2007 IEEE International Reliability Physics Symposium Proceedings. 45th Annual*, pages 486–491. IEEE, 2007.

[91] T. Smorodin, J. Wilde, P. Nelle, E. Lilleodden, and M. Stecher. Modeling of DMOS subjected to fast temperature cycle stress and improvement by a novel metallization concept. In *2008 IEEE International Reliability Physics Symposium*, pages 689–690. IEEE, 2008.

[92] G. Spagnuolo, G. Petrone, S. V. Araujo, C. Cecati, E. Friis-Madsen, E. Gubia, D. Hissel, M. Jasinski, W. Knapp, M. Liserre, P. Rodriguez, R. Teodorescu, and P. Zacharias. Renewable energy operation and conversion schemes: A summary of discussions during the seminar on renewable energy systems. *IEEE Industrial Electronics Magazine*, 4(1):38–51, 2010.

[93] M. Springer. *Modeling and Simulation of Fatigue Damage in Power Semiconductors*. PhD thesis, TU Wien, 2017.

[94] M. Springer and H. Pettermann. Fatigue life predictions of metal structures based on a low-cycle, multiaxial fatigue damage model. *International Journal of Fatigue*, 116: 355–365, 2018.

[95] M. Springer and H. E. Pettermann. A thermo-mechanical fatigue damage modeling methodology for power semiconductor robustness validation studies. In *2018 19th International Conference on Thermal, Mechanical and Multi-Physics Simulation and*

Experiments in Microelectronics and Microsystems (EuroSimE), pages 1–8. IEEE, 2018.

[96] M. Springer, M. Nelhiebel, and H. E. Pettermann. Fatigue crack growth modeling in the metallization of power semiconductors under cyclic thermo-mechanical loading. In *2016 17th International Conference on Thermal, Mechanical and Multi-Physics Simulation and Experiments in Microelectronics and Microsystems (EuroSimE)*, pages 1–5. IEEE, 2016.

[97] P. K. Steimer. Enabled by high power electronics - energy efficiency, renewables and smart grids. In *The 2010 International Power Electronics Conference - ECCE ASIA*, pages 11–15. IEEE, 2010.

[98] P. Ullmann. Method for real-time observation of thermo-mechanical induced fatigue in copper thin. Master's thesis, TU Wien, 2017.

[99] T. Walter, G. Khatibi, M. Nelhiebel, and M. Stefenelli. Characterization of cyclic delamination behavior of thin film multilayers. *Microelectronics Reliability*, 88-90: 721–725, 2018.

[100] G. Wang, P. S. Ho, and S. Groothuis. Chip-packaging interaction: a critical concern for cu/low k packaging. *Microelectronics Reliability*, 45(7-8):1079–1093, 2005.

[101] H. Wang, M. Liserre, and F. Blaabjerg. Toward reliable power electronics: Challenges, design tools, and opportunities. *IEEE Industrial Electronics Magazine*, 7(2):17–26, 2013.

[102] H. Wang, M. Liserre, F. Blaabjerg, P. de Place Rimmen, J. B. Jacobsen, T. Kvisgaard, and J. Landkildehus. Transitioning to physics-of-failure as a reliability driver in power electronics. *IEEE Journal of Emerging and Selected Topics in Power Electronics*, 2 (1):97–114, 2014.

[103] Z. Wang, Z. Zhang, X. Li, W. Jia, and S. Li. Orientation dependence of the cyclic deformation behavior and the role of grain boundaries in fatigue damage in copper crystals. *Materials Science and Engineering: A*, 319-321:63–73, 2001.

[104] E. Wilfried, W. Gerhard, M. Robert, and R. Marti. Comparison of energy-based and damage-related fatigue life models for aluminium components under TMF loading. In *Recent Trends in Processing and Degradation of Aluminium Alloys*, pages 329–336. InTech, 2011.

[105] A. Wimmer, A. Leitner, T. Detzel, W. Robl, W. Heinz, R. Pippan, and G. Dehm. Damage evolution during cyclic tension–tension loading of micron-sized Cu lines. *Acta Materialia*, 67:297–307, 2014.

[106] A. Wimmer, M. Smolka, W. Heinz, T. Detzel, W. Robl, C. Motz, V. Eyert, E. Wimmer, F. Jahnel, R. Treichler, and G. Dehm. Temperature dependent transition of intragranular plastic to intergranular brittle failure in electrodeposited Cu micro-tensile samples. *Materials Science and Engineering: A*, 618:398–405, 2014.

[107] Y. Yamada, Y. Takaku, Y. Yagi, I. Nakagawa, T. Atsumi, M. Shirai, I. Ohnuma, and K. Ishida. Reliability of wire-bonding and solder joint for high temperature operation of power semiconductor device. *Microelectronics Reliability*, 47(12):2147–2151, 2007.

[108] B. A. Zahn. Finite element based solder joint fatigue life predictions for a same die stacked chip scale ball grid array package. In *27th Annual IEEE/SEMI International Electronics Manufacturing Technology Symposium*, pages 274–284, 2002.

[109] H. Zeller. Cosmic ray induced failures in high power semiconductor devices. *Solid-State Electronics*, 38(12):2041–2046, 1995.